SIYUAN ZHAO
POSTDOCTORAL FELLOW OF BIOENGINEERING
John A. Paulson School of Engineering and Applied Sciences
Science and Engineering Complex
150 Western Ave., Room 3.208, Boston, MA 02134, USA
Phone: 617-230-3963
Email: siyuanzhao@g.harvard.edu

HARVARD
UNIVERSITY

January 30, 2024

Dear Members of the Faculty Search Committee:

I am writing to apply for Position 2 (Implantable Medical Devices) of Assistant Professor in the Department of Systems Design Engineering (SYDE) at the University of Waterloo. <u>I was deeply interested to learn of this opportunity, as it aligns closely with my research and teaching interests, especially in implanted brain-computer interfaces.</u> I received my Ph.D. in Physical Chemistry from Peking University in 2019 and have since been pursuing postdoctoral research at the John A. Paulson School of Engineering and Applied Sciences, Harvard University. My research has resulted in 12 published journal papers, including *Nature Neuroscience, Nature Nanotechnology, Nature Communications*, etc.

My Ph.D. and postdoctoral research have focused on developing novel materials and devices to address challenges in neuroscience and brain-computer interfaces. Significant accomplishments include the development of MRI-compatible neural electrodes for simultaneous DBS and MRI, enabling real-time disease detection and treatment by identifying neural responses from previously undetected regions (**Zhao et al.,** *Nature Communications*, 2020; **Zhao et al.,** *Nano Letters*, 2016). Additionally, I developed micro-porous mesh electronics with minimally invasive methods for single-cell and subcellular electrophysiology, for the first time, enabling monitoring of the same neurons over the lifespan of mice (**Zhao et al.,** *Nature Neuroscience*, 2023). Moreover, I developed elastic photo-patternable dielectric material (PFPE-DMA) that is 10,000 times softer than conventional plastic encapsulation, such as SU8 and polyimide. PFPE-DMA device is essential for long-term nanoelectronics-tissue interfaces in the brain and spinal cord of freely moving rodents (Le and **Zhao et al.,** *Nature Nanotechnology*, 2023, contributed equally).

My future research aims to advance the next-generation bioelectronics materials and devices for applications in biology and medicine. I will carry two layers of research: First, I will continue to develop cutting-edge tools for large-scale electrophysiology and multimodal mapping of living organisms with high resolution and minimal invasiveness. Secondly, by leveraging advancements in technology, I will strive to address fundamental questions in cognitive neuroscience and explore powerful new approaches for the treatment of neurological and neurodegenerative diseases, and traumatic brain and spinal cord injuries, ultimately aiming to advance human health through brain-computer interfaces.

In addition to my research, I have experience in teaching courses and mentoring undergraduate and graduate students. My teaching experience includes serving as a teaching assistant at Harvard and Peking University. My responsibilities included developing new class materials, leading class discussions, supervising labs, grading all assignments, and meeting with students individually. I have mentored four undergraduates and two graduates during my career via different research programs. I am prepared to teach courses in physical chemistry, materials science, neural engineering, and biological signal processing. I would also welcome the opportunity to develop new courses, according to departmental needs.

<u>I am deeply attracted to the diverse research areas within the department, especially in the development of novel devices for next-generation implanted brain-computer interfaces.</u> My interdisciplinary background and research initiatives enable me to contribute to and benefit from the collaborative culture on campus. I am excited about the possibility of collaborating with faculty members to generate novel electronics-tissue interfaces and develop advanced materials and biosensors for neuroscience and medical applications. I believe my research program not only complements but also enhances the department's core focus areas.

Thank you for considering my application. I look forward to hearing from you.

Sincerely,

Siyuan Zhao

Siyuan Zhao, Ph.D.

Siyuan Zhao, Ph.D.

+1 6172303963; siyuanzhao@g.harvard.edu

RESEARCH INTERESTS

My work, combining experimental and computational approaches within an interdisciplinary team, seeks to address key questions in neuroscience and challenges in neurotechnology. The ultimate goal is to advance human health through brain-computer interfaces.

RESEARCH EXPERIENCE

2019 -   **Postdoctoral Fellow,** School of Engineering and Applied Sciences, *Harvard University*, Boston, MA
Project: Soft and Flexible Bioelectronics for Chronically Stable Electrophysiology of the Same Neurons at Single-Cell Resolution
Faculty Advisor: Dr. Jia Liu

EDUCATION

2014 -19   **Ph.D. in Physical Chemistry**, *Peking University,* China
Thesis: Development of Highly MRI-Compatible Neural Electrodes and Their Application in Rodent Models of Parkinson's Disease
Faculty Advisor: Dr. Xiaojie Duan

2010 -14   **B.S. in Chemistry**, *Shandong University,* China
Faculty Advisor: Dr. Liqiang Zheng

PUBLICATIONS

Selected publications (∗ Equal contribution)
1. **S. Zhao***, X.Tang*, W. Tian*, S. Partarrieu*, R. Liu, H. Shen, J. Lee, J. Lee, S. Guo, Z. Lin, and J. Liu. Tracking neural activity from the same cells during the entire adult life of mice. *Nature Neuroscience,* 2023; 26 (4), 696-710.
2. P. Floch*, **S. Zhao***, R. Liu*, N. Molinari, E. Medina, Z. Wang, J. Kim, H. Sheng, S. Partarrieu, H. Shen, W. Wang, W. Tian, C. Sessler, G. Zhang, H. Park, X. Gong, A. Spencer, J. Lee, T. Ye, X. Tang, X. Wang, K. Bertold, N. Lu, B. Kozinsky, Z. Suo, J. Liu, Fluorinated elastomer enabled spatiotemporally scalable in vivo neural interfaces. *Nature Nanotechnology*, https://doi.org/10.1038/s41565-023-01545-6, (Equal contribution). Research highlights in *Nature Nanotechnology*, "Soft high-density neural probes enable stable single-neuron recordings".
3. **S. Zhao***, G. Li*, C. Tong, W. Chen, P. Wang, J. Dai, X. Fu, X. Liu, L. Lu, Z. Liang, and X. Duan, Full activation pattern mapping by simultaneous deep brain stimulation and fMRI with graphene fiber electrodes. *Nature Communications,* 2020; 11 (1), 1788.
4. T. Xin*, H. Shen*, **S. Zhao**, N. Li, and J. Liu, Flexible brain-computer interfaces. *Nature Electronics*, 2023; 6 (2), 109-118.

5. **S. Zhao**, X. Liu, Z. Xu, H, Ren, B. Deng, M. Tang, L. Lu, X. Fu, H. Peng, Z. Liu, and X. Duan, Graphene encapsulated copper microwires as highly MRI compatible neural electrodes. *Nano Letters*, 2016; 16 (12): 7731-7738.

Additional Published Research
6. R. Liu*, **S. Zhao*,** and J. Liu. From lithographically patternable to genetically patternable electronic materials for miniaturized, scalable, and soft implantable bioelectronics to interface with nervous and cardiac systems. *ACS Applied Electronic Materials*, 2020; 3 (1): 101-118.
7. P. Floch*, Q. Li*, Z. Lin*, **S. Zhao**, R. Liu, K. Tasnim, H. Jiang, and J. Liu. Stretchable mesh nanoelectronics for 3D single-cell chronic electrophysiology from developing brain organoids. *Advanced Materials,* 2022; 34 (11): 2106829.
8. Luo, Y., Abidian, M. R., Ahn, J. H., Akinwande, D., Andrews, A. M., Antonietti, M., ... **S. Zhao**… & Chen, X. Technology roadmap for flexible sensors. *ACS Nano*, 2023; 17 (6), 5211-5295.
9. L. Lu, X. Fu, Y. Liew, Y. Zhang, **S. Zhao**, Z. Xu, J. Zhao, D. Li, Q. Li, G.B. Stanley and X. Duan, Soft and MRI compatible neural electrodes from carbon nanotube fibers. *Nano Letters,* 2019; 19 (3): 1577-86.
10. R. Yin, Z. Xu, M. Mei, Z. Chen, K. Wang, Y. Liu, T. Tang, M. Kr. Priydarshi, X. Meng, **S. Zhao**, B. Deng, H. Peng, Z. Liu, and X. Duan. Soft transparent graphene contact lens electrodes for conformal full-cornea recording of electroretinogram. *Nature Communications,* 2018; *9* (1), 2334.
11. H. Gao, T. Kan, **S. Zhao**, Y. Qian, X. Cheng, W. Wu, X. Wang, and L. Zheng. Removal of anionic azo dyes from aqueous solution by functional ionic liquid cross-linked polymer. *Journal of Hazardous Materials,* 2013; 261: 83-90.
12. H. Gao, **S. Zhao**, X. Cheng, X. Wang, and L. Zheng. Removal of anionic azo dyes from aqueous solution using magnetic polymer multi-wall carbon nanotube nanocomposite as adsorbent. *Chemical Engineering Journal,* 2013; 223: 84-90.

Manuscripts Under Review
S. Guo*, **S. Zhao***, X. Tang*, B. Bordelon, H. Shen, R. Liu, S. Partarrieu, J. Lee, S. Vesuna, Y. He, N. Li, C. Pehlevan and J. Liu, Integration of flexible electronics with artificial intelligence-driven circuits for long-term stable and self-programmable brain state decoding. *Nature Machine Intelligence* (minor revision), Submitted in March 2022.

Manuscripts in Preparation
S. Zhao*, H. Shen*, S. Qin, S. Jiang, J. Liu, Monitoring representational drift in mouse visual cortex by flexible electrode arrays.

Google Scholar:
https://scholar.google.com/citations?hl=en&user=nkVGDkcAAAAJ&view_op=list_works&sortby=pubdate

PATENTS

Graphene-coated copper-based biomaterials and their associated preparation methods and applications, CN107875456A, granted, 2018

PRESENTATIONS

Soft and Flexible Bioelectronics for Brain-Computer Interfaces, Peking University Health Science Center, (virtual, invited), July 2023

Flexible Neural Interface, MRSEC Seed Meeting, Harvard University, Cambridge, MA. (invited), Dec. 2021

MRI compatible neural electrodes for simultaneous deep brain stimulation and fMRI mapping, Annual Meeting ISMRM-ESMRMB, Paris, France. June 2018

Graphene encapsulated copper microwires as highly MRI compatible neural electrodes, Physical Chemistry Graduate Frontier Forum, Peking University, Beijing, China. May 2017

TEACHING & ADVISING EXPERIENCE

Teaching Assistant
Responsibilities included developing new class materials, leading class discussions, supervising labs, grading all assignments, and meeting with students individually.
- Neuroengineering, Harvard University: 17 undergraduate and 13 graduate students (Fall 2022)
- Introduction to Neuroengineering, Peking University: 40 graduate students (Spring 2016)
- Chemistry Lab, Shandong University: 42 undergraduate students (Fall 2012)

Advising Experience
Advised one graduate student and three undergraduate students, Harvard University, 2019-
Advised one graduate student and one undergraduate student, Peking University, 2014-19

SELECTED FELLOWSHIPS & AWARDS

Youth Science Award, Peking University, 2018
Leo KoGuan Scholarship, Peking University, 2017
Academic Innovation Award, Peking University, 2017

PROFESSIONAL SERVICE

Committee Experience
Editorial board member of *Frontiers in Neuroscience, Neural Technology,* 2023
Section Editor of *Frontiers in Human Neuroscience*, 2023
Co-organizer, Center for Nanochemistry (CNC) Annual Symposium at Peking University, 2015

Reviewer
npj flexible electronics, Biosensors & Bioelectronics, Journal of Neuroscience Methods, Bioengineering, Biosensors, and Sensors.

1. **S. Zhao***, X.Tang*, W. Tian*, S. Partarrieu*, R. Liu, H. Shen, J. Lee, J. Lee, S. Guo, Z. Lin, and J. Liu. Tracking neural activity from the same cells during the entire adult life of mice. *Nature Neuroscience,* 2023; 26 (4), 696-710. https://doi.org/10.1038/s41593-023-01267-x

   My contribution: conceiving the idea, implanted mesh electronics fabrication, device characterization, brain implantation, histology studies, electrophysiological recording, data analysis, wrote the manuscript.

2. P. Floch*, **S. Zhao***, R. Liu*, N. Molinari, E. Medina, Z. Wang, J. Kim, H. Sheng, S. Partarrieu, H. Shen, W. Wang, W. Tian, C. Sessler, G. Zhang, H. Park, X. Gong, A. Spencer, J. Lee, T. Ye, X. Tang, X. Wang, K. Bertold, N. Lu, B. Kozinsky, Z. Suo, J. Liu, Fluorinated elastomer enabled spatiotemporally scalable in vivo neural interfaces. *Nature Nanotechnology*, https://doi.org/10.1038/s41565-023-01545-6, (**Equal contribution**). Research highlights in *Nature Nanotechnology*, "Soft high-density neural probes enable stable single-neuron recordings".

   My contribution: device characterization, brain and spinal cord implantation, histology studies, animal behavior testing, electrophysiological recording, data analysis, wrote the manuscript.

3. **S. Zhao***, G. Li*, C. Tong, W. Chen, P. Wang, J. Dai, X. Fu, X. Liu, L. Lu, Z. Liang, and X. Duan, Full activation pattern mapping by simultaneous deep brain stimulation and fMRI with graphene fiber electrodes. *Nature Communications,* 2020; 11 (1), 1788.

   My contribution: conceiving the idea, device fabrication, device characterization, brain implantation, histology studies, animal behavior testing, Parkinson's disease animal model, data analysis, wrote the manuscript.

Tracking neural activity from the same cells during the entire adult life of mice

Siyuan Zhao ®[1,3], Xin Tang ®[1,3], Weiwen Tian[1,3], Sebastian Partarrieu ®[1,3], Ren Liu[1], Hao Shen ®[1], Jaeyong Lee[1], Shiqi Guo[1], Zuwan Lin ®[2] & Jia Liu ®[1]✉

Stably recording the electrical activity of the same neurons over the adult life of an animal is important to neuroscience research and biomedical applications. Current implantable devices cannot provide stable recording on this timescale. Here, we introduce a method to precisely implant electronics with an open, unfolded mesh structure across multiple brain regions in the mouse. The open mesh structure forms a stable interwoven structure with the neural network, preventing probe drifting and showing no immune response and neuron loss during the year-long implantation. Rigorous statistical analysis, visual stimulus-dependent measurement and unbiased, machine-learning-based analysis demonstrated that single-unit action potentials have been recorded from the same neurons of behaving mice in a very long-term stable manner. Leveraging this stable structure, we demonstrated that the same neurons can be recorded over the entire adult life of the mouse, revealing the aging-associated evolution of single-neuron activities.

Long-term stable recording[1–4] of the same neurons at single-cell and single-spike resolution over the entire adult stage of life of behaving animals is important for understanding how neural activity changes with learning and aging, improving current brain–machine interface performance and studying neurological disorders[5–8]. However, current implantable electronic and optical tools can record neural activity at single-cell and single-spike resolution but suffer from immune response and recording drift caused by the mechanical and structural disparities between these devices and brain tissues[9,10]. The proliferation of astrocytes and microglia and the relative shear and repeat motion at the electrode–neuron interface can disrupt the relative position between recording devices and neurons, leading to chronic instability of recordings. Optical imaging techniques are also limited by the light penetration depth and three-dimensional (3D) volumetric scanning across the 3D tissue due to optical aberration and attenuation[11].

Miniaturized flexible electronics, such as mesh electronics and thin-film probes, have been used in in vivo electrophysiology given their unique mechanical properties[12–16]. Mesh electronics can provide a stable, gliosis-free interface over a few months through their tissue-like

structural and mechanical properties[17–19], but they require invasive methods, such as syringe injection, for implantation[17–19]. The relatively large mechanical damage from the implantation causes permanent damage to the neural network. In addition, implanted mesh electronics can unfold only in the cavities of the brain, such as the subventricular zone, but not in tissue-dense brain regions[17–19]. Therefore, the bundled mesh electronics do not have the optimized mechanical flexibility required to interface with the brain tissue over extended periods[17–20]. On the other hand, flexible thin-film brain probes lack the open mesh structures needed for 3D integration with the neural network[21,22] and need to maintain mechanical strength to prevent probe damage during implantation[21–23], which can cause immune responses and probe drift during long-term implantation. As a result, none of these technologies has been able to demonstrate long-term stable tracking of the same neuron over the entire adult stage of a behaving animal.

To address these challenges, we developed a method for implanting fully unfolded tissue-like mesh electronics into the mouse brain. The fully unfolded mesh electronics can form an interwoven structure within the neural network, eliminate immune response and probe drift

[1]John A. Paulson School of Engineering and Applied Sciences, Harvard University, Boston, MA, USA. [2]Department of Chemistry and Chemical Biology, Harvard University, Cambridge, MA, USA. [3]These authors contributed equally: Siyuan Zhao, Xin Tang, Weiwen Tian, Sebastian Partarrieu. ✉e-mail: jia_liu@seas.harvard.edu

and enable long-term stable, single-cell-level recording of the same neurons over the entire adult life of animals (Fig. 1a). We achieved this by fabricating mesh electronics monolithically integrated with ultra-thin, releasable polymer shuttles using lithographic techniques. We also incorporated unique polymer anchors and water-releasable structures, which enable precise and minimally invasive delivery of mesh electronics in the brain. This implantation method allows the open mesh structure of the device to be maintained across multiple brain regions, including cell-dense tissue regions. The open mesh can form seamlessly interwoven structures with neural networks, providing a tissue-level flexible interface and preventing repeated micromotion and drift between recording electrodes and the surrounding neural tissue during year-long recording, enabling highly stable recording of neural activity across multiple brain regions.

In addition, we integrated tetrode-like microelectrode arrays into the mesh electronics, which demonstrated the long-term stable tracking of single-unit action potentials from the same neurons. Chronic visual stimulation experiments further demonstrated the ability to record visual stimulus-dependent single-unit action potentials from the same neurons in a long-term stable manner. By optimizing the size and layout of implanted mesh electronics, we demonstrated the ability of mesh electronics to track neural activities of the same neurons over the entire adult life of mice, as confirmed by rigorous statistical and machine-learning-based tests[2,3,24–29]. The year-long recording data revealed neurons with age-dependent changes in extracellular waveform and firing dynamics.

Results

Integrated mesh electronics with ultra-thin polymer shuttle

To fully implant an open and unfolded mesh structure into the brain, we monolithically integrated the mesh electronics with ultra-thin, releasable polymeric shuttles using standard photolithography (Fig. 1b, Extended Data Fig. 1a–m and Methods). The mesh electronics were fabricated as described in previous reports[17–19]. In brief, 16 or 32 15-μm-diameter electrodes were connected by SU-8 encapsulated Cr/Au interconnects to Cr/Au input/output (I/O) pads. The interconnects were 10 μm wide and <1 μm thick, forming a mesh network with a two-dimensional (2D) filling ratio of 73.3% and an effective bending stiffness of 1.26×10^{-15} N m^{-2}, similar to that of brain tissue and orders of magnitude lower than state-of-the-art probes (that is, ultra-small carbon[30,31], polyimide[32] and elastomer-based probes[33]). The mesh electronics were partially fabricated on a nickel (Ni) sacrificial layer, and a 25-μm-thick polymer shuttle was defined on top of the mesh

electronics with ~2-μm-thick water-soluble dextran and 20-μm-thick polymer anchors (Extended Data Fig. 1n–r). These anchors (Fig. 1b, inset) connected the mesh electronics to the polymer shuttle through the dextran layer (Fig. 1b, red box, and Extended Data Fig. 1s,t). After the integrated device was released from the substrate by removing the Ni sacrificial layer (Fig. 1c, top, and Extended Data Fig. 1u), the anchor kept the unfolded mesh structure on the polymer shuttle. A layer of 10 wt% polyethylene glycol (PEG, 35 kDa) was then coated on the mesh electronics to reinforce the bonding with the polymer shuttle (Fig. 1c, bottom, and Extended Data Fig. 1v–w) and protect the mesh electronics during implantation. The biodegradable PEG adhesion layer was sub-micron thick, so the surgical footprint was mostly affected by the ultra-thin polymer shuttle. After the anchor connection was removed (Fig. 1c, bottom, and Extended Data Fig. 1w), the mesh electronics could then be released (Extended Data Fig. 1x) from the polymer shuttle by dissolving the PEG in an aqueous solution (Fig. 1d).

Two manipulators were used during the implantation procedure with the integrated device inserted by the first manipulator and the polymer shuttle extracted with the secondary manipulator (Fig. 1e and Extended Data Fig. 2a–f). We characterized the implantation procedure in a transparent 0.6 wt% agarose gel-based brain phantom with mechanical properties similar to brain tissue[34]. At a typical implantation speed of 100 μm s^{-1}, we did not observe any buckling of the device (Fig. 1f, left). After insertion, saline solution was applied to dissolve the PEG/dextran adhesive layer, and the shuttle was withdrawn at a speed of 10 μm s^{-1}. The device maintained its implantation location and open mesh structure without any deformations after the shuttle was removed (Fig. 1f, right). We tested the yield of the implantation in gel-based brain phantoms at various speeds and achieved a 93.3% ± 11.5% (mean ± s.d., $n = 3$ individual researchers; Extended Data Fig. 2g,h) yield for insertion and extraction of 16-channel mesh electronics at 100 μm s^{-1}. There was no difference in implantation yield of mesh electronics with different sizes ($n = 3$, $P > 0.05$ for all comparisons; Extended Data Fig. 2g,h). However, slower insertion speeds (for example, 10 μm s^{-1}) resulted in the PEG dissolving before the integrated mesh electronics reached the designed depth. The optimized implantation procedure was then used for mouse brain implantation. Figure 1e,g and Extended Data Fig. 2a–f show the typical implantation of 300-μm-wide 16-channel mesh electronics in the anesthetized mouse brain (Methods). The polymer shuttle was used to guide the implantation of the mesh electronics into the brain tissue (Fig. 1e and Extended Data Fig. 2a). After the integrated brain probe reached the targeted position, saline was applied to quickly dissolve the PEG to release the mesh electronics from the polymer shuttle,

Fig. 1 | Minimally invasive implantation of tissue-level flexible mesh electronics in the brain. a, Schematics showing the long-term stable electrical recording of the same neurons over the entire adult life of mice enabled by minimally invasively implanted and fully unfolded tissue-level flexible mesh electronics. Mesh electronics integrate seamlessly with neural networks without immune response and electrode drift. Single-cell electrophysiology from the same animal at (i) mature adult (3–6 months), (ii) middle (10–14 months) and (iii) old (18–24 months) stages are recorded. Colored waveforms represent different neurons stably recorded over the entire adult life of mice. **b**, Exploded view of the integrated mesh electronics showing the distinct material layers. The fully assembled electronics consist of (from top to bottom) ~25-μm-thick releasable polymer shuttle, ~20-μm-thick polymer anchor, ~2-μm-thick dextran dissolvable layer, a 450-nm-thick top SU-8 encapsulation layer, 50-nm-thick platinum electrodes and 70-nm-thick gold (Au) interconnects and a 450-nm-thick bottom SU-8 encapsulation layer. Inset: bright-field (BF) microscopic image of mesh electronics connected to the polymer shuttle through anchors (white arrows). **c**, Schematics showing the stepwise releasing of mesh electronics from the substrate and shuttle. The device was released from the fabrication substrate after removing the Ni sacrificial layer while still connected with the polymer shuttle by anchors (top). The released shuttle/electronics were cleaned for bonding and dicing and then coated by the biodegradable PEG through dip-coating. After cutting the polymer anchors, the device was finally released

from the shuttle by dissolving the coated PEG (bottom). **d**, Photographs showing the released polymer shuttle/mesh electronics hybrid from the substrate (top) and released mesh electronics from the shuttle (bottom). Red dashed lines and arrows highlight the cutting lines of the anchors and the released mesh electronics, respectively. **e**, Schematics showing the brain implantation process. **f**, In vitro images of mesh electronics implantation in a 0.6% agarose gel. Insets: zoomed-in images showing the released mesh electronics maintain an unfolded structure at the implantation location after withdrawing the polymer shuttle. The red arrow indicates the polymer shuttle integrated with the mesh electronics after insertion. **g**, Photograph showing the representative brain implantation with minimal tissue damage. Inset: ultra-thin polymer shuttle-enabled implantation. **h**, Statistical analysis of tissue acute damage zone of different implantation methods. Data are represented as mean ± s.d., and individual data points are overlaid (polymer shuttle versus tungsten shuttle, $P = 0.5149$; polymer shuttle versus 30-gauge needle, $P = 4.7 \times 10^{-4}$; polymer shuttle versus biodegradable PEG shuttle, $P = 3.5 \times 10^{-4}$; ***$P < 0.001$, NS, not significant, two-tailed t-test, $n = 5$ mesh electronics). **i**, Representative images of 20-μm-thick horizontal brain slices showing the acute tissue damages introduced by the ultra-thin polymer shuttle (left) and 50-μm-diameter tungsten shuttle (right). Yellow and cyan represent cross-sections of mesh electronics and DAPI, respectively. The tissue damage region is highlighted by white dashed lines. The experiments were repeated on $n = 5$ independent animals with similar results.

which was subsequently withdrawn from the brain tissue (Fig. 1e and Extended Data Fig. 2a,c–f). Specifically, after the device was implanted to the target position, saline solution was applied at the brain surface to dissolve the PEG coating between the polymer shuttle and the mesh

(Extended Data Fig. 2c). A small drop of glue was then placed on the polymer shuttle carrier chip to connect a customized 3D-printed pole to the second manipulator on the stereotaxic frame (Extended Data Fig. 2d). After 5–10 minutes, when the PEG coating was dissolved and
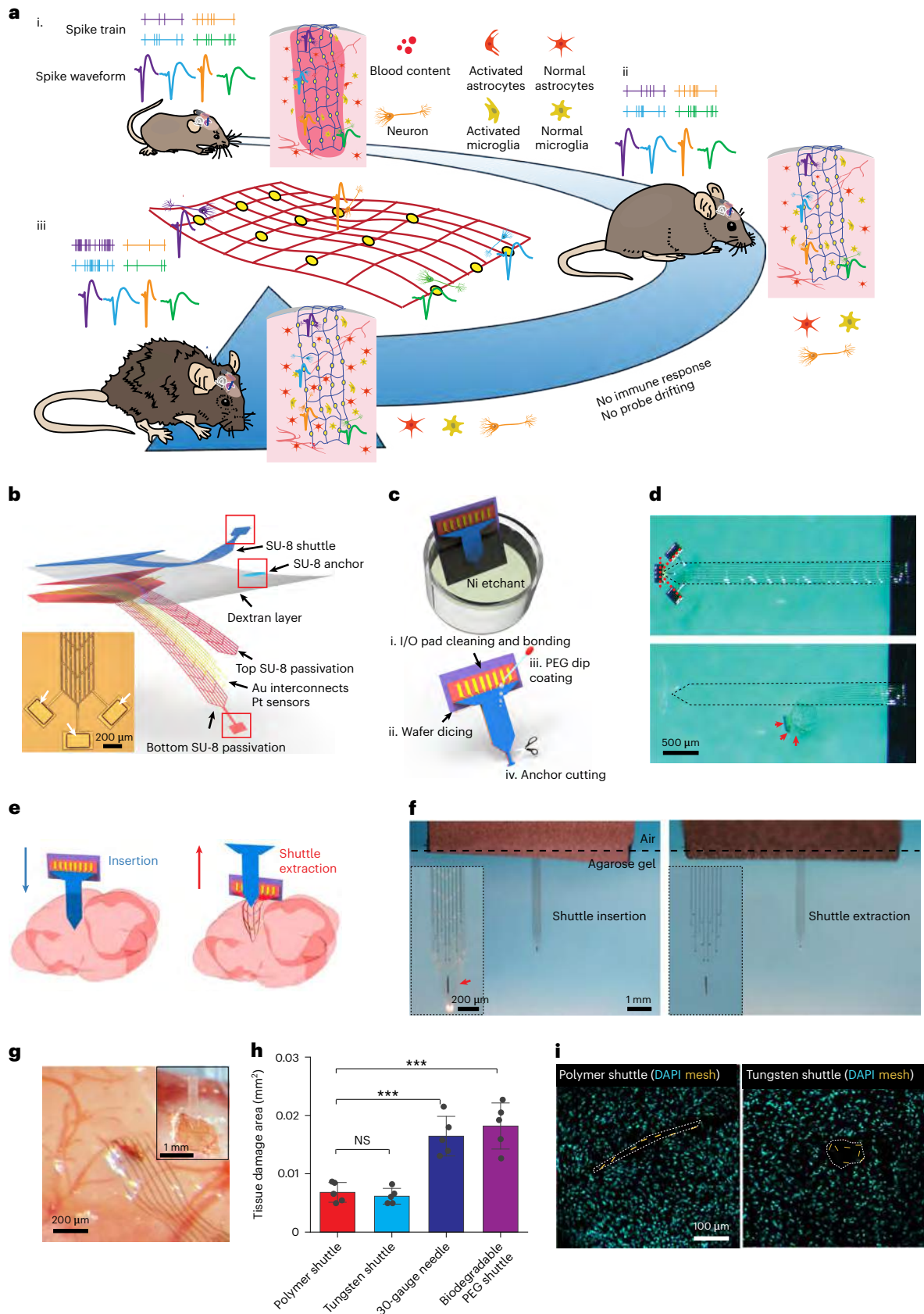
the glue was completely cured (Extended Data Fig. 2e), saline solution was applied to dissolve the dextran in the I/O region that remained to bond the polymer shuttle and silicon oxide substrate. Once both layers were removed, the polymer shuttle was carefully retracted from the brain tissue using the second manipulator under the same conditions tested in the phantom gel (Extended Data Fig. 2f), leaving the mesh electronics in the implantation sites.

Damage to the blood vessels was minimal throughout the imaging-guided implantation. To evaluate acute tissue damage, cell loss and mesh electronics distribution, we imaged the post hoc fixed and stained tissue slices immediately after implantation (Fig. 1h,i). The tissue-damaged area introduced by the ultra-thin polymer shuttle was approximately 0.0068 ± 0.0017 mm^2 (mean $\pm$ s.d., $n = 5$; Fig. 1h), significantly smaller than those from previous reported implantations using syringe injection[17,18] (0.0164 ± 0.0034 mm^2, mean $\pm$ s.d., $P = 4.7 \times 10^{-4}$, $n = 5$; Fig. 1h) or biodegradable shuttles[20] (0.0182 ± 0.004 mm^2, mean $\pm$ s.d., $P = 3.5 \times 10^{-4}$, $n = 5$; Fig. 1h). There was no significant difference compared with samples implanted with 50-μm-diameter tungsten wire[22] (0.0061 ± 0.0014 mm^2, $P = 0.5149$, mean $\pm$ s.d., $n = 5$; Fig. 1h). In addition, cross-sectional images of brain slices with implants clearly showed unfolded mesh structures covering much larger tissue regions compared to bundled ribbons made by tungsten-probe-based delivery (Fig. 1i). Compared with a previous method for flexible neural probes[17–21], the integrated 25-μm-thick polymer shuttle also markedly reduced tissue displacement during implantation and maintained the designed open structure with nearly 90% implantation yield. Moreover, this method involved minimal manual manipulations because ultra-flexible electronics were pre-attached to the polymer shuttle by lithographic fabrication. It took an average of less than 3 minutes to assemble one mesh electronics (over 20 electronics per hour) with a success rate approaching 100%.

Unfolded mesh structure 3D interwoven with neural network

We implanted mesh electronics with different sizes across multiple brain regions. The interwoven structure between the mesh and neural network remained intact at the tissue–electrode interface during tissue harvesting and post hoc fixation and staining. Rhodamine 6G dye was added to the SU-8 encapsulation layer, allowing for the imaging of the mesh structure in the brain. To explore the potential implantation capability, Fig. 2a shows a 2-mm-wide, 3-mm-long mesh electronics implanted into a mouse brain across the cortex, hippocampus and thalamus regions. The size of this device could potentially fit high-density electrodes through 3D stacking of electrodes, further increasing the number of electrodes[35] (Fig. 2a–d and Methods). A representative 3D reconstructed image of the mesh electronics in the brain tissue at 6 weeks after implantation (Fig. 2a) showed the fully unfolded, open mesh structure interwoven with neurons and astrocytes across multiple brain regions. The slight bending of the mesh suggested that tissue-like mesh electronics were flexible within the tissue. A zoomed-in view of the hippocampus CA1 region (Fig. 2b) shows a uniform distribution of neurons and astrocytes across the mesh. Notably, neurons in the cell-dense region (hippocampus) can still penetrate through the open

mesh structure (Fig. 2c), forming an intertwined tissue–electronics interface. Figure 2d shows that the size of the recording electrode (white dashed circles) was similar to the size of the soma. The subcellular feature size, tissue-level flexibility and 3D interwoven network collectively eliminated micromotion between the functional electrodes and recorded neurons[36]. Additional mesh electronics of different sizes were implanted in mouse brains and are shown in Extended Data Fig. 3a–f.

Next, we performed immunostaining characterizations to assess the distribution of key cell types around mesh electronics over time. To demonstrate that the open mesh structure reduced immune responses during chronic implantation (Fig. 2e, top), we used thin-film electronics (Fig. 2e, bottom) with the same dimensions as control and implanted them contralaterally in the same mouse brain. The bending stiffness of the thin-film electronics was higher than that of the mesh electronics (3.98×10^{-14} N m^{-2} versus 1.26×10^{-15} N m^{-2}). The brain tissue was harvested and sliced for immunostaining at 2 weeks, 6 weeks, 12 weeks and 1 year after implantation. We quantitatively analyzed horizontal brain slices implanted with 16-channel, 300-μm-wide film/mesh electronics (Fig. 2f–i) and calculated protein marker signals for neurons, astrocytes and microglia (Extended Data Fig. 3g,h) by normalizing fluorescence intensity around the implantation site with the defined baseline value (average fluorescence intensity over a range of 525–550 μm away from the electronics). Statistical analysis demonstrated a significant degradation of neuron density (NeuN) and an enhancement of astrocytes and microglia intensity (GFAP and Iba-1, respectively) near the thin-film electronics at all timepoints ($P < 0.05$ for all comparisons, $n = 5$ independent animals; Fig. 2f and Supplementary Tables 1–4). These results proved that the thin-film electronics can still trigger the proliferation of astrocytes/microglia and reduce the neuron density at the electronics–brain interface. In contrast, the open mesh structure introduced minimal damage to the surrounding neurons and negligible immune response. Notably, no significant neuron loss was detected at 2 weeks after implantation for mesh samples (Fig. 2f), suggesting minimal acute damage from the polymer shuttle implantation. In addition, the neuron density near the mesh surface remained the same at 1 year after implantation (Fig. 2f).

We further calculated the normalized fluorescence intensity within regions 100 μm away from the electronics to assess neuron loss and inflammation reaction at the different post-implantation periods (Fig. 2g–i). Compared with the open mesh structure, thin-film samples introduced significantly higher levels of astrocyte and microglia proliferation and caused neuron loss over the same period ($P < 0.05$ for all comparisons; Fig. 2g–i). Together, these results demonstrate that open mesh electronics introduced little to no inflammation and mechanical damage to the surrounding tissues as compared with thin-film electronics over year-long implantation.
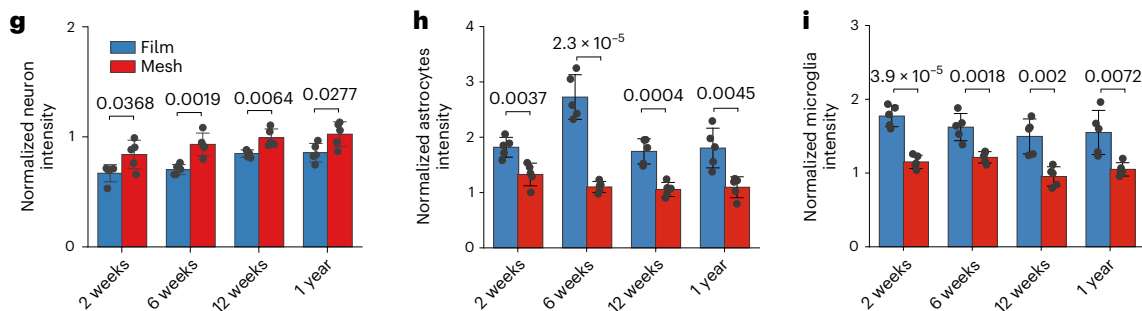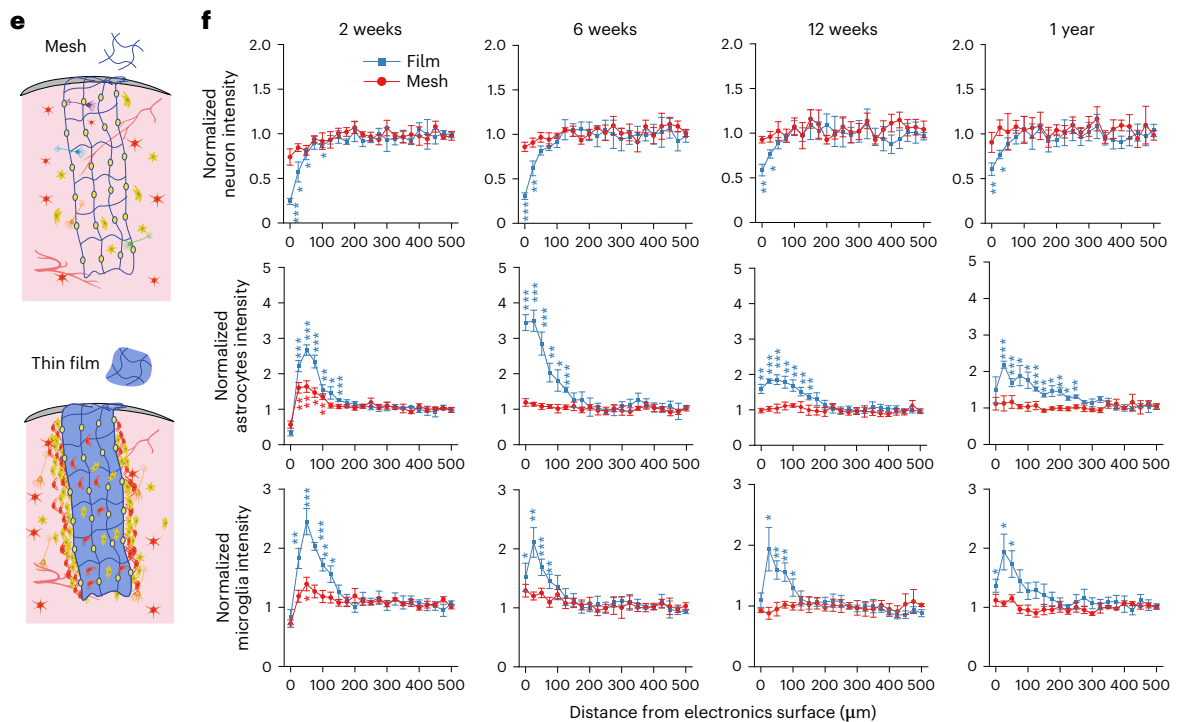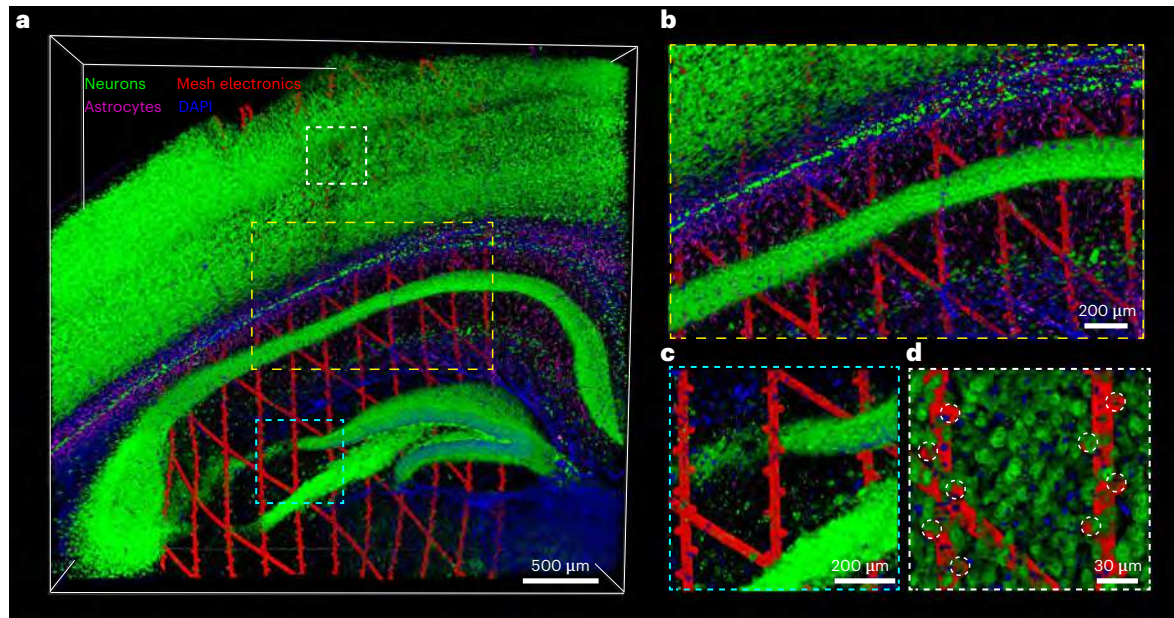
Stable recording across multiple brain regions

To assess the stability of the recording, we implanted 600-μm-wide mesh electronics with 32 channels and 300-μm-wide mesh electronics with 16 channels into different brain regions, including the somatosensory cortex and striatum (32-channel mesh electronics 1; Fig. 3a);

Fig. 2 | Unfolded mesh electronics seamlessly integrating with neuron networks across multiple brain regions. a, Representative 3D reconstructed confocal fluorescence imaging of 600-μm-thick brain tissue implanted with 2-mm-wide mesh electronics for 6 weeks. Green, purple, blue and red label neurons, astrocytes, nuclei and mesh electronics, respectively. **b–d**, Zoomed-in views of the regions highlighted by yellow (**b**), cyan (**c**) and white (**d**) dashed boxes in **a**, showing the seamless integration and interwoven structures between the mesh and the neural network. Neuron-like electrodes are highlighted by white dashed circles in **d**. **e**, Schematics illustrating unfolded 1-μm-thick mesh (top) and thin-film (bottom) electronics implanted inside brain tissue for the long-term immune response characterization. **f**, Normalized fluorescence intensity as a function of distance from the mesh/thin-film electronics–tissue

boundary at 2 weeks, 6 weeks, 12 weeks and 1 year after implantation. The relative signal was obtained by normalizing the fluorescence intensity with the baseline value defined as the fluorescence intensity over a range of 525–550 μm away from the electronics. Data are represented as mean ± s.e.m. (intensity compared with that of distance at 500 μm; significant astrocyte and microglia proliferation as well as neuron loss are indicated as *$P < 0.05$, **$P < 0.01$ and ***$P < 0.001$; P values are indicated in Supplementary Tables 1–4, two-tailed t-test, $n = 5$ independent animals). **g–i**, Normalized fluorescence intensity of neuron (**g**), astrocytes (**h**) and microglia (**i**) within 100 μm from the electronic surface. Data are represented as mean ± s.d.; individual data points are overlaid ($P < 0.05$; P values are indicated in the graphs, two-tailed t-test, $n = 5$ independent animals).

midbrain (32-channel mesh electronics 2; Fig. 3a); and visual cortex and hippocampus (16-channel mesh electronics 3; Fig. 3a). Here, we refer to a sorted unit as a 'neuron'. Intrinsic spike waveforms from isolated neuron variations from different brain regions (Fig. 3b–d) were consistent across different putative neuron types in each brain region[37,38]. Moreover, signals from different brain regions showed various neuron yield per electrode, amplitude and firing rate (Fig. 3e–g). Next, we evaluated the long-term stability of recordings from 32-channel and 16-channel
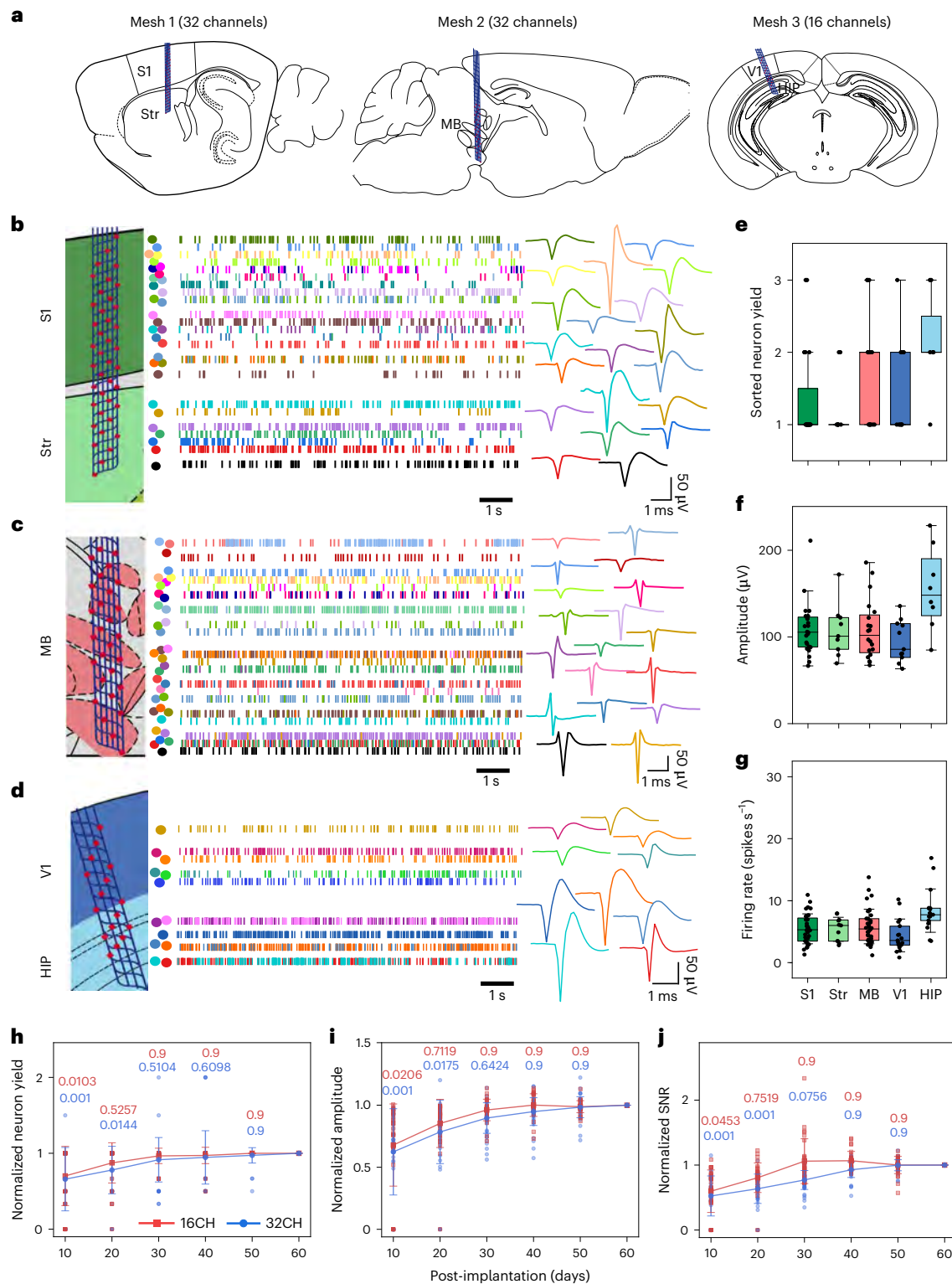
Fig. 3 | Chronically stable recording across multiple brain regions.
a, Schematics illustrating the representative brain regions implanted with mesh electronics for chronic recording. HIP, hippocampus; MB, midbrain; S1, primary somatosensory cortex; Str, striatum; V1, primary visual cortex. **b**–**d**, Schematics showing approximate mesh electrode locations across multiple brain regions (left), representative spiking raster (middle) and representative single-unit waveforms (right) from two 32-channel (**b**,**c**) and one 16-channel (**d**) mesh electronics at 60 days after implantation. Colors indicate individual neurons. The approximate electrode sites were located by post hoc histological characterization. **e**–**g**, Quantification of sorted neuron yield per electrode (**e**), average spike amplitude per electrode (**f**) and single-unit firing rate (**g**) across five

brain regions. Individual data points are overlaid (n = 72 electrodes in **e** and **f**; n = 113 neurons from five independent animals in **g**). Box: 75% and 25% quantiles. Line: median. Whiskers: the maxima/minima or median ± 1.5× interquartile range. **h**–**j**, Statistical analysis of sorted neuron yield per electrode (**h**), amplitude of spikes (**i**) and SNR (**j**) over the time course of 60 days after implantation. Data represent mean ± s.d., and individual data points are overlaid (P values are indicated in the graphs, compared with data at 60 days after implantation; one-way ANOVA, Tukey's multiple-comparisons test, n = 29 electrodes from three 16-channel mesh electronics and n = 43 electrodes from two 32-channel mesh electronics).

mesh electronics in five independent animals (*n* = 43 electrodes from two 32-channel mesh electronics and *n* = 29 electrodes from three 16-channel mesh electronics). We recorded 70 neurons from multiple regions at 10 days after implantation, which increased to 113 neurons at 60 days. The statistical results (Fig. 3h–j) showed that the neuron yield per electrode, amplitude and signal-to-noise ratio (SNR) of 300-μm-wide, 16-channel mesh electronics stabilized after 10 days after implantation. These parameters from the 600-μm-wide, 32-channel mesh electronics stabilized after 20 days after implantation, suggesting a potential size-related effect on signal stability. The dynamic process may involve neuron migration and neuronal process regeneration at the electrode–tissue interface during interwoven structure formation. These results contrast with reports from previous brain probes where amplitudes, SNR and neuron counts degraded weeks after implantation[3,4,36], suggesting that the unfolded, open mesh electronics formed a long-term stable interface with neurons and tissue.

Stable tracking of the same single-unit action potentials

To further demonstrate the ability of mesh electronics to stably track single-unit action potentials from the same neurons, we designed mesh electronics with tetrode-like electrode arrays based on previous studies[2,3,25]. Specifically, each device consisted of five arrays of six highly packed electrodes (Fig. 4a,b and Extended Data Fig. 4a) with an interelectrode distance of 30 μm within each array. This distance is similar to the size of a single-neuron soma, allowing each neuron to be simultaneously recorded by multiple nearby electrodes (Fig. 4b)[2,3]. The tetrode-like mesh electronics were implanted in the mouse primary visual cortex. Representative filtered voltage traces (300–3,000 Hz bandpass filter) showed spiking signals from two electrode arrays in an awake, head-fixed mouse (Extended Data Fig. 4b,c). An automated spike sorting (MountainSort) was used to extract single-unit spikes[26], and the waveforms from six representative units that are simultaneously captured by multiple electrodes were overlapped with the layout of the corresponding electrode array (Extended Data Fig. 4d). The overlapping result showed that the spikes from the same neurons could be simultaneously recorded by multiple nearby electrodes with different amplitudes (Extended Data Fig. 4d). The interspike interval (ISI)

distribution and auto-correlogram variability also demonstrated that the individual sorted units were well isolated (Extended Data Fig. 4e,f). Using the spatial information of electrodes and waveform amplitudes at each electrode, the relative position of the neurons to the electrode array could be estimated (Extended Data Fig. 4g) using previously reported methods[3]. In one representative mouse, 32 well-isolated individual neurons with their single-unit spikes and positions were distinguished from tetrode-like mesh electronics (Extended Data Fig. 4g). A low likelihood ratio (L-ratio) (purple, 0.017 ± 0.013, mean ± s.d., *n* = 5 electrode arrays; Extended Data Fig. 4h), high silhouette score (red, 0.77 ± 0.09, mean ± s.d., *n* = 5 electrode arrays; Extended Data Fig. 4h) and <10% refractory period violations[2] (Extended Data Fig. 4i; refractory period is defined as an ISI <1.5 ms, 1.26% ± 0.93%, mean ± s.d., *n* = 32 neurons) demonstrated that the sorted units were isolated single-unit activity rather than multi-unit activities[2]. Scatter plots of peak-to-peak amplitudes of waveforms (Extended Data Fig. 5a and Methods) and projected waveforms of the first principal component (PC) axis of each electrode from all pairs of electrodes within an array[25] (Extended Data Fig. 5b and Methods) supported the quality of single-unit isolation. Together, these results proved the ability of mesh electronics to record single-unit action potentials from the same neurons.

Then, we assessed the long-term stability of single-unit recording from the same neurons based on spike waveforms and estimated positions of neurons in head-fixed, behaving mice over a 7-month chronic recording (Fig. 4a,b). We started the recording from five mice at 1 month after implantation (mice were then 5 months old; Fig. 4a). We extracted 102 well-isolated neurons at the beginning of the recording for analysis using established methods (Methods)[2,3,19,27,26]. The units with firing rate less than 0.1 spikes per second were excluded from our analysis[2]. Results showed that the shape of each single-neuron waveform and its projection in the 2D embedding space of uniform manifold approximation and projection (UMAP)[24] were stable over the course of recording (Fig. 4c,d and Methods). The clusters of sorted spikes in the UMAP space showed nearly constant positions and were well separated from each other throughout the chronic recording (Fig. 4d and Methods). The ISI distribution of each neuron was stable

Fig. 4 | Chronically stable tracking of single-unit action potentials from the same neuron using mesh electronics with tetrode-like electrode arrays. a, Schematics showing the long-term stable electrical recording of the same neuron (left) and simultaneous recording of single-unit activities from the same neurons by multiple recording sites (right) enabled by the minimally invasive and fully unfolded tissue-level flexible mesh electronics with tetrode-like electrode arrays. **b**, Schematics showing validation of long-term stable tracking of the single-unit action potentials from the same neurons by examining the waveform similarity and estimated position of neurons (single-unit waveform centroid computed by using spatial average across electrode positions weighted by the mean waveform amplitude at each electrode) identified by tetrode-like mesh electronics. **c**, Average single-unit waveforms at each of the recording electrodes from one representative tetrode-like mesh electronics (five electrode arrays) over the course of 7-month recording. Waveforms recorded from each month are plotted as a gradient color. **d**, Time evolution of the single-unit spikes from the same neurons in **c**. The *x* and *y* axes denote the first and second UMAP dimensions, respectively, and the *z* axis denotes months. **e**, Proportion of refractory period violations (2.05% ± 1.49%, mean ± s.d., *n* = 102 units from five mice). Refractory period violation is defined as an ISI <1.5 ms. **f**, Waveform similarity for each single neuron across all the recording sessions (0.97 ± 0.04, mean ± s.d., *n* = 92 units from five mice). **g**, Statistical summary of waveform-defined stable neurons across entire recording sessions in five mice (90.77% ± 5.47% same neurons defined by waveform similarity can be stably tracked throughout 7-month recording. Data are presented as mean ± s.d.). The yield was averaged by five mice with 92 stable units out of 102 units. Inset: schematics showing identification of the recorded stable neurons based on their waveform similarity. The stable neurons were defined as those with the Pearson correlation within units greater than that across units between two

recording sessions. **h**, Single-neuron waveform centroids throughout 7-month recording from a representative mouse. The centroid for each single neuron was isolated on month 5 (blue circles) compared with that on months 7, 9 and 11 (red circles, rows 1–3, respectively). Gray circles indicate the positions of the mesh electrodes. **i**, Average displacement of single-neuron centroids from five mice between month 5 (blue circle, defined at origin) and months 7, 9 and 11 (red circles, rows 1–3, respectively). Gray contours indicate quintile boundaries of the distribution of centroid position displacement for the population (month 5 versus month 7, *n* = 97 single units; month 5 versus month 9, *n* = 95 single units; month 5 versus month 11, *n* = 93 single units). **j**, Left: the cumulative distribution of within-unit centroid displacement (red) between month 5 and months 7, 9 and 11 (rows 1–3, respectively) and across-unit centroid displacement within a day (black) for five mice. Average month 5 versus month 7 within-unit = 1.63 μm (Q1 = 0.77 μm, Q3 = 2.01 μm), across-unit = 24.57 μm (Q1 = 17.61 μm, Q3 = 32.06 μm); month 5 versus month 9 within-unit = 2.51 μm (Q1 = 1.23 μm, Q3 = 3.46 μm), across-unit = 24.65 μm (Q1 = 17.86 μm, Q3 = 31.97 μm); month 5 versus month 11 within-unit = 2.61 μm (Q1 = 1.26 μm, Q3 = 3.48 μm), across-unit = 24.54 μm (Q1 = 17.31 μm, Q3 = 32.24 μm). For all comparisons, *P* < 0.001. *P* values are indicated in the graphs, two-sided Wilcoxon rank-sum test, *n* as in **i**. Inset at right: *x* axis 0–10 μm. **k**, Statistical summary of vertical and horizontal displacement of the same neurons across the entire recording sessions (vertical displacement = 1.26 ± 0.48 μm, horizontal displacement = 0.85 ± 0.44 μm, mean ± s.d., *n* as in **i**). **l**, Statistical summary of stability assessed by single-neuron estimated positions across 7 months in five mice (91.83% ± 5.92%, mean ± s.d., *n* = 5 mice). Schematics showing characterization of the same neurons based on neurons' estimated positions. The stable neurons (93 out of 102 neurons) were defined as those with the displacement smaller than 10 μm across two consecutive recording sessions.
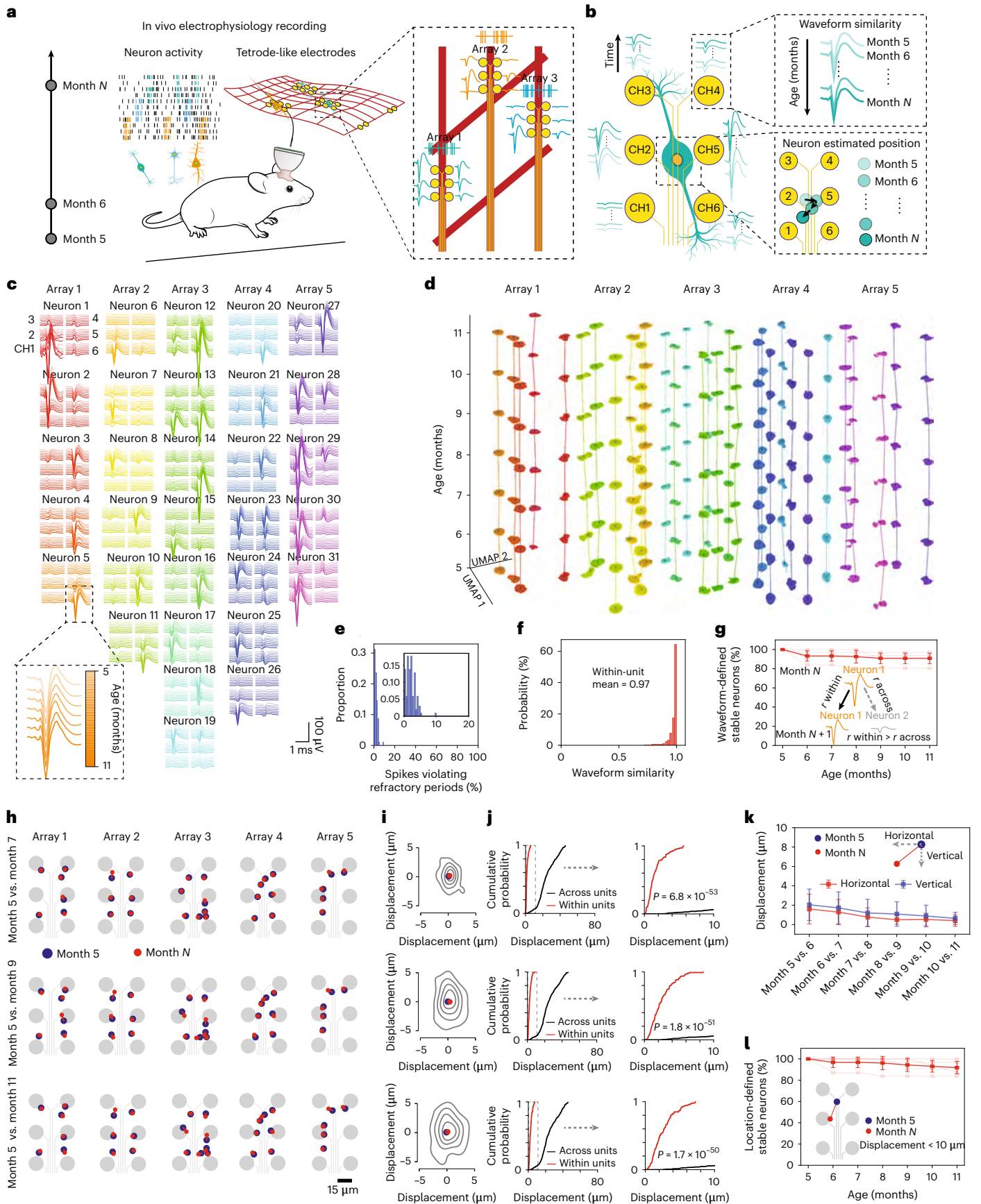
over time (Extended Data Fig. 6a and Methods), and the fraction of refractory period violations across all neurons was 2.05% ± 1.49% (ref. [2]) (Fig. 4e; mean ± s.d., $n = 102$ neurons from five independent mice), demonstrating well-isolated single units continuously recorded throughout the chronic recording. Single-unit waveforms from the same neurons were highly similar and almost indistinguishable within each neuron (0.97 ± 0.04 across all recording sessions from five mice, mean ± s.d.; Fig. 4f and Methods). L-ratio[28] (Extended Data Fig. 6b; 0.006 ± 0.006, mean ± s.d., $n = 18$ electrode arrays) and silhouette score[29] (Extended Data Fig. 6b; 0.84 ± 0.06, mean ± s.d., $n = 18$ electrode arrays) analysis further confirmed good unit separation and accurate identification of individual units. We examined chronic recording stability of the same units by comparing the waveform similarity within each neuron (r_{within}) with the similarity across different neurons (r_{across}). A neuron was considered stable if r_{within} was greater than r_{across} across two recording sessions in 2 months[2,3]. As a result, 92 out of all 102 neurons were stable across 7-month recording (Fig. 4g; 90.77% ± 5.47%, mean ± s.d.; percentage was averaged by each mouse). Statistical analysis of single-neuron recording stability by firing rate, SNR and five waveform features (Extended Data Fig. 6c–g; amplitude, duration, peak–trough (PT) ratio, repolarization slope and recovery slope)[38] showed that most (>80%) of neurons' waveform features did not change significantly over time ($P > 0.05$, two-tailed t-test; Extended Data Fig. 6e–g and Methods). Notably, the consistent SNR demonstrated that the electrode-to-cell interface did not degrade during the entire recording period (Extended Data Fig. 6e, red). The estimated positions of neurons[3] were nearly constant over the 7-month recording (Fig. 4h and Extended Data Fig. 6h). Specifically, the average displacement of the estimated neuron positions across the longest recording interval was 2.61 μm (Fig. 4i,j; first quartile (Q1) = 1.26 μm, third quartile (Q3) = 3.48 μm; $P < 0.001$ compared to the displacement across units, two-tailed t-test, month 5 versus month 11, $n = 93$ neurons from five mice), indicating that the displacement of the mesh electrodes with respect to the neurons was negligible (Fig. 4i,j and Extended Data Fig. 6i,j). The vertical and

horizontal displacement across all recording periods showed that the displacements were much smaller than the size of the neuron soma (Fig. 4k; vertical displacement = 1.26 ± 0.48 μm, horizontal displacement = 0.85 ± 0.44 μm, mean ± s.d.). Statistically, 91.83% ± 5.92% of neurons (Fig. 4l; mean ± s.d., $n = 5$ mice, 93 out of 102 neurons) showed nearly constant positions (<10 μm) throughout the 7-month recording. Together, all the results demonstrated the ability of the mesh electronics to long-term stably track single-unit action potentials from the same neurons.

## Tracking behavior-dependent activities from the same neurons

We further examined the ability of mesh electronics to stably record the behavior-dependent single-unit action potentials from the same neurons in the primary visual cortex by measuring the visual stimulus-dependent peristimulus time histogram (PSTH) (Fig. 5a). We selected a battery of static gratings (Fig. 5b,c–h) with six orientations and three spatial frequencies, as well as a group of dynamic gratings (Fig. 5b,i–n) with 12 orientations as visual stimuli, based on the assumption that neurons in the primary visual cortex show distinct responses to these different visual stimuli and minimal representational drifts of population dynamics[2,39]. Representative neural responses showed stable and distinct patterns to different static and dynamic gratings over the course of the entire recording. First, different neurons presented disparate responses to the same stimulus (Fig. 5c). For example, neurons 1, 2 and 3 showed a slightly positive response, a fast positive response and a negative response to static grating of 90° over time, respectively (Fig. 5c, column 3). Second, the same neurons responded differently to different stimuli or showed distinct response features to one stimulus (Fig. 5i). For example, neuron 4 showed positive responses to 0° and 180° dynamic gratings but no response to 90° over time (Fig. 5i, row 1), and neuron 5 showed multiple distinct response peaks to the 90° dynamic grating (Fig. 5i, column 2 on neuron 5). In addition, the heat maps also showed the patterned selectivity of neurons to all

Fig. 5 | Chronically stable tracking of visual stimulus-dependent neural activities from the same neurons. a, Schematics showing the mesh electronics implanted in the primary visual cortex (V1). Activities of V1 neurons were recorded with visual stimulus over 7 months. **b**, Schematics summarizing orientation and spatial frequency of neuronal responses to the static and dynamic grating stimuli. **c–h**, Static grating stimulus-dependent single-unit activities from the same neurons. **c**, PSTH of representative neurons in response to three static gratings (orientations from left to right, 0°, 60° and 90°, respectively) presented for 1 second (dark blue), averaged from $n = 15$ repetitions, on each of recording sessions over 7 months. **d**, Correlation coefficients of representative neurons derived from split-half analysis (odd versus even trials) comparing visual responses to static gratings recorded within a single recording session (black), between two recording sessions from different months (red) and after shuffling the stimulus order (blue). For the three representative neurons, P values are indicated in the graphs; $n = 7$ recording sessions across all recording periods. For all responsive neurons to static gratings, r_{across} versus $r_{shuffle}$, $P = 3.7 \times 10^{-26}$ and r_{within} versus $r_{shuffle}$, $P = 1.3 \times 10^{-67}$, two-sided t-test, $n = 47$ neurons from all recording sessions. **e**, Visual response of each neuron to static gratings in the first recording was matched with its own response and with the visual response of the physically closest other units in following months (month 5 versus month 7: 52/54 neurons; month 5 versus month 9: 50/54 neurons; month 5 versus month 11: 53/54 neurons). **f**, Summary of static gratings defined stability (**e**) of well-isolated units across 7-month recording in five mice. The visual response of each stable unit was matched with its own response across all recording periods. Forty-seven stable responsive neurons were recorded out of all 54 neurons over 7 months. Data are presented as mean ± s.d. **g**, Population summary comparing split-half correlations computed for trials drawn from the same neurons versus different neurons over 7-month recording. Dark blue: correlation r from the same neurons (0.50 ± 0.28, mean ± s.d., $n = 47$ responsive neurons to static gratings); light blue: correlation r from all pairwise combinations of different neurons responding to the same stimuli (0.03 ± 0.26, mean ± s.d., $n = 47$ responsive neurons to static gratings). **h**, ROC curve plots

(area = 0.89) of false alarms (x axis) against hits (y axis). Correlation and ROC between the same neurons and different neurons for each month are included in Extended Data Fig. 8. **i–n**, Dynamic grating stimulus-dependent single-unit activities from the same neurons. **i**, PSTH of representative neurons in response to different dynamic gratings presented for 2 seconds (dark red), averaged from $n = 15$ repetitions, on each recording session over 7 months. Black arrows show the orientation of dynamic gratings. **j**, Correlation coefficients of representative neurons derived from split-half analysis (odd versus even trials) comparing visual responses to dynamic gratings recorded within a single recording session (black), between two recording sessions from different months (red) and after shuffling the stimulus order (blue). For the three representative neurons, P values are indicated in the graphs, $n = 7$ recording sessions across all recording periods. For all responsive neurons to dynamic gratings, r_{across} versus $r_{shuffle}$, $P = 1.2 \times 10^{-50}$, and r_{within} versus $r_{shuffle}$, $P = 3.0 \times 10^{-266}$, two-sided t-test, $n = 57$ neurons. **k**, Visual response of each neuron to dynamic gratings in the first recording was matched with its own response and with the visual response of the physically closest other units in the following months (month 5 versus month 7: 60/63; month 5 versus month 9: 60/63; month 5 versus month 11: 60/63). **l**, Summary of dynamic gratings defined stability (**k**) of well-isolated units across 7-month recording in five mice. Visual response of each stable unit was matched with its own response across all recording periods. Fifty-seven stable responsive neurons were recorded out of all 63 neurons over 7 months. Data are presented as mean ± s.d. **m**, Population summary comparing split-half correlations computed for trials drawn from the same neurons versus different neurons over 7-month recording. Dark red: correlation r from the same neurons (0.72 ± 0.23, mean ± s.d., $n = 57$ responsive neurons to dynamic gratings); light red: correlation r from all pairwise combinations of different neurons responding to the same stimuli (0.18 ± 0.33, mean ± s.d., $n = 57$ responsive neurons to dynamic gratings). **n**, ROC curve plotting (area = 0.91) of false alarms (x axis) against hits (y axis). Correlation and ROC between the same neurons and different neurons in each month are included in Extended Data Fig. 8.

the stimuli (Extended Data Fig. 7a,b). These results demonstrated that the recorded neurons maintained stable visual stimulus-dependent responses to the same orientation and spatial frequency over time (Fig. 5c,i and Extended Data Fig. 7a,b).

To quantify the month-to-month consistency of visual responses, we calculated a split-half correlation coefficient for each recording by dividing the trials into two subsets. Here, the correlation coefficients r_{within}, r_{across} and $r_{shuffle}$ were calculated based on the averaged
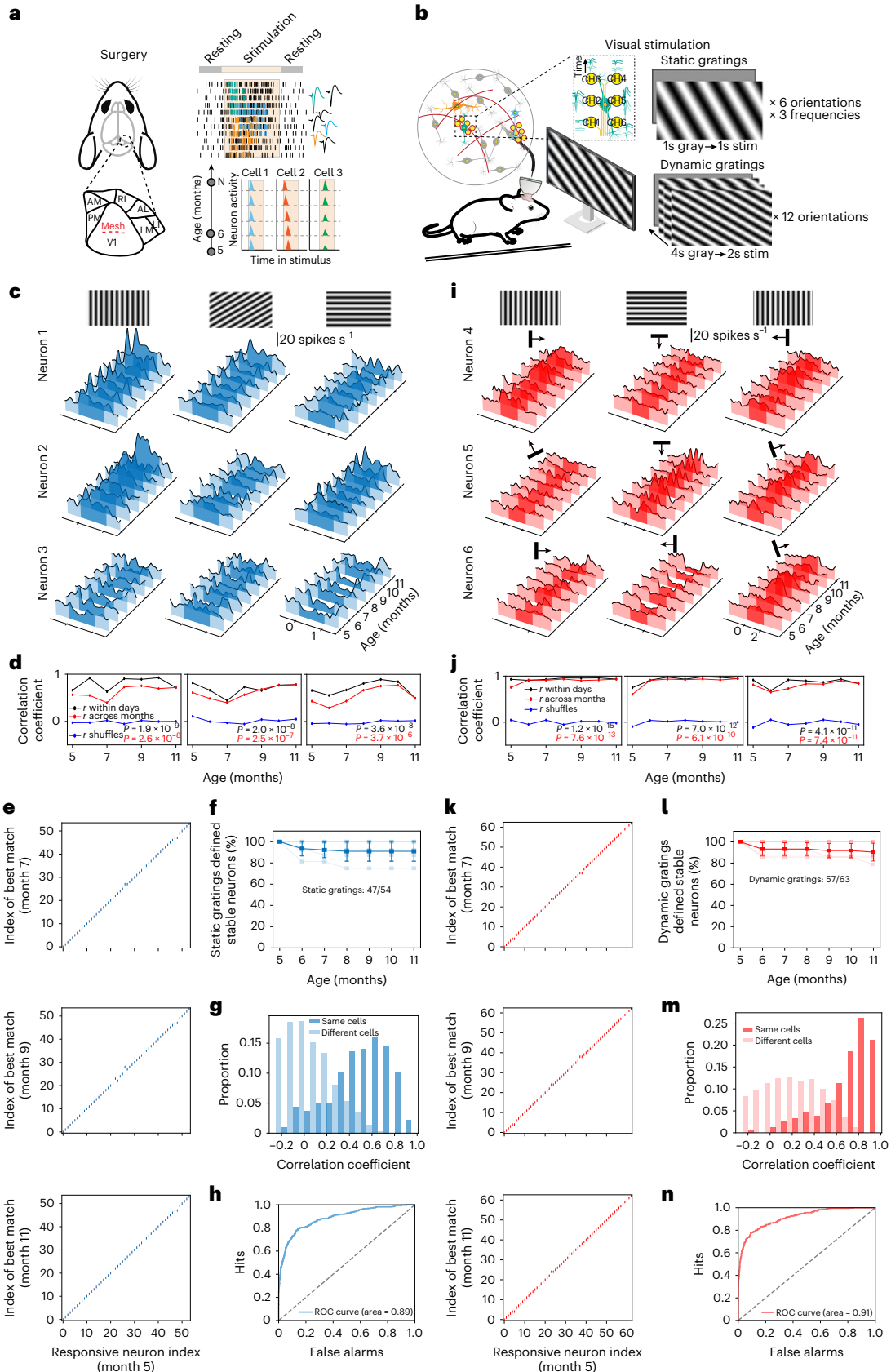
responses to all static and dynamic gratings between odd versus even trials, between two consecutive months and after shuffling the identity of all stimuli, respectively (Fig. 5d,j and Methods)[27]. Results showed that r_{across} was slightly smaller than r_{within} (Fig. 5d,j), and r_{within} and r_{across} were both significantly greater than $r_{shuffle}$ ($P < 0.001$ for all comparisons, two-tailed t-test; Fig. 5d,j), which suggest that the visual stimulus-dependent recording is stable over time but may exhibit small intrinsic representational drift over time, consistent with previous reports[2,39].

We then assessed whether mesh electronics-recorded and algorithmically identified units represented the same neurons by comparing their responses to the same stimulus across two recording sessions with the responses of the nearest neighboring neuron[2] (Fig. 5e,k and Extended Data Fig. 7c,d). Results showed that most visual stimulus-dependent neurons (Fig. 5f, 47/54 responsive neurons for the static gratings; Fig. 5l, 57/63 responsive neurons for the dynamic gratings) were successfully tracked over the course of 7-month recording. However, it is possible that, if neurons in close proximity have closely matching response patterns to stimuli (that is, orientation or spatial frequency), two different nearby neurons encountered on multiple months might be mistakenly considered as the same neuron. To further assess this possibility, we quantified the within-unit (same neurons) consistency of visual responses by computing a correlation coefficient between responses to all stimuli on odd versus even trials (Fig. 5g, 0.50 ± 0.28, mean $\pm$ s.d., $n = 47$ response neurons to static gratings; Fig. 5m, 0.72 ± 0.23, mean $\pm$ s.d., $n = 57$ responsive neurons to dynamic gratings). We then calculated the correlation coefficient across different units (different neurons, Fig. 5g, 0.03 ± 0.26, mean $\pm$ s.d.; Fig. 5m, 0.18 ± 0.33, mean $\pm$ s.d.). The correlation of the same-neuron responses was significantly higher than that of the across-neuron responses, indicating that neurons in one neighborhood have distinct visual responses ($P < 0.001$ for both visual stimuli, two-tailed t-test). We also applied receiver operating characteristic (ROC) analysis to characterize the separability of a binary classification system where a higher area under the curve (AUC) typically represents higher separability[27]. The AUC of static and dynamic gratings were 0.89 and 0.91 (AUC > 0.5 represents good separability), respectively (Fig. 5h,n), indicating good isolation of different neurons responsive to visual stimuli. Distinct within-unit and across-unit correlation coefficients and ROC curves on each month (Extended Data Fig. 8a–d) confirmed the good separability of different responsive neurons. These results demonstrate the ability of mesh electronics to long-term stably track the behavior-dependent single-unit activities from the same neurons.

Tracking the same neuron's activity over the adult life of mice

We tested the recording capability of mesh electronics in the brains of six mice over their entire adult life. To fully leverage the stable interface with the brain, mesh electronics with sparsely distributed electrode arrays were used (Fig. 1b). Two mice were implanted with 16-channel mesh electronics and four with 32-channel mesh electronics (5 months to 17–18 months of mouse age). Compared to 5-month-old mice with

glossy brown fur, the aged mice (18 months old) exhibited significantly normal and healthy aging characteristics, including weight gain, barbering around the eyes and thinning gray fur in the dorsal back skin (Extended Data Fig. 9a–f).

We defined a neuron as stable if it was recorded successfully across all sessions and the total number of neurons as the number of units sorted from all sessions. We excluded the units with firing rate less than 0.1 spikes per second from our analysis[2]. As a result, 111 out of 144 neurons from six mice were identified as stable neurons across all recording sessions from 5 months to 17–18 months of mouse age. We used established methods to assess the stability of the signals[19,24,40]. The UMAP clusters for each sorted spike showed nearly constant positions and were well separated from each other through >1-year recordings (Fig. 6a; additional replication in Extended Data Fig. 10a and Methods). In addition, the corresponding single-neuron waveform shapes (Fig. 6b and Extended Data Fig. 10b) as well as their firing dynamics (that is, ISI) were stable (Extended Data Fig. 10c and Methods). The electrode interfacial impedances remained relatively constant values over time (Fig. 6c), indicating stable electrical and mechanical properties of mesh electronics over the course of the year-long recording[41]. The low fraction of refractory periods ($0.17\% \pm 0.33\%$, mean $\pm$ s.d., $n = 144$ neurons from six mice; Fig. 6d) confirmed the single-unit recording. During the spontaneous activity recording, 2.7% of neurons had firing rates that were between 0.1 and 1 spikes per second (Supplementary Fig. 1a, dark blue). This low firing rate may result in inadequate reporting of ISI violations when using fractions of ISI violations. To address this issue, we calculated ISI violations based on the relative firing rate of the hypothetical neurons that are generating these violations[42]. The low ISI violations (0.0539 ± 0.1240, median $\pm$ s.d., $n = 111$ neurons; Supplementary Fig. 1b and Supplementary Table 5) further demonstrated the well-isolated single-unit recording[43]. Single-unit waveforms were highly similar and almost indistinguishable within themselves (0.98 ± 0.03 across all recording sessions from six mice, mean $\pm$ s.d., $n = 111$ neurons; Fig. 6e and Methods). L-ratio[28] (0.002 ± 0.004, mean $\pm$ s.d., $n = 31$ electrodes; Fig. 6f) and silhouette score[29] analysis (0.73 ± 0.09, mean $\pm$ s.d., $n = 31$ electrodes; Fig. 6f and Methods) confirmed that the signals were sufficiently separated to permit isolation of single units. Statistical analysis on single-unit waveform similarity stability examined by five waveform features (amplitude, duration, PT ratio, repolarization slope and recovery slope; Fig. 6g)[38] and SNR showed that their average values were nearly constant, and most (85.23% from six mice, $P > 0.05$, two-sided t-test; Fig. 6h–j and Methods) of the neurons' five waveform features did not change significantly over time. Notably, the consistent SNR demonstrated that the electrode-to-cell interface was not degraded during the year-long recording (Fig. 6h, red). Percentages of stable neurons over year-long recording on individual mice are shown in Fig. 6k. We used a machine-learning-based algorithm to examine the stability of our recordings in an unbiased manner. The algorithm examined the entire spike waveform rather than manually selected features. The results showed that most of the neurons (86%, $n = 144$ neurons from six mice) were stable over time (Supplementary

**Fig. 6 | Tracking of neural activites from the same neurons over the entire adult life of mice. a**, Time evolution of single units clustered by Leiden over the entire adult life of mice from the mature adult (5 months) to the aged (18 months) stage. The x and y axes denote the first and second UMAP dimensions, respectively, and the z axis denotes mouse age in months. Color scheme is maintained throughout. **b**, Time-course analysis of the average waveforms of single-neuron action potential in the Leiden clustering results in a. Waveforms are represented as mean $\pm$ s.d. **c**, Time-dependent electrode interfacial impedance at 1 kHz over the time course of implantation. Data are represented as mean $\pm$ s.d., and individual data points are overlaid (mean $\pm$ s.d., $n = 25$ electrodes). **d**, Distribution of refractory period violations over 144 neurons from six mice. The fraction of refractory period violations across year-long recording was $0.17\% \pm 0.33\%$, mean $\pm$ s.d. **e**, Waveform similarity for every single neuron across all recording sessions (0.98 ± 0.03, mean $\pm$ s.d., $n = 111$ units from

six mice). Inset: overlaid average waveforms across all recording sessions for one representative neuron. **f**, L-ratio (0.002 ± 0.004, mean $\pm$ s.d., $n = 31$ electrodes) and silhouette score (0.73 ± 0.09, mean $\pm$ s.d., $n = 31$ electrodes) showing the clustering quality for the single-unit action potentials from identified neurons. Data are represented as mean $\pm$ s.d., and individual data points are overlaid. The blue and red dashed lines label L-ratio of 0.05 and silhouette score of 0.5, respectively, commonly taken as a threshold of high cluster quality. **g**, Schematic showing features extracted from the single-unit action potential waveform used for the analysis in **h–j**. **h–j**, SNR (red in **h**), amplitude (blue in **h**), duration (blue in **i**), PT ratio (red in **i**), repolarization slope (red in **j**) and recovery slope (blue in **j**) of all the single-unit spikes as a function of time. Data are represented as mean $\pm$ s.d., $n = 111$ neurons from six mice. Individual data points are overlaid. **k**, Number of the same neurons that were stably recorded (111 out of 144 neurons from six mice) as a function of recording interval duration.

Figs. 2a–f and 3a–d). Collectively, all these results indicated that the waveforms were stably recorded from the same neurons over the entire recording period.

We compared the recording stability of mesh electronics with sparsely distributed electrodes to that of mesh electronics with tetrode-like electrodes using metrics based on previous data analysis (Supplementary Fig. 4a–f). These results showed that the recording stability of mesh electronics with sparsely distributed electrodes is similar to or slightly higher than that of mesh electronics with tetrode-like mesh electronics (Supplementary Fig. 4a,b), suggesting that the size
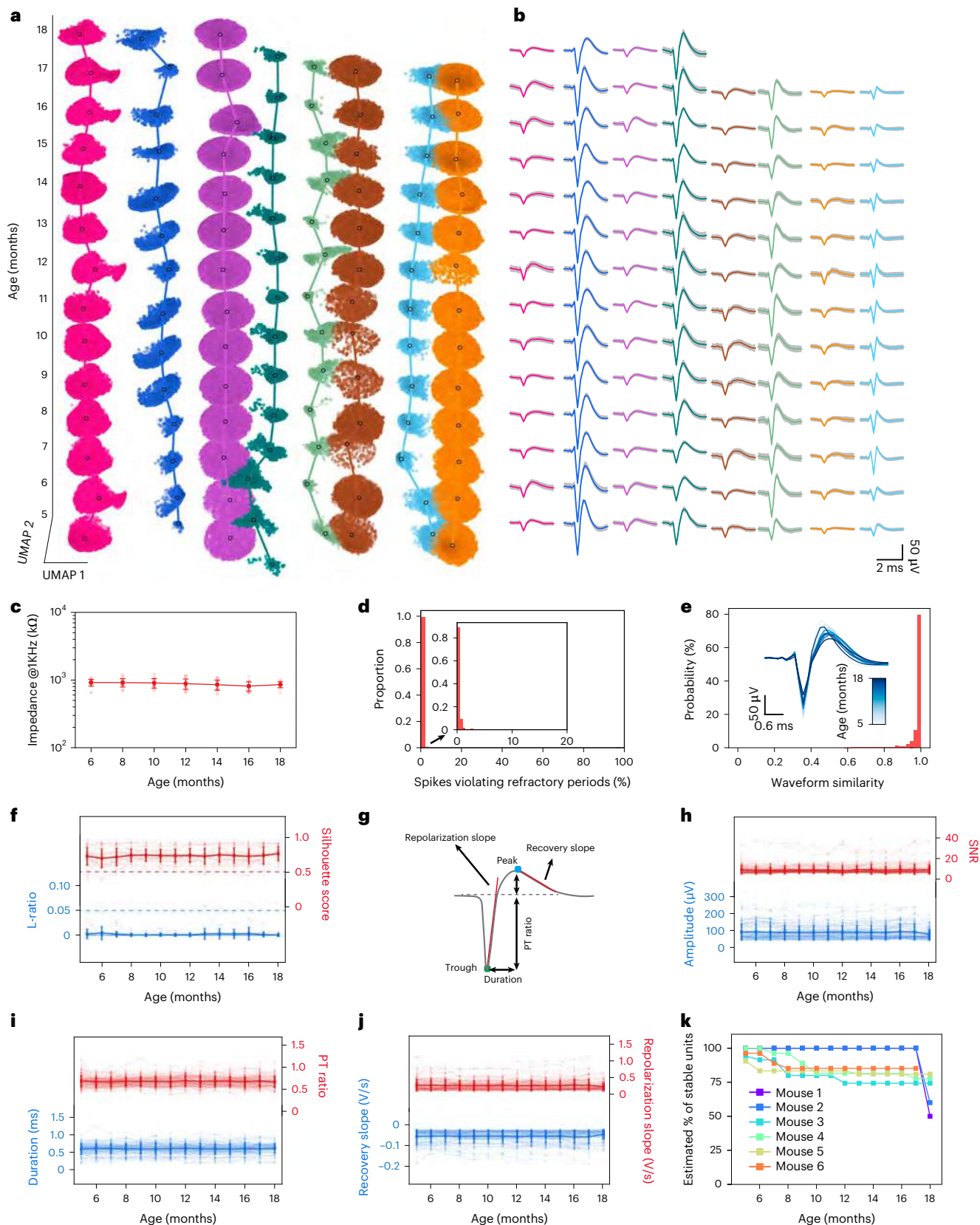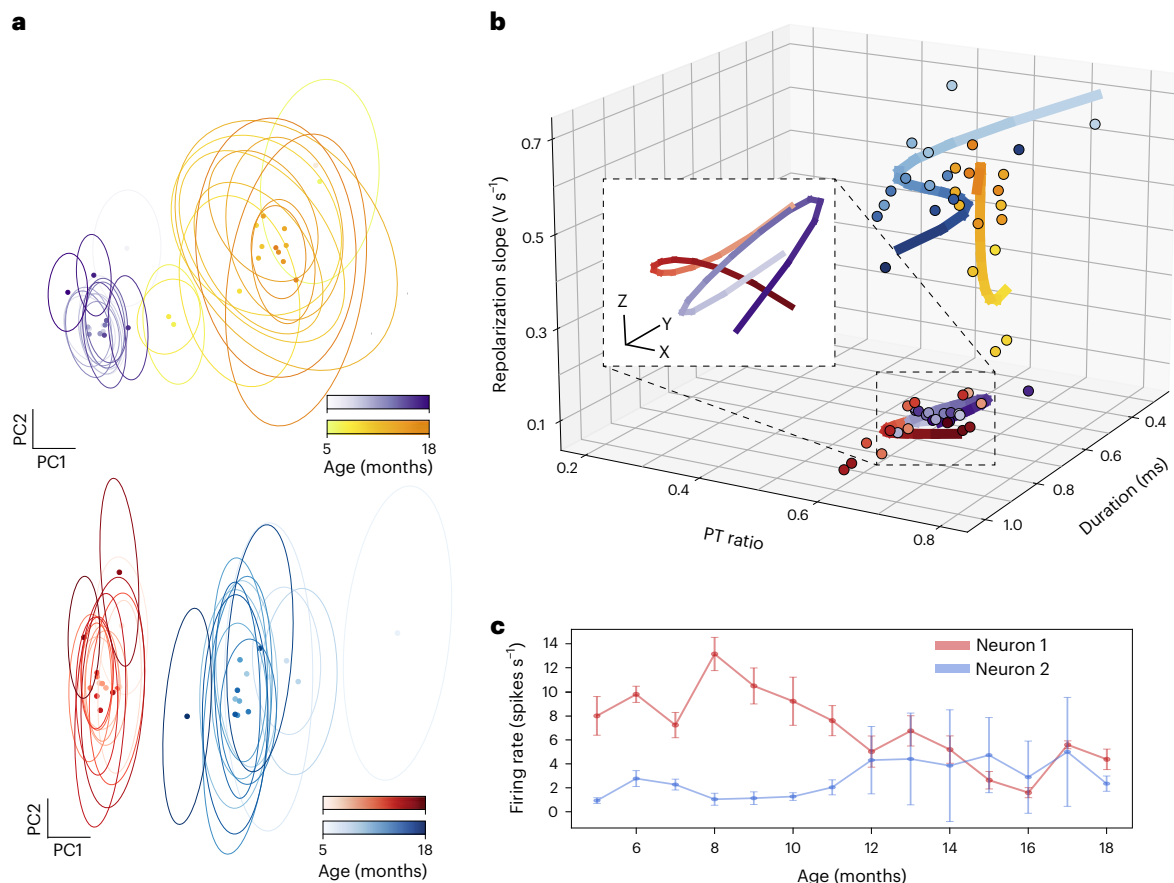
Fig. 7 | Tracking of age-associated single-unit waveform changes. a, PCA of representative waveforms of neurons showing stable (purple and red) and progressively changing (orange and blue) electrophysiological behaviors. Dots and ovals represent the centers and ±2 σ of PC clusters, respectively. Average cluster centroid successive position shifts: 0.47 σ_{purple}, 0.58 σ_{red}, 1.96 σ_{orange} and 2.63 σ_{blue}. Low values indicate stable cluster centroid position across time relative to single cluster, whereas high values suggest time evolution of corresponding cluster centroids and associated single-unit action potential waveforms. In both cases, a single electrode channel tracked stable (<1 σ) and time-evolving single-neuron action potential waveforms. **b**, Trajectory analysis conducted with a B-spline interpolation of representative waveform features over the time course of implantation for the same neurons. Non-correlated features were chosen after performing correlation analysis (duration, PT ratio and repolarization slope in Supplementary Fig. 5a). Dots with the same color represent mean values of features calculated by the waveforms associated with the same color-coded neurons from data shown in **a**. Trajectories highlight the representative neurons shown in **a**, showing slow progressive and aging-associated electrophysiological properties. Inset: zoomed-in view of purple and red trajectory. Scale bar, $x = 0.25$, $y = 0.1$, $z = 0.01$. **c**, Time evolution of the firing rate of two representative neurons over the adult life of mice, $n = 5$ recording sessions. Data are represented as mean ± s.d.

and geometry of the electrode region may have an impact on the signal stability.

Long-term study the brain aging at the single-neuron level

Analysis of the single-unit action potentials recorded from the same neurons throughout the adult life of mice offered an opportunity to observe aging-associated electrophysiological changes at the single-neuron level. Overlapping clusters of spikes across the recordings in the principal component analysis (PCA) space showed that some electrodes can simultaneously record multiple neurons. We found that, whereas one neuron (that is, 1.96 σ_{orange}, 2.63 σ_{blue}; Fig. 7a and Supplementary Methods) showed slight changes in its clusters of spikes over time, another neuron (that is, 0.47 σ_{purple}, 0.58 σ_{red}; Fig. 7a) remained stable throughout the recording, suggesting stable recording of this neuron by the electrode. We analyzed the time evolution of average neuron waveforms in a representative 3D feature space (Fig. 7b and Supplementary Fig. 5a). We observed that 15% of neurons (that is, orange and blue) displayed a clear trajectories trend, whereas others (that is, purple and red) remained the same (Fig. 7b). We also analyzed the evolution of the spike waveforms by quantifying the intrinsic state of the

spike waveforms at different recording times using 'pseudotime'[44] and found that the pseudotime of the stable neurons remained constant, but the pseudotime of unstable neurons increased over the course of the recording (Supplementary Fig. 5b). Finally, we could identify neurons with aging-associated increase and decrease in firing frequency (Fig. 7c; $P < 0.05$, Pearson correlation). Overall, these qualitative and quantitative results suggested that mesh electronics may be useful for studying the aging-related electrical activity evolution from the same neurons in behaving animals.

Discussion

We developed ultra-thin shuttle monolithically integrated mesh electronics that can be implanted across multiple brain regions with an open mesh structure and minimal tissue damage. The open mesh structure can be interwoven with the neural network in the brain, enabling immune-response-free implantation and long-term stable 3D electrode–neuron integration. This structural stability allowed us to track the single-unit action potentials of the same neurons over the entire adult life of mice until natural death as supported by our data analyses, which, to our knowledge, has not been achieved by other

state-of-the-art electrodes. Compared with the previous high-density array, mesh electronics can stably track the same neurons without the need for post hoc drift correction over long-term recording[2]. The unique ability to successfully track individual neurons in a chronically stable manner over the entire adulthood of the mice allowed for a continuous view of aging-associated changes in neural activity. We think that long-term stable tracking of single-neuron activity patterns across a stably recorded population of cells will open new opportunities for neuroscience study, next-generation brain–machine interface and bioelectronic medicine. This technology also has the potential to uncover long-term neural processes, such as development, learning, recovery from injury, neurodegeneration and age-related cognitive decline. However, the current recording system still requires wiring between the amplification and data acquisition system and implanted electronics, which could limit the free movement of mice in a 3D environment[45]. A potential solution is the integration of a high-bandwidth wireless data transmission system, which could greatly improve the capability of our flexible electronics for the behavioral study of freely moving animals. In the future, we envision that the incorporation of stretchability and wireless transmission capabilities into our device design, which can adapt to the large volume change during early brain development and the complex 3D environment with free movement of mice, will allow us to achieve long-term stable tracking of neural activity from the same neurons over the entire lifespan of freely moving animals.

Online content

Any methods, additional references, Nature Portfolio reporting summaries, source data, extended data, supplementary information, acknowledgements, peer review information; details of author contributions and competing interests; and statements of data and code availability are available at https://doi.org/10.1038/s41593-023-01267-x.

References

1. Gallego, J. A., Perich, M. G., Chowdhury, R. H., Solla, S. A. & Miller, L. E. Long-term stability of cortical population dynamics underlying consistent behavior. *Nat. Neurosci.* **23**, 260–270 (2020).
2. Steinmetz, N. A. et al. Neuropixels 2.0: a miniaturized high-density probe for stable, long-term brain recordings. *Science* **372**, eabf4588 (2021).
3. Schoonover, C. E., Ohashi, S. N., Axel, R. & Fink, A. J. P. Representational drift in primary olfactory cortex. *Nature* **594**, 541–546 (2021).
4. Dhawale, A. K. et al. Automated long-term recording and analysis of neural activity in behaving animals. *eLife* **6**, e27702 (2017).
5. Dhawale, A. K., Wolff, S. B. E., Ko, R. & Ölveczky, B. P. The basal ganglia control the detailed kinematics of learned motor skills. *Nat. Neurosci.* **24**, 1256–1269 (2021).
6. Wang, M. et al. Neuronal basis of age-related working memory decline. *Nature* **476**, 210–213 (2011).
7. Igarashi, K. M., Lu, L., Colgin, L. L., Moser, M.-B. & Moser, E. I. Coordination of entorhinal–hippocampal ensemble activity during associative learning. *Nature* **510**, 143–147 (2014).
8. Grady, C. The cognitive neuroscience of ageing. *Nat. Rev. Neurosci.* **13**, 491–505 (2012).
9. Meng, G. et al. High-throughput synapse-resolving two-photon fluorescence microendoscopy for deep-brain volumetric imaging in vivo. *eLife* **8**, e40805 (2019).
10. Salatino, J. W., Ludwig, K. A., Kozai, T. D. Y. & Purcell, E. K. Glial responses to implanted electrodes in the brain. *Nat. Biomed. Eng.* **1**, 862–877 (2017).
11. Ji, N. The practical and fundamental limits of optical imaging in mammalian brains. *Neuron* **83**, 1242–1245 (2014).
12. Yu, K. J. et al. Bioresorbable silicon electronics for transient spatiotemporal mapping of electrical activity from the cerebral cortex. *Nat. Mater.* **15**, 782–791 (2016).
13. Chiang, C.-H. et al. Development of a neural interface for high-definition, long-term recording in rodents and nonhuman primates. *Sci. Transl. Med.* **12**, eaay4682 (2020).
14. Liu, Y. et al. Soft and elastic hydrogel-based microelectronics for localized low-voltage neuromodulation. *Nat. Biomed. Eng.* **3**, 58–68 (2019).
15. Yin, R. et al. Soft transparent graphene contact lens electrodes for conformal full-cornea recording of electroretinogram. *Nat. Commun.* **9**, 2334 (2018).
16. Song, E. et al. Flexible electronic/optoelectronic microsystems with scalable designs for chronic biointegration. *Proc. Natl Acad. Sci. USA* **116**, 15398–15406 (2019).
17. Liu, J. et al. Syringe-injectable electronics. *Nat. Nanotechnol.* **10**, 629–636 (2015).
18. Yang, X. et al. Bioinspired neuron-like electronics. *Nat. Mater.* **18**, 510–517 (2019).
19. Fu, T.-M. et al. Stable long-term chronic brain mapping at the single-neuron level. *Nat. Methods* **13**, 875–882 (2016).
20. Guan, S. et al. Elastocapillary self-assembled neurotassels for stable neural activity recordings. *Sci. Adv.* **5**, eaav2842 (2019).
21. Kim, T.-i et al. Injectable, cellular-scale optoelectronics with applications for wireless optogenetics. *Science* **340**, 211–216 (2013).
22. He, F. et al. Multimodal mapping of neural activity and cerebral blood flow reveals long-lasting neurovascular dissociations after small-scale strokes. *Sci. Adv.* **6**, eaba1933 (2020).
23. Sharp, A. A., Ortega, A. M., Restrepo, D., Curran-Everett, D. & Gall, K. In vivo penetration mechanics and mechanical properties of mouse brain tissue at micrometer scales. *IEEE Trans. Biomed. Eng.* **56**, 45–53 (2008).
24. McInnes, L., Healy, J. & Melville, J. UMAP: uniform manifold approximation and projection for dimension reduction. Preprint available at *arXiv* https://doi.org/10.48550/arXiv.1802.03426 (2018).
25. Tolias, A. S. et al. Recording chronically from the same neurons in awake, behaving primates. *J. Neurophysiol.* **98**, 3780–3790 (2007).
26. Chung, J. E. et al. A fully automated approach to spike sorting. *Neuron* **95**, 1381–1394 (2017).
27. McMahon, D. B. T., Jones, A. P., Bondar, I. V. & Leopold, D. A. Face-selective neurons maintain consistent visual responses across months. *Proc. Natl Acad. Sci. USA* **111**, 8251–8256 (2014).
28. Schmitzer-Torbert, N., Jackson, J., Henze, D., Harris, K. & Redish, A. D. Quantitative measures of cluster quality for use in extracellular recordings. *Neuroscience* **131**, 1–11 (2005).
29. Nguyen, T. et al. Automatic spike sorting by unsupervised clustering with diffusion maps and silhouettes. *Neurocomputing* **153**, 199–210 (2015).
30. Kozai, T. D. Y. et al. Ultrasmall implantable composite microelectrodes with bioactive surfaces for chronic neural interfaces. *Nat. Mater.* **11**, 1065–1073 (2012).
31. Lu, L. et al. Soft and MRI compatible neural electrodes from carbon nanotube fibers. *Nano. Lett.* **19**, 1577–1586 (2019).
32. Rousche, P. J. et al. Flexible polyimide-based intracortical electrode arrays with bioactive capability. *IEEE Trans. Biomed. Eng.* **48**, 361–371 (2001).
33. Minev, I. R. et al. Electronic dura mater for long-term multimodal neural interfaces. *Science* **347**, 159–163 (2015).
34. Jeong, J.-W. et al. Wireless optofluidic systems for programmable in vivo pharmacology and optogenetics. *Cell* **162**, 662–674 (2015).
35. Airaghi Leccardi, M. J. I., Vagni, P. & Ghezzi, D. Multilayer 3D electrodes for neural implants. *J. Neural Eng.* **16**, 026013 (2019).
36. Barrese, J. C. et al. Failure mode analysis of silicon-based intracortical microelectrode arrays in non-human primates. *J. Neural Eng.* **10**, 066014 (2013).

37. Viswanathan, P. & Nieder, A. Visual receptive field heterogeneity and functional connectivity of adjacent neurons in primate frontoparietal association cortices. *J. Neurosci.* **37**, 8919–8928 (2017).

38. Jia, X. et al. High-density extracellular probes reveal dendritic backpropagation and facilitate neuron classification. *J. Neurophysiol.* **121**, 1831–1847 (2019).

39. Marks, T. D. & Goard, M. J. Stimulus-dependent representational drift in primary visual cortex. *Nat. Commun.* **12**, 5169 (2021).

40. Lee, E. K. et al. Non-linear dimensionality reduction on extracellular waveforms reveals cell type diversity in premotor cortex. *eLife* **10**, e67490 (2021).

41. Zhao, S. et al. Full activation pattern mapping by simultaneous deep brain stimulation and fMRI with graphene fiber electrodes. *Nat. Commun.* **11**, 1788 (2020).

42. Hill, D. N., Mehta, S. B. & Kleinfeld, D. Quality metrics to accompany spike sorting of extracellular signals. *J. Neurosci.* **31**, 8699–8705 (2011).

43. Siegle, J. H. et al. Survey of spiking in the mouse visual system reveals functional hierarchy. *Nature* **592**, 86–92 (2021).

44. Cao, J. et al. The single-cell transcriptional landscape of mammalian organogenesis. *Nature* **566**, 496–502 (2019).

45. Grieves, R. M. et al. The place-cell representation of volumetric space in rats. *Nat. Commun.* **11**, 789 (2020).

Methods

Animals and ethical compliance

Mature adult male C57BL/6 mice, 16 weeks of age (Charles River Laboratories), were used throughout this study. The mice were maintained at 22 ± 1 °C with humidity ranging from 30% to 70% and on a 12-hour light/dark cycle and fed ad libitum. All procedures complied with the National Institutes of Health guidelines for the care and use of laboratory animals and were approved by the Harvard University Institutional Animal Care and Use Committee under protocols 19-03-348 and 20-05-368.

Fabrication of monolithically integrated mesh electronics

(1) Cleaning a silicon wafer grown with thermal oxide (500-nm thickness) with acetone, isopropyl alcohol and deionized water. (2) Depositing 100-nm-thick Ni using a Sharon thermal evaporator as a sacrificial layer. (3) Spin-coating SU-8 precursor (SU-8 2000.5, MicroChem) at 3,000 r.p.m., which was pre-baked at (65 °C, 95 °C) for 2 minutes each, exposed to 365-nm ultraviolet (UV) for 200 mJ/cm², post-baked at (65 °C, 95 °C) for 2 minutes each, developed using SU-8 developer (MicroChem) for 60 seconds and hard-baked at 180 °C for 40 minutes to define mesh SU-8 patterns for bottom encapsulation. (4) Spin-coating LOR3A photoresist (MicroChem) at 4,000 r.p.m., followed by pre-baking at 180 °C for 5 minutes, and spin-coating S1805 photoresist (MicroChem) at 4,000 r.p.m., followed by pre-baking at 115 °C for 1 minute. The sample was then exposed to 405-nm UV for 40 mJ/cm² and developed using CD-26 developer (MICROPOSIT) for 70 seconds to define interconnects patterns. (5) Depositing 5/70/5-nm-thick chromium/gold/chromium (Cr/Au/Cr) by a Denton electron beam evaporator, followed by a standard lift-off procedure in remover PG (MicroChem) to define the Au interconnects. (6) Repeating step (4) to define electrode array patterns in LOR3A/S1805 bilayer photoresists. (7) Depositing 5/50-nm-thick chromium/platinum (Cr/Pt) by a Denton electron beam evaporator, followed by a standard lift-off procedure in remover PG (MicroChem) to define the electrode array. (8) Repeating step (3) for top SU-8 encapsulation. (9) Spin-coating SU-8 precursor (SU-8 2025, MicroChem) at 4,000 r.p.m., which was pre-baked at 65 °C for 2 minutes and 95 °C for 8 minutes, exposed to 365-nm UV for 200 mJ/cm², post-baked at 65 °C for 2 minutes and 95 °C for 6 minutes, developed using SU-8 developer (MicroChem) for 6 minutes and hard-baked at 180 °C for 1 hour to define SU-8 anchor patterns to connect the mesh and SU-8 shuttle. (10) Spin-coating 20 wt% dextran solution at 1,000 r.p.m. for 20 seconds, which was at 80 °C for 1 minute and 180 °C for 30 minutes. (11) Spin-coating SU-8 precursor (SU-8 2025, MicroChem) at 3,000 r.p.m., which was pre-baked at 65 °C for 2 minutes and 95 °C for 8 minutes, exposed to 365-nm UV for 200 mJ/cm², post-baked at 65 °C for 2 minutes and 95 °C for 6 minutes, developed using SU-8 developer (MicroChem) for 6 minutes and hard-baked at 180 °C for 1 hour to define the SU-8 shuttle pattern. (12) Cleaning the I/O with water and soldering a 32-channel flexible flat cable (Molex) onto the I/O pads using a flip-chip bonder (Finetech FINEPLACER). (13) Soaking the mesh electronics in nickel etchant for 2–4 hours to completely release the mesh electronics from the substrate wafer. (14) Rinsing the mesh electronics with deionized water and PBS three times each. (15) Dicing the substrate to the desired length. Dip-coating 10 wt% PEG solution to attach the mesh electronics and SU-8 polymer shuttle. The monolithically integrated mesh electronics were allowed to dry in the air. (16) After cutting the anchor, the monolithically integrated mesh electronics were ready for implantation.

In vitro testing

The yield of insertion and extraction was determined by in vitro testing in agarose gels. Success was defined as the successful delivery of the mesh electronics to the target depth upon insertion and the preservation of the integrity and location of the mesh electronics after the shuttle extraction. The implantation was performed by three researchers, and each of them implanted five mesh electronics. The total yield was calculated as the average of the success rates achieved by the three researchers.

Brain implantation

During the intracranial implantation surgery, the mice were anesthetized with 2–3% isoflurane and maintained under anesthesia with 0.75–1% isoflurane. Stainless steel screws were implanted in the cerebellum as ground electrodes. A craniotomy (2 × 2 mm²) was performed to expose the cortical surface after removing the dura mater. The mesh electronics with the releasable shuttle was attached to a micromanipulator on a stereotaxic frame. The micromanipulator was used to manually insert the electronics into the brain at the targeted depth. Sterile saline solution was applied on the rear end of the electronics to dissolve the PEG/dextran and release the SU-8 shuttle from the mesh electronics. After the PEG/dextran had fully dissolved on both ends, the SU-8 shuttle was extracted using a second manipulator, leaving the ultra-flexible mesh electronics implanted at the target positions. The craniotomy was sealed with a silicone elastomer (World Precision Instruments), and ceramic bone anchor screws and dental methacrylate were used to fix the flat flex connector (FFC) and electrode set onto the mouse skull.

Immunohistochemistry

The following procedures were carried out as previously described[17,46]. To prepare histology samples, mice were anesthetized with 40–50 mg kg⁻¹ of sodium pentobarbital and perfused transcardially with approximately 40 ml of PBS, followed by 40 ml of 4% paraformaldehyde (PFA) in PBS. After decapitation, the scalp skin was removed, and the exposed skull/dental cement was ground for 10–20 minutes at 15,000 r.p.m. using a high-speed micromotor tool. The brain with undisturbed mesh or thin-film electronics was removed from the cranium, post-fixed in PFA for 24 hours at 4 °C and then transferred to a series of sucrose solutions with increasing concentrations (10–30% (w/v)) until it sank to the bottom for the thin tissue preparation. This was done at different timepoints after implantation (2 weeks, 6 weeks, 12 weeks and 1 year).

Immunohistochemical staining of 20-μm thin tissue was performed as follows. After cryostat sectioning, brain slices were incubated in PBST (1× PBS with 0.2% Triton X-100, Thermo Fisher Scientific) for 30 minutes and then blocked with 5% (w/v) normal donkey serum for 2 hours. After three 30-minute rinses with PBST, the slices were incubated at 4 °C overnight with primary antibodies for astrocytes (chicken anti-glial fibrillary protein GFAP, 1:200, Abcam, ab4674), microglia (goat anti-ionized calcium binding adaptor molecule 1 Iba1, 1:100, Abcam, ab5076) and neurons (rabbit anti-neuronal nuclear NeuN, 1:200, Abcam, ab177487). The slices were then washed three times for 30 minutes each with PBST and incubated for 2 hours at room temperature in the dark with secondary antibody (1:500, Alexa Fluor 647 donkey anti-chicken, Jackson ImmunoResearch; 1:500, Alexa Fluor 594 donkey anti-goat; 1:500, Alexa Fluor 488 donkey anti-rabbit, Invitrogen). After additional washes with PBST three times for 30 minutes each with PBST, the brain slices were stained with DAPI (Sigma-Aldrich) for 30 minutes to mark all cell nuclei. The slices were then washed and mounted on glass slides with coverslips using ProLong Gold (Invitrogen) mounting media. The slides were kept in the dark at room temperature for 12 hours of clearance before imaging.

Thick tissue clearing and staining was performed as follows. After vibratome sectioning, brain slices were placed in 1× PBS containing 4% (w/v) acrylamide (Sigma-Aldrich) and 0.25% (w/v) VA-044 thermal polymerization initiator (Thermo Fisher Scientific) at 4 °C for 3 days. The solution was replaced with a fresh solution before placing the brain slices in the X-CLARITY polymerization system (Logos Biosystems) for 3 hours at 37 °C. After polymerization, any remaining gel on the tissue surface was removed, and the slices were rinsed with PBST before being placed in electrophoretic tissue clearing solution (Logos Biosystems)

at 37 °C for 3–5 days until the samples were translucent. The brain slices were incubated with PBST overnight, washed three times with PBST and then blocked with 5% (w/v) normal donkey serum for 2 days. After three rinses with PBST, the slices were incubated at 4 °C for 5–7 days with primary antibodies, washed three times with PBST and incubated at 4 °C for 5–7 days in the dark with secondary antibodies. The slices were then washed three times with PBST and incubated with DAPI for 2 days to mark all cell nuclei. The brain slices were then glued at their edge to the bottom of Petri dishes with 1% (w/v) agarose in optical clearing solution (LifeCanvas Technologies) for 24 hours before microscopy imaging.

Microscope imaging acquisition and analysis

Confocal fluorescent images were obtained using a Leica SP8 confocal system. Images were collected using a ×25, 0.95 NA water-immersion or ×40, 1.3 NA oil-immersion objective lens and lasers with wavelengths of 488 nm, 591 nm and 633 nm as excitation sources for Alexa Fluor 488, Alexa Fluor 594 and Alexa Fluor 647, respectively. Standard TIFF files were exported and colorized using LAS X Software. ImageJ software and custom code were used for image analysis. The distance of each pixel to the mesh or film electronics was defined as the shortest distance from the mesh/film boundary. The baseline fluorescence intensity was defined as the average fluorescence intensity of all pixels 525–550 μm away from the boundary. Intensity values were binned over intervals of 25 μm, averaged and normalized against the baseline intensity.

Electrophysiological data acquisition and spike sorting

Neural activity of mice was recorded monthly using the CerePlex Direct recording system (Blackrock Microsystems) starting from 1 month after implantation (5-month-old mice). A homemade printed circuit board (PCB) was used to connect the FFC and headstage. Electrophysiological recordings were performed at a sampling rate of 10 kHz. Mesh electronics with sparsely distributed electrodes were used to record from 5 to 17–18 months of mouse age (mice 1–6), and mesh electronics with tetrode-like electrode arrays were used to record from 5 to 11 months of mouse age (mice 7–11). Long-term recordings in mice 1 and 2 were performed under 0.75% isoflurane anesthesia, whereas long-term recordings in mice 3–11 were performed while the mice were awake and head fixed.

The following standard procedure was used to pre-process each recording session[2,3,40,47]. A digital bandpass filter (300–3,000 Hz) was applied; common average reference was used to reduce the common-mode noise by creating an average of all electrode channels and subtracting it from each channel; and all recordings across multiple months were concatenated and used for downstream spike sorting. For mesh electronics with tetrode-like electrode arrays, the concatenated recordings were then spike sorted using the fully automated algorithm MountainSort[26] with the SpikeInterface package (version 0.93.0)[47]. MountainSort takes into account the geometry or the electrode array, so when a neuron is recorded by multiple neighboring electrodes from the same array, it will consider the similar spikes firing simultaneously from these multiple electrodes as coming from the same neuron. For mesh electronics with sparsely distributed electrode arrays, spike detection was performed using the WaveClus3 software package. Clusters were determined using Leiden[48], and clustering was performed on a graph constructed by UMAP[24]. The large distance between neighboring electrodes ensured that no neuron was recorded by two separate electrodes.

The output of spike sorting was manually curated without the knowledge of visual stimulus responsiveness or downstream stability verification. The standard procedure described in Phy (https://github.com/cortex-lab/phy) was followed. During manual curation, units were selected for downstream analyses based on the following criteria[2]: (1) the spatial extent of the waveform is sufficiently small, which distinguishes neuronal waveforms from noise; (2) the fraction of refractory period violations is <10%, and ISI distribution conforms to a Poisson

distribution, which distinguishes well-isolated single units from the background activities, and units with firing rate less than 0.1 Hz were excluded. In addition, a pair of units was merged based on the following criteria: (1) similar auto-correlogram showing a visible refractory period; (2) cross-correlogram with a strong, asymmetric peak at a short time interval; and (3) overlapping PCA embeddings.

Visual stimulation

Mice were shown two sets of stimuli—static gratings and dynamic gratings—during each recording session. The stimuli were displayed monocularly on an ASUS PA248Q LCD monitor with 1,920 × 1,200 pixels, positioned 15 cm from the eye and covering 120° × 95° of visual space. Static gratings were shown at six different orientations (0°, 30°, 60°, 90°, 120° and 150°) and three spatial frequencies (0.04, 0.08 and 0.16 cycles per degree) with 15 repeats per recording session. Dynamic gratings had a spatial frequency of 0.04 cycles per degree, 12 directions (0°, 30°, 60°, 90°, 120°, 150°, 180°, 210°, 240°, 270°, 300° and 330°), a 2-Hz temporal frequency and 15 repeats per recording session.

Assessment of single-unit recording

Cluster quality was evaluated using two metrics: L-ratio and silhouette score. The L-ratio is a measure of the separability of clusters, with low values (<0.05) indicating good separability and high values indicating potential incorrect inclusion of spikes from other clusters. The silhouette score is measure of how well defined a cluster is and is calculated using the implementation of scikit-learn version 0.24.2 (http://scikit-learn.org). For mesh electronics with sparsely distributed electrodes, the L-ratio and silhouette score were calculated on an individual electrode. For mesh electronics with tetrode-like electrode arrays, the L-ratio and silhouette score were calculated on all electrodes within an array. The ISI distribution was calculated for individual months with a bin size of 2 ms and a range of 0–100 ms. The refractory period violation of each unit was calculated by its fraction of spikes that had low ISI (<1.5 ms).

Assessment of single-unit stability over time

Assessment of recording stability by waveform similarity. The stability of the recordings was assessed by comparing the waveform similarity of the neurons during two separate recording sessions based on previous study[3]. A neuron was considered to be the same across sessions when the waveform similarities within that neuron were higher than those between different neurons. For mesh electronics with tetrode-like electrode arrays, we calculated average waveforms for each neuron and then concatenated these average waveforms from all the electrodes in each array and finally used Pearson correlation to measure the waveform similarity between a pair of concatenated average waveform vectors. For mesh electronics with sparsely distributed electrodes, waveform similarity was calculated using the recordings from individual electrodes between two recording sessions.

Assessment of recording stability by waveform features. PT ratio, duration, repolarization slope, amplitude and recovery slope, firing rate, L-ratio, silhouette score and SNR were computed to validate recording stability using SpikeInterface package[47] and AllenSDK (https://github.com/AllenInstitute/AllenSDK).

Assessment of recording stability by estimated position of neurons. The estimated positions of each neuron were evaluated using the SpikeInterface package. To estimate the position of a single neuron, a spatial average was calculated using electrode positions weighted by the mean waveform amplitude at each electrode, with

$$(x, y) = \left(\frac{\sum_{i=1}^{N} x_i a_i}{\sum_{i=1}^{N} a_i}, \frac{\sum_{i=1}^{N} y_i a_i}{\sum_{i=1}^{N} a_i} \right) \qquad (1)$$

where N is the number of electrodes; x_i and y_i are the horizontal and vertical positions of the ith electrode, respectively; and a_i is the peak-to-peak amplitude of the spike waveform recorded at the ith

electrode. The displacement of a single neuron was then calculated using the Euclidean distance between the estimated positions of the neuron in each recording session. It is worth noting that, due to complicated morphologies and biophysics of the neurons in visual cortex, the estimated position of a neuron may not be the exact physical location of the neuron relative to the probe sites. However, if the recording was stable, the displacement of the estimated position should be small over months. Specifically, neurons whose estimated positions showed a displacement of less than 10 μm across two recording sessions were considered stable. To validate the stability defined by the estimated positions of the neurons, cumulative distributions of the within-neuron and across-neuron centroid displacement across two recording sessions were calculated.

Assessment of recording stability by visual stimulus-dependent activities. The stability of the visual stimulus-dependent single-neuron activities was evaluated based on previous studies[2,27]. First, neurons were identified based on their selective firing patterns in response to different visual stimuli (12 dynamic gratings or 18 static gratings, with $P < 0.01$ in a Kruskal–Wallis test of the visual responses). Neurons that met these criteria in the first month of recording were included in the chronic stability analysis. Second, the stability of the visual response was gauged using the following procedure based on previous studies[2]. Specifically, the firing patterns of each neuron in response to all visual stimuli were calculated by averaging the firing rate across all trials for each visual stimulus. The visual firing pattern of each neuron in the first month was compared to its own visual firing patterns in all other months as well as to the visual firing patterns of other neurons from different months. This comparison resulted in two possible outcomes for each neuron: (1) a match, when the similarities of the visual firing patterns within the same neurons were higher than those between different neurons; and (2) a mismatch, when the visual firing pattern of one neuron on the first recording session had a higher similarity to that of another neuron in close proximity to the original neuron on the second recording session[2]. Neurons that were identified matches were considered stable neurons across months. Third, the month-to-month consistency of the visual responses was also assessed using the procedure based on previous studies[27]. Specifically, stimulation-dependent recording trials were divided into two subsets (odd versus even trials), and a split-half correlation coefficient was calculated between the subsets of the odd and even trials on each recording session. The consistency of visual response within a day (r_{within}) for each neuron was calculated as the Pearson correlation between the averaged visual firing patterns from odd trials and those from even trials. The consistency of visual response across months (r_{across}) for the same neurons were calculated by the Pearson correlation between the firing patterns on reference recording sessions (the last month of recording in our analysis) and those on previous recording sessions. To compare r_{within}, r_{across} and a random level of response, the order of images in the visual firing patterns was randomly shuffled, and the $r_{shuffle}$ of each neuron was calculated as the Pearson correlation between the averaged randomized visual firing patterns from odd and even trails. To further assess whether the tetrode-like mesh electrode arrays tracked the same neurons over time, we also quantified the visual response consistency across different neurons using a split-half analysis on each month. The r from the same neurons was defined as the Pearson correlation between the averaged visual firing patterns from odd trials and those from even trials. The r from different neurons was defined as the Pearson correlation between the averaged visual firing patterns of one neuron and another neuron. To quantify the separability of r from the same cells and r from different cells, a ROC analysis was conducted, and the AUC was calculated. Each point on the ROC curve represents the false alarms and hits under one discrimination threshold. When varying the discrimination threshold from the minimum r values to the maximum r values, numerous points consist of the ROC curve.

Statistics and reproducibility

The acute damage characterization was repeated on five independent animals for each implantation method for a total of 20 mice. The histology experiments to investigate the time-dependent electronics–tissue interfaces were repeated on five independent animals at each of the four timepoints, for a total of 20 mice. Three independent animals were used to explore the potential implantation capability. The long-term electrophysiological experiment was repeated on 11 independent animals. The number of replicates (n) is also indicated in the figure legends and refers to the number of experimental subjects treated independently in each experimental condition. In total, experiments and analyses were conducted on 54 mice. Attempts at replication were successful, and the conclusions were drawn from the analysis of multiple experiments. Animals with surgical complications or that displayed health concerns during the post-surgery monitoring period were excluded. No statistical methods were used to pre-determine sample sizes, but they are similar to those reported in previous publications[18,19]. Data are presented as mean/median ± standard error/standard deviation, as noted in the figure legends. The data distribution was assumed to be normal, but this was not formally tested. Statistical comparisons were performed using Origin 2020, Python 3.7 and Scipy 1.7.3 with appropriate inferential methods, as indicated in the figure legends. Graphs were created using Origin 2020, Python 3.7, matplotlib 3.5.1 and seaborn 0.11.2. One-way ANOVA followed by Tukey correction was used for multiple comparisons unless specifically noted. Two-sided t-tests were used for two-group comparisons. Statistical results in the figures are presented as symbols *$P < 0.05$, **$P < 0.01$, ***$P < 0.001$ or exact P value. The investigators were blinded to data collection and analyses of fluorescence images. Mice were randomized into different experimental groups. For the visual stimulation, mice received visual stimuli in a random order. Blinding was not relevant to the long-term electrophysiological recording because the animals were not divided into control and experimental groups.

Reporting summary

Further information on research design is available in the Nature Portfolio Reporting Summary linked to this article.

Data availability

The data analyzed during the current study are available at https://github.com/LiuLab-Bioelectronics-Harvard/SpikeStability. Raw data generated during the current study are available from the corresponding author upon reasonable request. Source data are provided with this paper.

Code availability

Blackrock Research Central Software Suite 7.04 was used to acquire electrophysiology data, available at https://blackrockneurotech.com/research/support/software/. Leica Application Suite X software platform 3.5.5 was used to acquire fluorescence images. Psychtoolbox-3 was used for visual stimulation administration, available at http://psychtoolbox.org. All data analysis and visualization in this study are implemented based on Python 3.7, MATLAB 2021a, Origin 2020 and ImageJ 1.53k. The following packages and software were used: R 4.1.0, RStudio 1.4, Jupyter 1.0.0, Anaconda 4.10.3, WaveClus3 (https://github.com/csn-le/wave_clus), Leiden 0.8.2 (https://github.com/vtraag/leidenalg), UMAP 0.5.2 (https://github.com/lmcinnes/umap), AllenSDK 2.10.1 (https://github.com/AllenInstitute/AllenSDK), tensorflow 2.5 (https://www.tensorflow.org), Monocle3 (https://cole-trapnell-lab.github.io/monocle3), MountainSort 4 (https://github.com/flatiron-institute/mountainsort), SpikeInterface 0.93.0 (https://github.com/SpikeInterface), scikit-learn 0.24.2, matplotlib 3.5.1, seaborn 0.11.2, numpy 1.21.5, scipy 1.7.3, pandas 1.3.5, cmasher 1.6.3, isosplit5 0.1.3 and pickle5 0.0.12. Custom code used in this study has been deposited on GitHub (https://github.com/LiuLab-Bioelectronics-Harvard/SpikeStability) and Zenodo (https://doi.org/10.5281/zenodo.7504820).

References

46. Zhao, S. et al. Graphene encapsulated copper microwires as highly MRI compatible neural electrodes. *Nano Lett.* **16**, 7731–7738 (2016).
47. Buccino, A. P. et al. SpikeInterface, a unified framework for spike sorting. *eLife* **9**, e61834 (2020).
48. Traag, V. A., Waltman, L. & van Eck, N. J. From Louvain to Leiden: guaranteeing well-connected communities. *Sci. Rep.* **9**, 5233 (2019).

Acknowledgements

Author contributions

J. Liu and S.Z. conceived and designed the experiments. S.Z., R.L. and J. Lee fabricated and characterized the electrodes. S.Z. and Z.L. performed the brain implantation and in vivo recording and histology study. S.Z. and W.T. conducted visual stimulation experiments. S.Z., W.T., X.T., S.P. and S.G. conducted the data analysis. J. Liu, S.Z., X.T., W.T., S.P. and H.S. wrote the manuscript.

Competing interests

Additional information

Extended data is available for this paper at https://doi.org/10.1038/s41593-023-01267-x.

Supplementary information The online version contains supplementary material available at https://doi.org/10.1038/s41593-023-01267-x.

Correspondence and requests for materials should be addressed to Jia Liu.

Peer review information *Nature Neuroscience* thanks Michael Okun and the other, anonymous, reviewer(s) for their contribution to the peer review of this work.

Reprints and permissions information is available at www.nature.com/reprints.

Zhao, Siyuan <siyuanzhao@g.harvard.edu>

Final Decision made for NNANO-22051051C

1 message

---

lu.shi@nature.com <lu.shi@nature.com>   Mon, Oct 16, 2023 at 1:39 AM
Reply-To: lu.shi@nature.com
To: siyuanzhao@g.harvard.edu

Dear Dr Zhao,

Please find below a copy of the decision letter for your manuscript "3D spatiotemporally scalable in vivo neural probes based on fluorinated elastomers" [NNANO-22051051C], which has just been accepted for publication in Nature Nanotechnology.

You can now use a single sign-on for all your accounts, view the status of all your manuscript submissions and reviews, access usage statistics for your published articles and download a record of your refereeing activity for the Nature journals.

To assist our authors in disseminating their research to the broader community, our SharedIt initiative provides all co-authors with the ability to generate a unique shareable link that will allow anyone (with or without a subscription) to read the published article. Recipients of the link with a subscription will also be able to download and print the PDF.

As soon as your article is published, you can generate your shareable link by entering the DOI of your article here: http://authors.springernature.com/share. Corresponding authors will also receive an automated email with the shareable link.

Sincerely,

Dr. Lu Shi
Senior Editor
Nature Nanotechnology

Subject: Decision on Nature Nanotechnology manuscript NNANO-22051051C

16th October 2023

Dear Jia,

We are pleased to inform you that your manuscript, "3D spatiotemporally scalable in vivo neural probes based on fluorinated elastomers", has been accepted for publication in Nature Nanotechnology, subject to checking and approval of your production-quality files. If there are any technical issues with your files, our Art Editor will contact you promptly.

The received date for your paper will be 3rd May 2022, and the accepted date will be 16th October 2023. The publication date is normally 4-5 weeks after receipt of the production-quality files.

Once your manuscript is typeset and you have completed the appropriate grant of rights, you will receive a link to your electronic proof via email with a request to make any corrections within 48 hours. If, when you receive your proof, you cannot meet this deadline, please inform us at rjsproduction@springernature.com immediately. Once your paper has been scheduled for online publication, someone from our Press or Editorial Assistant team will be in touch to confirm the details.

Acceptance of your manuscript is conditional on all authors' agreement with our publication policies (see www.nature.com/nnano/authors/index.html). In particular your manuscript must not be published elsewhere and there must be no announcement of the work to any media outlet until the publication date (the day on which it is uploaded onto our web site).

Please note that *Nature Nanotechnology* is a Transformative Journal (TJ). Authors may publish their research with us through the traditional subscription access route or make their paper immediately open access through payment of an article-processing charge (APC). Authors will not be required to make a final decision about access to their article until it has been accepted. Find out more about Transformative Journals

Authors may need to take specific actions to achieve compliance with funder and institutional open access mandates. If your research is supported by a funder that requires immediate open access (e.g. according to Plan S principles) then you should select the gold OA route, and we will direct you to the compliant route where possible. For authors selecting the subscription publication route, the journal's standard licensing terms will need to be accepted, including self-archiving policies. Those licensing terms will supersede any other terms that the author or any third party may assert apply to any version of the manuscript.

If you have posted a preprint on any preprint server, please ensure that the preprint details are updated with a publication reference, including the DOI and a URL to the published version of the article on the journal website.

An online order form for reprints of your paper is available at https://www.nature.com/reprints/author-reprints.html. All co-authors, authors' institutions and authors' funding agencies can order reprints using the form appropriate to their geographical region.

We welcome the submission of potential cover material (including a short caption of around 40 words) related to your manuscript; suggestions should be sent to Nature Nanotechnology in London, either as hard copies or as electronic files (the image should be 300 dpi at 210 x 297 mm in either TIFF or JPEG format).
* Please note that such pictures should be selected more for their aesthetic appeal than for their scientific content, and that colour images work better than black and white or grayscale images.
* Please do not try to design a cover with the Nature Nanotechnology logo etc, and please do not submit composites of images related to your work. I am sure you will understand that we cannot make any promise as to whether any of your suggestions might be selected for the cover of the journal.

You can now use a single sign-on for all your accounts, view the status of all your manuscript submissions and reviews, access usage statistics for your published articles and download a record of your refereeing activity for the Nature journals.

To assist our authors in disseminating their research to the broader community, our SharedIt initiative provides you with a unique shareable link that will allow anyone (with or without a subscription) to read the published article. Recipients of the link with a subscription will also be able to download and print the PDF.

As soon as your article is published, you will receive an automated email with your shareable link.

In approximately 10 business days you will receive an email with a link to choose the appropriate publishing options for your paper and our Author Services team will be in touch regarding any additional information that may be required.

If you have any questions about our publishing options, costs, Open Access requirements, or our legal forms, please contact ASJournals@springernature.com

Congratulations again and wish you all the best in your research!

With kind regards,

Lu

Dr. Lu Shi
Senior Editor
Nature Nanotechnology

P.S. Click on the following link if you would like to recommend Nature Nanotechnology to your librarian
http://www.nature.com/subscriptions/recommend.html#forms

** Visit the Springer Nature Editorial and Publishing website at www.springernature.com/editorial-and-publishing-jobs for more information about our career opportunities. If you have any questions please click here.**

This email has been sent through the Springer Nature Tracking System NY-610A-NPG&MTS

Confidentiality Statement:

This e-mail is confidential and subject to copyright. Any unauthorised use or disclosure of its contents is prohibited. If you have received this email in error please notify our Manuscript Tracking System Helpdesk team at http://platformsupport.nature.com .

Details of the confidentiality and pre-publicity policy may be found here http://www.nature.com/authors/ policies/confidentiality.html

3D spatiotemporally scalable in vivo neural probes based on fluorinated elastomers

Paul Le Floch [1,2,6], Siyuan Zhao [1,6], Ren Liu[1,6], Nicola Molinari[1], Eder Medina[1], Hao Shen [1], Zheliang Wang[3], Junsoo Kim [1], Hao Sheng [1], Sebastian Partarrieu [1], Wenbo Wang [1], Chanan Sessler[4,5], Guogao Zhang [1], Hyunsu Park[2], Xian Gong [2], Andrew Spencer[2], Jongha Lee[2], Tianyang Ye[2], Xin Tang [1], Xiao Wang [4,5], Katia Bertoldi[1], Nanshu Lu [3], Boris Kozinsky [1], Zhigang Suo [1] & Jia Liu [1]✉

Electronic devices for recording neural activity in the nervous system need to be scalable across large spatial and temporal scales while also providing millisecond and single-cell spatiotemporal resolution. However, existing high-resolution neural recording devices cannot achieve simultaneous scalability on both spatial and temporal levels due to a trade-off between sensor density and mechanical flexibility. Here we introduce a three-dimensional (3D) stacking implantable electronic platform, based on perfluorinated dielectric elastomers and tissue-level soft multilayer electrodes, that enables spatiotemporally scalable single-cell neural electrophysiology in the nervous system. Our elastomers exhibit stable dielectric performance for over a year in physiological solutions and are 10,000 times softer than conventional plastic dielectrics. By leveraging these unique characteristics we develop the packaging of lithographed nanometre-thick electrode arrays in a 3D configuration with a cross-sectional density of 0.076 electrodes per square micrometre. The resulting 3D integrated multilayer soft electrode array retains tissue-level flexibility, reducing chronic immune responses in mouse neural tissues, and demonstrates the ability to reliably track electrical activity in the mouse brain or spinal cord over months without disrupting animal behaviour.

Q1 Mapping the long-term stable activity of the central nervous system is important for neuroscience[1,2], addressing neurological disorders[3–5] and developing high-bandwidth brain–machine interfaces for neuro-prosthetics and communications[6,7]. However, mapping neural activity in the central nervous system is challenging as the functions of the central nervous system not only occur across multiple regions and depths of the tissue over months and years but also involve electrical activities that need to be quantified on the millisecond and micrometre scales of individual neurons. Among current technologies, implantable microelectrode arrays can simultaneously measure extracellular action potentials of thousands of single neurons at the millisecond timescale[6,8]. The number of electrodes can be increased further through three-dimensional (3D) stacking[9] or the integration of CMOS (complementary metal–oxide–semiconductor) multiplexing circuits[8]. However, their temporal scalability for the long-term stable recording of electrical activities from the same neurons is limited by

[1]John A. Paulson School of Engineering and Applied Sciences, Harvard University, Boston, MA, USA. [2]Axoft, Inc., Cambridge, MA, USA. [3]Department of Aerospace Engineering and Engineering Mechanics, The University of Texas at Austin, Austin, TX, USA. [4]Broad Institute of MIT and Harvard, Cambridge, MA, USA. [5]Department of Chemistry, Massachusetts Institute of Technology, Cambridge, MA, USA. [6]These authors contributed equally: Paul Le Floch, Siyuan Zhao, Ren Liu. ✉e-mail: jia_liu@seas.harvard.edu
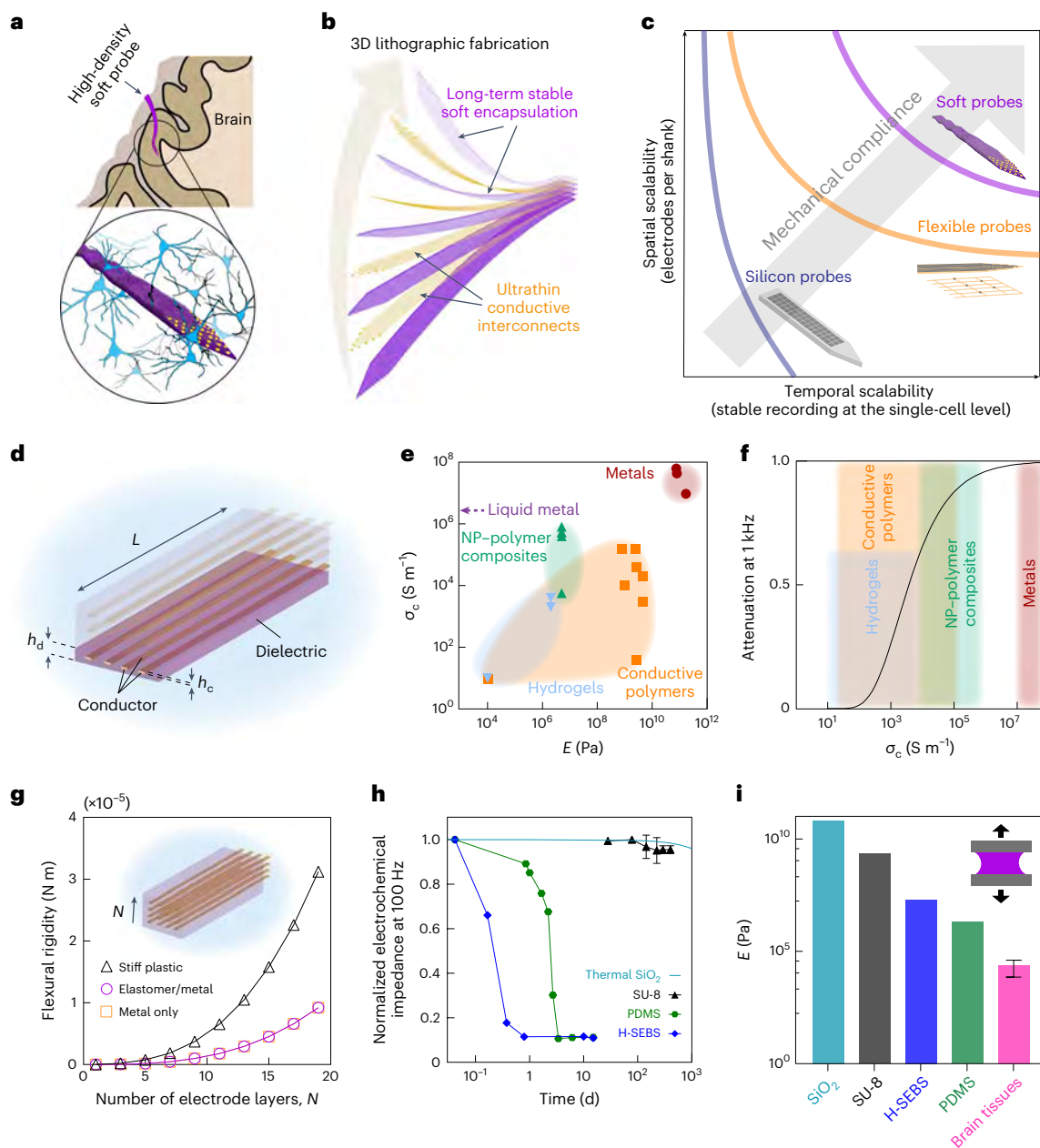
Fig. 1 | Implantable neural probes for spatiotemporally scalable in vivo electrophysiology. a, Schematic showing a spatiotemporally scalable neural probe implanted in the brain. The inset shows a 3D stacked microelectrode array encapsulated by soft elastomer layers, which can prevent ion permeation from the biofluid and maintain cell- and tissue-level mechanical properties, capable of providing a long-term stable interface with neurons at the single-cell level. **b**, Schematic illustrating the 3D lithographic fabrication of multilayer thin-film soft encapsulation/conductive interconnects to scale up the number of electrodes integrated on the neural probe. **c**, Spatial and temporal scalability of neural probes. Rigid silicon electronics can achieve high-density electrodes for neural recording but cannot stably record electrical activities from the same neurons over a long time period. Tissue-like flexible electronics can record electrical activities from the same neurons over a long time but do not offer scalability to increase the density and number of electrodes for neural recording. Soft electronics with a 3D electrode array can provide both spatial and temporal scalability for neural recording. **d**, Representative geometry of one layer of electrodes from a 3D stacked electrode array as a scalable neural probe, where L denotes the length of the interconnects, h_c denotes the thickness of

the interconnects and h_d denotes the thickness of dielectric encapsulation. **e**, Conductivity of materials (σ_c) for flexible and soft electronics as a function of their elastic modulus (E)[26–36]. NP, nanoparticle. **f**, Attenuation of the voltage along an interconnect described in **d** as a function of the electrical conductivity of the materials. Parameters for simulation: $L = 2$ cm, $h_c = 40$ nm, $h_d = 1$ μm and $\varepsilon_d = 3.2$ for the dielectric constant of the encapsulation. **g**, Flexural rigidity of the neural probe as a function of the number of layers (N) of 3D integrated interconnects. Modulus values of 79 GPa, 4 GPa and 0.5 MPa are used for the simulation of metal interconnects, and plastic and elastomer encapsulations. **h**, Normalized electrochemical impedance of representative dielectric thin films as a function of the soaking time in 1x phosphate-buffered saline (PBS) solution at 37 °C. The SU-8 (an epoxy-based photoresist), polydimethylsiloxane (PDMS) and hydrogenated styrene-ethylene-butylene-styrene (H-SEBS) films have respective average thicknesses of 0.84 μm, 8.04 μm and 3.60 μm. For SU-8, the values are shown as the mean ± s.d. ($n = 4$ samples), and the PDMS and H-SEBS data are from our previous work[37]. For thermal silica (SiO₂), the model used is based on the etching rate measured in ref. 25. **i**, Elastic modulus values of dielectric materials compared with brain tissues[64].

probe drifting, chronic tissue damage and immune responses due to the large mechanical and structural disparities between the implantable electrodes and brain tissues[10].

The recent development of flexible thin-film nanoelectronics[6,11–15] tackles this issue by introducing biomimetic designs such as mesh nanoelectronics[12,16] and ultraflexible probes[6,13]. These designs reduce the thickness of stiff electronic structures to the submicrometre range, which enables tissue-level flexible nanoelectronics that reduce immune responses and probe drifting. As a result, it is possible to track the electrical activity of the same neurons in animals over a long period of time[12]. Despite remarkable progress, this aggressive downscaling of the neural probe dimensions due to the intrinsic stiffness of materials used in flexible nanoelectronics limits the ability to scale up the number of electrodes while maintaining tissue-level flexibility[6,17,18].

Here we introduce a spatiotemporally scalable neural probe (Fig. 1a) through the 3D integration of thin-film tissue-level soft microelectrode arrays (Fig. 1b). We have overcome the intrinsic instability of soft dielectric elastomers as passivation layers in physiological solutions through the use of fluorinated elastomers with high hydrophobicity[17,19] and low molecular solubility[20,21], which substantially reduces ion diffusion from surrounding biofluids, enabling a very long-term stable dielectric performance in biofluids. Specifically, we developed an elastomer based on perfluoropolyether (PFPE) as an elastic photo-patternable dielectric material[22,23]. This PFPE-based photo-patternable dielectric material is (1) 10,000 times softer than conventional stiff plastic encapsulation while maintaining the same level of longitudinal dielectric performance, (2) capable of micrometre-resolution 3D photolithographic multilayer nanofabrication and (3) compatible with nanometre-thick metal deposition. The 3D stacked microelectrode arrays can increase the number and density of electrodes through 3D stacking while maintaining tissue-level flexibility and mechanical robustness, and are capable of stably tracking electrical activities at single-unit-single-spike resolution over months with reduced immune responses, which demonstrates their scalability in both spatial and temporal scales for neural electrophysiology (Fig. 1c).

Our design is based on the following rationales. One way to increase the electrode density without changing the probe's flexibility properties is by substantially reducing the interconnect dimensions. However, this poses challenges such as crosstalk and signal attenuation (Supplementary Discussion 1)[24]. Another approach involves using thin-film transistors for on-site multiplexing to increase the electrode density, but their mechanical rigidity and need for thick inorganic

passivation in physiological solutions[25] limit their potential for use in tissue-level flexible neural probes. A third option is to increase the electrode density by vertically stacking 3D electrode arrays (Fig. 1d)[6,13], although this requires the incorporation of low-modulus electronic materials to preserve the overall flexibility.

Although certain soft conductors[26–36] offer mechanical flexibility, their conductivity is affected to a large extent by their softness (Fig. 1e). The moderate conductivity compounded with large parasitic capacitance limits their use in high-density neural recording[37]. To offer sufficient conductivity for signal transmission and maintain cellular-level mechanical properties and feature sizes, nanoscale metals (for example, gold (Au)) are still the ideal candidates for interconnects (Fig. 1e,f, Extended Data Fig. 1 and Supplementary Discussion 2). By contrast, the dielectric constant (ε) that determines the performance of the encapsulation layer is not always affected by the mechanical softness of the insulator. Using an Euler–Bernoulli beam theory-based analytical model (Supplementary Discussion 3), we found that combining a soft dielectric elastomer as the encapsulation layer with a nanometre-thick metal layer as the conductive layer can substantially reduce the flexural rigidity of the neural probe (that is, the bending stiffness per unit width) by around 10,000 times (Fig. 1g and Extended Data Fig. 2a–e) compared with the probe using rigid plastic encapsulation. In fact, the contribution of the elastomer layers to the overall probe flexural rigidity is negligible compared with that of a frictionless stack of nanometre-thick metal layers alone. Therefore, incorporating thin-film dielectric elastomers with tissue-level elastic modulus as passivation layers could pave the way to increase further the electrode count and density in tissue-like electronics through 3D stacking (Fig. 1b,c).

Long-term stable soft encapsulation in biofluids

Conventional dielectric elastomers can be used as soft encapsulation materials for bioelectronics; however, their long-term encapsulation performance is limited by the progressive penetration of ions[37] from physiological solutions into the elastomer (Fig. 1h,i). Our previous work showed that their electrochemical impedance drops drastically in biofluids, reducing the cut-off frequency of the encapsulated electrode[37] (Extended Data Fig. 1). This instability is caused mainly by the diffusion of ions from biofluids into the elastomers (Fig. 2a) as soft polymers have molecular permeabilities that are typically orders of magnitude higher than those of plastics and inorganics[38–40]. The ionic conductivity of polymers is directly proportional to their diffusivity and solubility (equation (1)),

Fig. 2 | Fluorinated elastomers as soft and long-lived dielectrics. **a**, Schematics showing the effect of ion diffusion and solvent swelling on a plastic, a conventional elastomer and a fluorinated elastomer. **b**, Diffusion coefficient of water (top) and sodium and chloride ions (bottom) as a function of $1,000/T$ estimated via MD simulations for PDMS, H-SEBS, perfluoropolyether dimethacrylate (PFPE-DMA) and poly(1,1,1,3,3,3-hexafluoroisopropyl acrylate) (PHFIPA), where the values are shown as the mean ± s.d. for $n = 5$ simulations per material and per diffusing species. **c**, Schematics illustrating the electrochemical methods used to evaluate the built-up ionic conductivity of dielectric polymers after immersion in physiological solution (middle). Left: three-electrode setup used to measure the EIS spectrum, which determines the impedance of the dielectric polymer. The working electrode is in contact with one side of the dielectric thin film, while the other side is immersed in PBS with the Pt counter electrode and the reference Ag/AgCl electrode. The electrochemical impedance across the dielectric thin film is measured over the time course of immersion in PBS. Right: EEC measurement, in which the dielectric polymer thin films, previously soaked in PBS, are transferred to deionized (DI) water to measure the concentration of ions released from the polymer into the solution using conductimetry. **d**, Modulus of the normalized electrochemical impedance of various dielectric films at 1 Hz after soaking in 10x PBS at 70 °C at $t/H^2 = 5$ d μm⁻² (except for PDMS, with $t/H^2 = 1.55$ d μm⁻²). For the SU-8, PFPE-DMA, PHFIPA, PPFHEA, H-SEBS and PDMS samples, $n = 4, 4, 4, 4, 12$ and 8, respectively, where the

values are shown as the mean ± s.d., using one-way ANOVA (analysis of variance) with Dunnett's multiple comparison test and SU-8 as the control group. (The values obtained for each measurement are shown by the filled grey symbols.) ***$P < 0.005$, ****$P < 0.0001$. **e**, Concentration of ions released in DI water per polymer volume as a function of t/H^2 at 4, 37 and 65 °C during EEC measurements. **f**, Comparison of the ionic conductivity of dielectric polymers soaked in 1x PBS at 37 °C obtained using both measurement methods. For EIS, we show our previously reported results for PDMS and H-SEBS (mean ± s.d.)[37] and compare them with the data obtained for PFPE-DMA and SU-8 in this work ($n = 4$ samples for each material, mean ± s.d.). **g**, Modulus of electrochemical impedance for the PFPE-DMA and SU-8 thin films in 1× PBS at 37 °C as a function of the soaking time. Average thicknesses are 1 μm for the PFPE-DMA films and 800 nm (a double layer of two 400-nm-thick films to reduce pinholes) for the SU-8 films ($n = 4$ samples for each material, and data are shown as the mean ± s.d.). **h**, Nominal stress–stretch curves for the dielectric polymer films. **i**, Elastic modulus as a function of $t_{1/2}/H^2$ (which corresponds to the time required to decrease the initial modulus of the normalized impedance by 50%) measured at 1 kHz when soaked in 1x PBS at 37 °C for the different dielectric polymers. Individual data points for PDMS and H-SEBS were obtained from our previous work[37]. Values shown are the mean ($n = 4$ samples) for PI, PFPE-DMA and SU-8. The values for PFPE-DMA and SU-8 are higher than 500 d μm⁻².

$$\sigma = 2\frac{q^2}{kT}D \times S \times C_{out} \tag{1}$$

Q14

where σ is the ionic conductivity, q is the elementary charge, k is the Boltzmann constant, T is the temperature, D is the ionic diffusivity, S is

the ionic solubility and C_{out} is the concentration of ions in the surrounding biofluids at equilibrium (Supplementary Discussion 4). Notably, because ionic diffusivity in standard dielectric elastomers is in the range of 10^{-15} to 10^{-17} m² s⁻¹ at 37 °C, this instability can only be observed in micrometre-thick dielectric films over a timescale of days to weeks, which is critical for long-term neural recording.
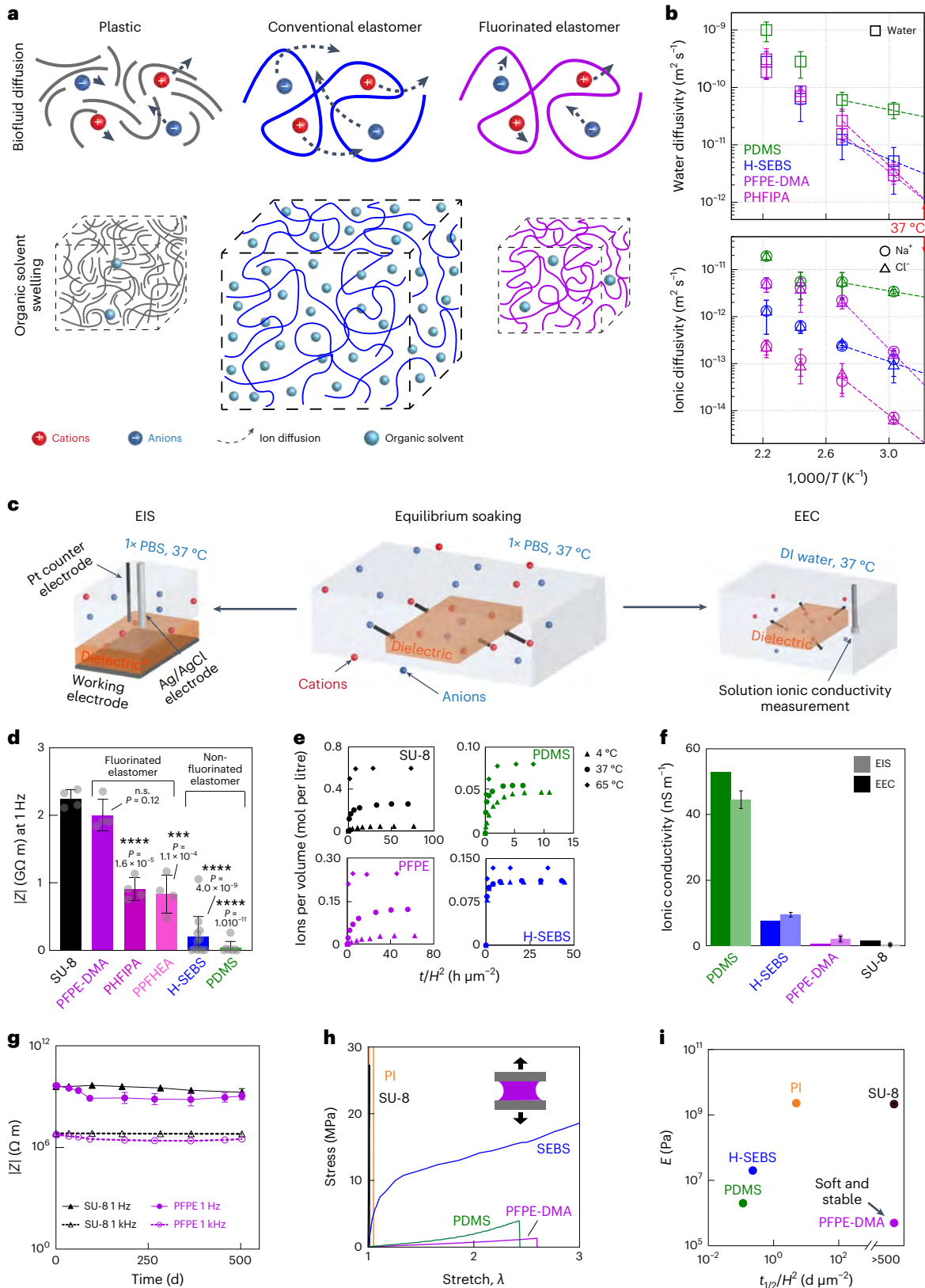
We used molecular dynamics (MD) simulations to study the diffusion of water and sodium chloride across different dielectric elastomers to better understand this ion-diffusion process and identify material systems that could potentially solve this issue (see Methods, Extended Data Fig. 3 and Supplementary Tables 1 and 2). Our MD simulations revealed that, towards 37 °C, the molecular diffusivity of water and sodium and chloride ions in fluorinated elastomers (PFPE-DMA and PHFIPA) is significantly lower than that in conventional elastomers (PDMS and H-SEBS) (Fig. 2b). This lower diffusivity suggests that fluorinated elastomers can have a lower ionic conductivity (Supplementary Discussion 4 and equation (1)) than conventional elastomers, which could allow them to maintain their dielectric performance during long-term immersion in physiological solutions. To test this hypothesis, we systematically characterized the long-term electrochemical stability of eight different dielectric materials, which comprised three fluorinated elastomers (PFPE-DMA, PHFIPA and poly[2-(perfluorohexyl) ethyl]acrylate (PPFHEA)), three non-fluorinated elastomers (PDMS, H-SEBS and polyisobutylene (PIB)) and two plastic dielectric polymers (polyimide (PI) and SU-8 2000.5 (SU-8)) as controls.

We evaluated the ionic conductivity of the dielectric polymers (see Methods, Supplementary Discussion 5 and Supplementary Table 3) (Fig. 2c) using electrochemical impedance spectroscopy (EIS)[37] (Extended Data Fig. 4a–c) and external electrolyte conductimetry (EEC) techniques (Extended Data Fig. 5a,b). We used an electrical model of the dielectric material with conductive losses to estimate the ionic conductivity from EIS data (Extended Data Fig. 4a–c and Supplementary Table 4)[37,41]. To conduct an accelerated ageing test, we soaked the polymer thin films in 10x PBS solution at 65 °C. Bode plots of normalized electrochemical impedance (Z) before and after soaking (Extended Data Fig. 4d) showed substantial impedance reduction for the conventional elastomer and PI films across the 0–1,000 Hz range, whereas SU-8 and the fluorinated elastomer films exhibited a slight decrease. At low frequency (<1,000 Hz), all of the fluorinated elastomer films showed a lower impedance modulus drop than the PDMS, H-SEBS, PIB and PI films. To account for variations in diffusion times due to differences in thickness among the samples (Supplementary Table 4), we plotted the progressive decrease in impedance modulus at 1 Hz and 1 kHz (Fig. 2d and Extended Data Fig. 4e,f) as a function of the time (t) normalized by the square of the average thickness (H) of the polymer films. A larger reduction in normalized impedance is observed for the non-fluorinated elastomers at 1 Hz. In addition, we extrapolated average dielectric constants of the dielectric thin films in the frequency range of 1,000–100,000 Hz from the EIS plots (Supplementary Table 5), confirming the low dielectric constant of PFPE-DMA ($\varepsilon = 1.99 \pm 0.03$), consistent with previous reports[42,43].

Using EEC (Fig. 2c and Extended Data Fig. 5a), we further analysed the ionic diffusivity, solubility and conductivity of four representative dielectric polymers, excluding the remaining polymers due to sample-preparation limitations (see Supplementary Discussion 5 and Supplementary Table 3). The ionic conductivity changes in DI water indicate the ion-diffusion rates from these polymers (Fig. 2e). The value of the plateau in the solution's conductance is proportional to the ionic solubility, S. We determined the ionic diffusivity, D, by fitting the experimental data (see Supplementary Discussion 5 and Extended Data Fig. 5b,c) and calculated ionic conductivity using equation (1).

The results from both methods[37] (Fig. 2f and Supplementary Table 6) consistently showed that the ionic conductivity of PFPE-DMA is similar to that of SU-8 but 1–2 orders of magnitude lower than the other dielectric elastomers. This reduced ionic conductivity is mostly attributed to its low ionic diffusivity (Extended Data Fig. 5d and Supplementary Table 6), aligning with MD simulations.

We carried out EEC measurements at different temperatures to calculate the average ion-diffusion activation energy and the heat of solution between 4 and 65 °C (refs. 44–46) (Extended Data Fig. 5e–g and Supplementary Table 7). The average activation energy for PFPE-DMA is even higher than SU-8, and its enthalpy of the solution is closer to SU-8 but higher than hydrocarbon elastomers. This aligns with our MD simulations showing low ionic diffusivity in PFPE-DMA (Fig. 2b). The MD simulations suggested a correlation between ionic diffusivity and polymer density (Extended Data Fig. 3c,d), but further simulations to analyse the molecular mechanism of diffusion are required to understand the difference between fluorinated and hydrocarbon elastomers. In addition, PFPE-DMA has a low water permeability (Supplementary Table 8), comparable to that of PIB, which could contribute to its long-term stability in biofluids.

Our results highlighted the stability of the dielectric performance of fluorinated dielectric elastomers in biofluids. We further tested PFPE-DMA as a long-lived dielectric material for implantable bioelectronics, given its potential in nanofabrication[22,23]. The results showed that the PFPE-DMA film is as stable as the SU-8 double layers over a soaking period of 17 months (Fig. 2g). Notably, the elastic modulus of the crosslinked PFPE-DMA film is 0.50 MPa, which is approximately 10,000 times softer than SU-8 (Fig. 2h and Extended Data Fig. 6a–e). We plotted the elastic modulus against the half-life time ($t_{1/2}$) of the thin-film dielectric impedance at 1 kHz, which is defined as the soaking time required for the initial impedance modulus to decrease by 50% (Extended Data Fig. 4f). PFPE-DMA uniquely combines both mechanical softness and long-term dielectric performance stability (Fig. 2i), making it ideal for implantable neural probes in spatiotemporally scalable in vivo electrophysiology.

3D scalable neural probes

We developed a 3D photolithographic protocol using PFPE-DMA elastomers for scalable neural probe fabrication. Traditional elastomers are not suitable for multilayer photolithography as the organic solvents used in the process[21,47] easily cause the elastomers to swell, damaging the thin-film microstructures and microelectronic components. PFPE-DMA elastomers, however, have demonstrated chemical orthogonality[20,48], resisting both organic and aqueous solvents, preserving their surface even after intensive nanofabrication. However, the high contact angle with other conventional photo-patternable dielectric materials and the low surface adhesion energy to metals prevent the direct patterning of metals on PFPE-DMA elastomers. In addition, sensitivity to oxygen during crosslinking limits the resolution of mask-based photolithographic patterning of PFPE-DMA elastomers. To overcome these challenges, we developed the following technological advancements: (1) a 3D-printable nitrogen diffuser integrated with conventional photoaligners to create an inert atmosphere during exposure to ultraviolet (UV) light, enabling microscale photopatterning of PFPE-DMA (Extended Data Fig. 7a–c); (2) a photopatterned
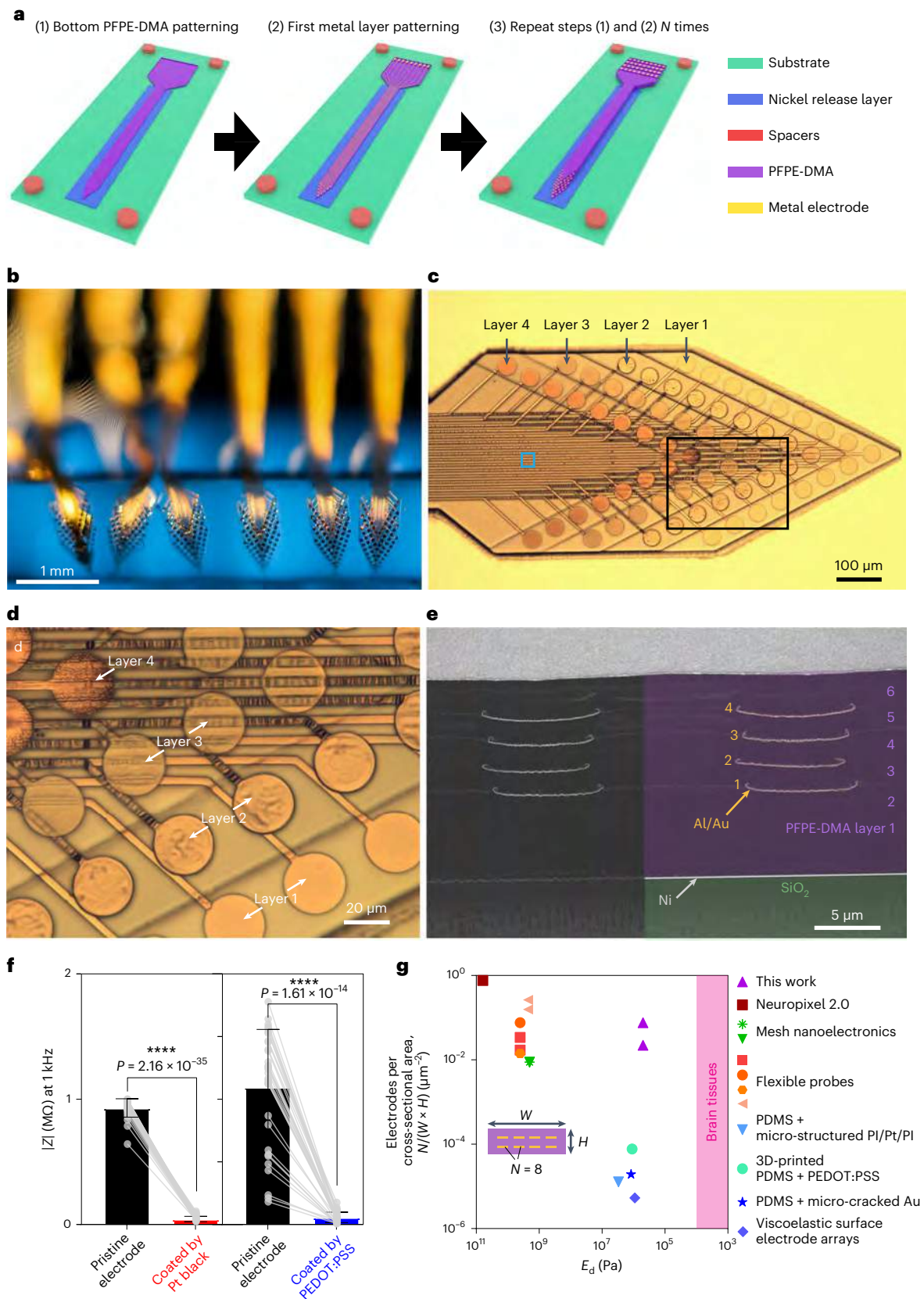
Fig. 3 | 3D integration of high-density soft microelectrode arrays for scalable neural probes. a, Schematics showing the stepwise nanofabrication process of a multilayer neural probe encapsulated by PFPE-DMA elastomers. **b**, Photograph of PFPE-DMA elastomer-encapsulated neural probes with four layers of electrode arrays self-wrapping on a glass capillary. **c**, BF micrograph of the neural probe in **b**. **d**, Expanded merged BF micrograph of the region in **c** highlighted by the black box. **e**, Focused ion beam (FIB) combined with SEM image showing the cross-section of the region in **c** highlighted by the blue box. Each layer is pseudo-coloured and labelled. **f**, Change in the impedance modulus at 1 kHz before and after electroplating with Pt black or PEDOT:PSS for 40-μm-diameter electrodes of neural probes ($n = 32$). The data in the bar plots show the mean ± s.d. and the grey dots show the values obtained for individual electrodes. ****$P < 0.0001$, two-tailed, paired t-test. **g**, Electrodes per cross-sectional area of state-of-the-art neural probes as a function of the elastic modulus of the dielectric encapsulation[6,11–13,17,35,54,55]. N, number of electrodes; W, probe width; H, probe height.

spacer to prevent direct contact between the PFPE-DMA precursor and the photomask, preserving the nanometre smoothness of the PFPE-DMA film during photolithography (Extended Data Fig. 7d,e); (3) treatment with an inert gas plasma to decrease the contact angle of the photoresists and increase adhesion to other materials (Extended Data Fig. 7f–h); and (4) high-pressure sputtering of metal oxide/metal layers to deposit metal lines and prevent metal-ion diffusion into PFPE-DMA. Processes (1)–(4) can be repeated to create multilayered microelectronic structures. Importantly, these innovations enable PFPE-DMA to be processed as a negative photo-patternable dielectric

a (1) Bottom PFPE-DMA patterning (2) First metal layer patterning (3) Repeat steps (1) and (2) *N* times

Substrate
Nickel release layer
Spacers
PFPE-DMA
Metal electrode

b 1 mm

c Layer 4 Layer 3 Layer 2 Layer 1 100 μm

d Layer 4 Layer 3 Layer 2 Layer 1 20 μm

e 6 5 4 3 2 4 3 2 1 Al/Au PFPE-DMA layer 1 Ni SiO$_2$ 5 μm

f $|Z|$ (MΩ) at 1 kHz
**** $P = 2.16 \times 10^{-35}$
**** $P = 1.61 \times 10^{-14}$
Pristine electrode / Coated by Pt black / Pristine electrode / Coated by PEDOT:PSS

g Electrodes per cross-sectional area, $N/(W \times H)$ (μm^{-2})
E_d (Pa)
W, H, $N = 8$
Brain tissues
This work
Neuropixel 2.0
Mesh nanoelectronics
Flexible probes
PDMS + micro-structured PI/Pt/PI
3D-printed PDMS + PEDOT:PSS
PDMS + micro-cracked Au
Viscoelastic surface electrode arrays

material in a standard cleanroom, establishing PFPE-DMA as an elastomer that is compatible with conventional photolithographic processes for 3D electronics (Fig. 3a, Extended Data Fig. 7a and Methods).

Figure 3b shows the flexibility of a neural probe with 64 electrodes on a glass capillary (Extended Data Fig. 8a–c). The corresponding bright-field (BF) optical image shows one probe containing six layers of PFPE-DMA sandwiching four layers of metal electrodes (Fig. 3c,d and Extended Data Fig. 8d–i). Scanning electron microscopy (SEM) imaging (Extended Data Fig. 8h–k) is used to confirm the smooth surface of the PFPE-DMA dielectric layers after the ten-layer fabrication process. We achieved a lateral resolution of approximately 1 μm for the PFPE-DMA features (Extended Data Fig. 8d–l), and surface treatment enabled standard photoresists to define precise features on the PFPE-DMA film (Extended Data Fig. 8g–i,l). Notably, there was no delamination between the PFPE-DMA and metal layers (Fig. 3e and Extended Data Figs. 8m–o and 6n–t), even after a uniaxial stretch to 20% (Extended Data Fig. 8o). Adhesion testing[49,50] (Extended Data Fig. 6f–k) showed that the self-adhesion energy of the PFPE-DMA layers was substantially higher than their adhesion energy to a glass substrate and was closer to their intrinsic fracture toughness measured (Extended Data Fig. 6e), indicating that the two PFPE-DMA layers adhere strongly and do not delaminate easily under strain. Delamination between layers was not observed on the 64-channel, four-metal-layer neural probes after >20% of uniaxial stretch (Extended Data Fig. 6l). In addition, accelerated ageing in saline did not induce delamination between the PFPE-DMA and metal layers (Extended Data Fig. 6n–t).

We measured the conductivity of the metal interconnects and electrodes on PFPE-DMA as a function of their aspect ratio (Extended Data Fig. 8p), and found average conductivity values consistent with standards for sputtered Al/Au (40/100 nm) metal lines. Our fabrication method is compatible with three-inch wafer-scale fabrication processes (Extended Data Fig. 8q). To facilitate connections to recording setups, we overexposed the PFPE-DMA layers to create smooth steps at their edges and used isotropic metal deposition to continuously deposit the metal electrodes from different PFPE-DMA layers to the input/output (I/O) pads, enabling standard flip-chip bonding of flexible cables (Extended Data Fig. 7i–m). Finite element analysis indicated that the strain concentration in the central metal layer remains below the yield strain of Au when bent (Extended Data Fig. 2f–h), suggesting that metal interconnects will not undergo plastic deformation or fracture. The adhesion of the metal lines to the elastomer is even sufficient to generate wrinkle patterns, which are commonly observed in laminates[34,51] (Fig. 3d and Extended Data Fig. 8g–i) with a stiff island on a soft substrate, where larger strains can be accommodated before failure of the stiff layer compared with the free-standing fracture strain[51–53]. This result can explain further why metal lines are still highly conductive after 5% uniaxial strain (Extended Data Fig. 6m).

Q26 After chip bonding, we used standard electroplating techniques to coat the electrode tips with poly(3,4-ethylenedioxythiophene) polystyrene sulfonate (PEDOT:PSS) or platinum black (Pt black) to verify the conductivity of the electrodes (see Methods and Extended

Data Fig. 8r,s). The reduced electrochemical impedance matches previously reported values and is comparable to other implantable brain probes[6,12,13] (Fig. 3f). We also conducted chronic measurements of the impedance of sputtered Al/Au interconnects and Pt electrodes to confirm the stability of fluorinated elastomer-based neural probes without additional effects from the electroplated material (Extended Data Fig. 8t). Finally, we showed that the crosstalk level between neighbouring electrodes in a relevant test geometry was comparable to standard values measured in polymer microelectrode arrays after more than 50 days of soaking time in 1x PBS (Extended Data Fig. 4g–j)[24]. Q27 Collectively, compared with state-of-the-art neural probes made with other soft materials and thin-film plastic passivation, PFPE-based neural probes, respectively, increase the density of the electrodes by over two orders of magnitude (up to 7.6 electrodes per 100 μm² of the cross-section in this work)[35,54–56] and increase the mechanical softness by between four and five orders of magnitude (Fig. 3g and Supplementary Table 9)[6,11–13,17,57,58].

Multilayer neural probes encapsulated by dielectric elastomers are still more flexible than probes made with plastic dielectric materials. Comparing neural probes made using 9-μm-thick PFPE-DMA or Q28 SU-8, the PFPE-DMA-based probes exhibit substantially higher flexibility (Extended Data Fig. 2f–h). Finite element analysis confirms the difference in their flexibility to be due to the different elastic modulus values between the elastomeric and rigid dielectric materials. Specifically, the SU-8 layer is the principal load-carrying member in the SU-8-based probe, whereas in the PFPE-DMA-based probe, the PFPE-DMA layer contributes negligibly to the load-carrying capacity. Instead, the nanometre-thick metal layer is the principal load-carrying member. As a result, a simple beam model with three electrode layers shows that this design reduces the contribution of the encapsulation layers to the overall flexural rigidity of the neural probe by a factor of 900 (Extended Data Fig. 2b).

Long-term stable neural electrophysiology

We implanted neural probes in the mouse brain for chronic recording. Q29 The soft neural probes were delivered into the brain following the previously reported method (Extended Data Fig. 9a–c and Methods)[59]. The PFPE-DMA probes have four-layer electrode arrays vertically integrated, with a cross-sectional area approximately 150–500 times larger than that of an ultraflexible probe[17,18], thus enabling a high density of 64 electrodes to be packed in one probe (Fig. 4a), and they were implanted in the somatosensory cortex and connected to a voltage amplifier through a flat flexible cable for electrophysiological recording (Extended Data Fig. 9d and Methods).

We compared the brain immune response of multilayer PFPE-DMA probes with SU-8 probes of the same thickness (Fig. 4b,c). At twelve weeks post-implantation, we observed a significant enhancement of the NeuN (neuron) signal around the PFPE-DMA probes compared with the SU-8 probes. In addition, the fluorescence intensity of astrocytes and microglia at twelve weeks post-implantation was significantly reduced around the PFPE-DMA probes in comparison with the SU-8 probes.

Fig. 4 | Long-term stable brain electrophysiology and implantation with reduced immune responses by scalable soft neural probes. a, BF image of a multilayer, high-density PFPE-DMA neural probe with four layers of electrode Q30 arrays and 64 channels after Pt black electrodeposition. **b**, Representative Q31 immunostaining of horizontal brain slices at two (top), six (middle) and twelve weeks (bottom) post-implantation. The green, pink, cyan, blue and red colours show signals corresponding to neurons (NeuN), astrocytes (GFAP), microglia (IBA1), the DAPI dye and rhodamine 6G, respectively. The PFPE-DMA and SU-8 brain probes are both 9 μm thick and 250 μm wide. **c**, Normalized average fluorescence intensity of NeuN, GFAP and IBA1 signals as a function of distance from the probe–tissue interfaces at two, six and twelve weeks post-implantation. The fluorescence intensity at 500–525 μm away from the probe was used for Q32 normalization (n = 4 brain slices, mean ± s.e.m., *P < 0.05; **P < 0.01, ***P < 0.01,

two-tailed unpaired t-test for distance between 0 and 250 μm away from the probe). **d**, Left: representative voltage traces (300–3,000 Hz bandpass Q33 filtered) recorded from a high-density PFPE-DMA neural probe at four weeks post-implantation. Right: unit activities of the region highlighted by the dashed red box in the left panel. **e**, Average single-unit waveforms detected in **d. f**, Representative ISI plots over ten weeks of recording. **g**, Representative Q34 average waveforms from two to ten weeks post-implantation. **h**, Clusters of Q35 the waveforms detected in **g** in PCA space as a function of the number of weeks post-implantation. PC1 and PC2 represent the first two axes in the PCA from the clustering algorithm. **i–k**, Peak–valley amplitude (**i**), firing rate (**j**) and waveform similarity (**k**) of the units detected in **g** and **h** as a function of the post-implantation time (n = 14 units, mean ± s.d.).

However, the difference in the microglia signals was marginal. These results demonstrate that the 3D vertically stacked, multilayer PFPE-DMA probes can maintain long-term biocompatibility with the brain tissue.

Chronic recording (Fig. 4d,e) showed that single-unit action potentials were recorded stably over an implantation period of ten weeks, with minimal change in the interspike interval (ISI) distribution (Fig. 4f) and waveform shape (Fig. 4g). Moreover, principal component analysis (PCA) showed that all units exhibited nearly constant positions on the first and second principal component plane (PC1–PC2) from two to ten weeks post-implantation (Fig. 4h). In addition, the amplitude,
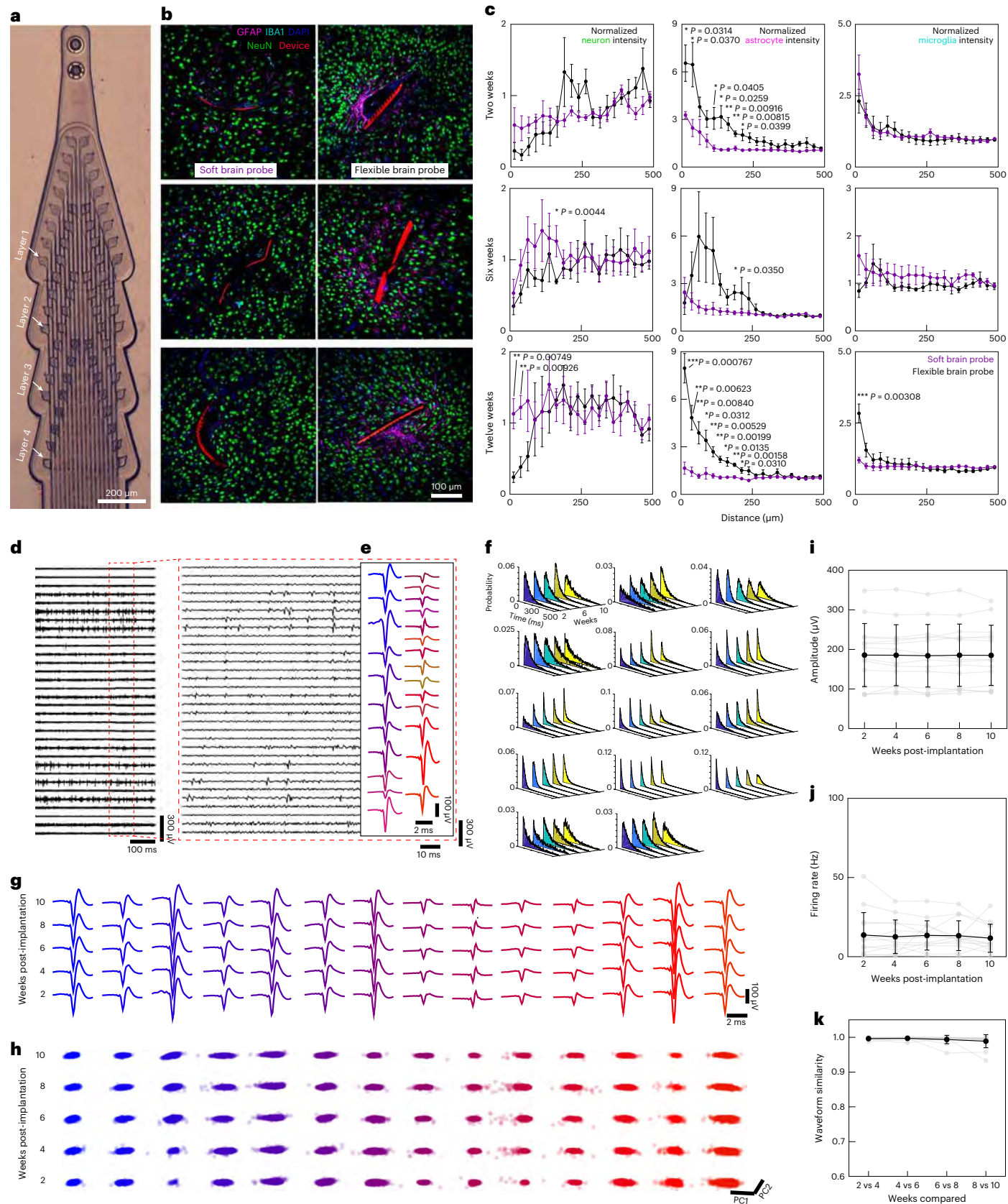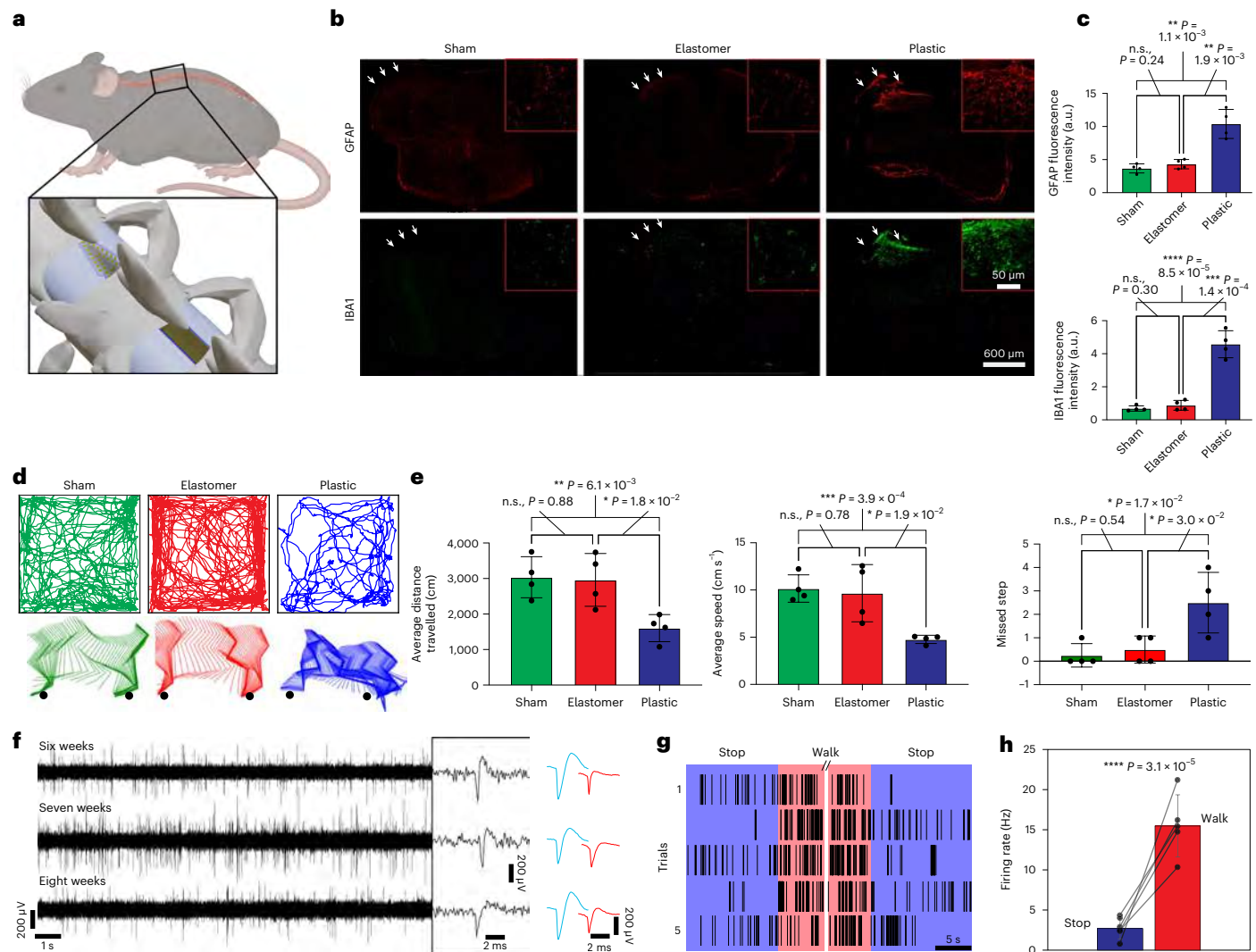
Fig. 5 | Long-term stable spinal cord recording. a, Schematic of the spinal cord-implanted mice. **b**, Representative confocal fluorescence images showing GFAP (astrocytes) and IBA1 (microglia) staining in the sections of spinal cord tissues from sham control mice (left) and mice implanted with PFPE-DMA (elastomer, middle) and PI (plastic, right) probes at six weeks post-implantation. The insets show expanded panels to highlight the contact area with the implanted neural probes. **c**, Bar plots showing the statistical summary of the astrocyte (top) and microglia (bottom) fluorescence intensities in the regions of interest, where the spinal cord tissues received sham surgery or were implanted with neural probes (white arrows in **b**). Data were obtained for $n = 4$ independent biological replicates, mean ± s.d., two-sided, unpaired t-test. **d**, Top: representative data showing the motion traces for a sham control animal (green) and animals implanted with PFPE-DMA (red) and PI (blue) neural probes at four weeks post-

implantation. Bottom: representative data showing the hindlimb kinematics. **e**, Bar plots summarizing the average distance travelled (left), average movement speed (middle) and number of missed steps onto the rungs of the ladder (right) for the motion-trace characterization ($n = 4$ independent experiments, mean ± s.d., two-sided, unpaired t-test) at four weeks post-implantation. **f**, Left: voltage traces (filtered in the 250–3,000 Hz range) of a representative channel showing spike-like electrical activity from post-implantation periods of six to eight weeks. Middle: expansion showing the representative spike-like electrical signals. Right: Sorted spiking units identified from the left panel. **g**, Raster plot of spike-like signals in a representative channel during mouse resting and walking states. **h**, Average firing rate between animal walking and resting states ($n = 5$ independent experiments, two-tailed paired t-test). Panel **a** created with BioRender.com.

firing rate and waveform similarity remained constant over all the recording sessions, suggesting that the high-density, multilayer soft probe could stably track the activity from the same neurons over time (Fig. 4i–k). We also confirmed the stability of brain recording using a PFPE-DMA probe with a single-layer electrode array (approximately 2-μm-thick PFPE-DMA) to further validate the dielectric stability of the ultrathin PFPE-DMA encapsulation layer during chronic brain recording (Extended Data Fig. 10).

The stretchability of the PFPE-DMA dielectric layer enables the multilayer neural probe to tolerate more strain and introduce less mechanical damage to the tissue during the bending. To demonstrate this, we performed chronic electrophysiology on the mouse spinal cord (Fig. 5a and Methods). We first characterized the

long-term immune response by comparing the immune response from PFPE-DMA and PI probes with that of sham-operated controls (Methods). PI probes of 25 μm thickness were used as standard for flexible spinal cord implants[60], which are robust enough to withstand the surgical procedure and chronic implantation. The sham-operated group of animals received spinal cord surgery but no device implant. Neuroinflammatory responses at chronic stages were evaluated by the density of astrocytes (GFAP) and microglia (IBA1) for foreign-body reactions, which showed that the density of astrocytes and microglia increased in the vicinity of PI probes at six weeks post-implantation. By contrast, there was no significant difference between mice with PFPE-DMA probes and sham-operated animals (Fig. 5b,c).

We characterized the impact of implantation on animal behaviours by measuring freely moving mice in an open-field box and whole-body movement during basic walking and skilled locomotion across a horizontal ladder (Fig. 5d). Statistical results showed that, compared with sham controls, mice implanted with PI probes showed a reduction in the average distance travelled and average speed during movements, as well as motor deficits, whereas mice implanted with the PFPE-DMA probes showed no significant differences (Fig. 5e). Using the implanted electrodes, we recorded the spike-like electrical activity from the representative electrodes over several weeks (Fig. 5f), with changes in firing rate corresponding to the animal resting and walking states (Fig. 5g,h). The observed spikes exhibit prolonged durations (2–4 ms) and heightened amplitudes (250–500 µV). This phenomenon has been noted previously in depth probe spinal cord recordings of mice[60]. However, further investigation is required to determine if these spikes are indicative of multi-unit action potentials or local field potentials. These results show that PFPE-DMA soft neural probes implanted in the mouse spinal cord do not affect the animal behaviour and can provide a stable recording of spinal cord electrical activity.

Conclusion

Our results showed that neural probes can be made with four layers of fluorinated elastomer/metal structures. An analytical model based on Euler–Bernoulli beam theory (Supplementary Discussion 3) shows that probes with up to nine layers have a flexural rigidity (that is, a bending stiffness per unit width) below 1 µN m, whereas probes encapsulated by plastic dielectrics with only three layers of electrodes have a flexural rigidity above 1 µN m (Extended Data Fig. 2b,c). In practice, plastic probes thicker than 10 µm are brittle, whereas elastomer-encapsulated probes remain flexible and robust for implantation (Supplementary Video 1).

It has been demonstrated that ultrasoft neural probes with larger cross-sections can achieve long-term stable neural recordings compared with thin rigid plastic probes[17,18]. These ultrasoft probes can support more channels. We recognize that the extreme modulus mismatch between the Au and PFPE-DMA layers may lead to a split of the neutral axis[61], which could reduce the flexural rigidity. However, an analytical model based on previous work[62] indicates that Euler–Bernoulli theory still applies to the majority of the probe's length (see Supplementary Discussion 3 and Extended Data Fig. 2d,e). In practice, the main limitations in scaling these probes will probably come from microfabrication challenges (see Supplementary Discussion 6).

When the elastic modulus of the dielectric layer is significantly below the megapascal level, its contribution on the total flexural rigidity of the probe is minimal and metal layers dominate the probe's mechanical properties. Therefore, as the number of layers increases, the benefit decreases asymptotically because the metal layers located further from the neutral axis contribute more to the flexural rigidity of the probe (Extended Data Fig. 2a and Supplementary Discussion 3). To reduce this rigidity, strategies, such as adjusting the metal-layer placements, increasing the outer elastomer thickness to prevent signal leakage or using softer conductors such as liquid metal[63], can be considered.

Online content

Any methods, additional references, Nature Portfolio reporting summaries, source data, extended data, supplementary information, acknowledgements, peer review information; details of author contributions and competing interests; and statements of data and code availability are available at https://doi.org/10.1038/s41565-023-01545-6.

References

1. Sadtler, P. T. et al. Neural constraints on learning. *Nature* **512**, 423–426 (2014).
2. Gallego, J. A., Perich, M. G., Chowdhury, R. H., Solla, S. A. & Miller, L. E. Long-term stability of cortical population dynamics underlying consistent behavior. *Nat. Neurosci.* **23**, 260–270 (2020).
3. Perlmutter, J. S. & Mink, J. W. Deep brain stimulation. *Annu. Rev. Neurosci.* **29**, 229–257 (2006).
4. Patel, S. R. & Lieber, C. M. Precision electronic medicine in the brain. *Nat. Biotechnol.* **37**, 1007–1012 (2019).
5. Adolphs, R. The unsolved problems of neuroscience. *Trends Cogn. Sci.* **19**, 173–175 (2015).
6. Musk, E. An integrated brain–machine interface platform with thousands of channels. *J. Med. Internet Res.* **21**, e16194 (2019).
7. Lacour, S. P., Courtine, G. & Guck, J. Materials and technologies for soft implantable neuroprostheses. *Nat. Rev. Mater.* **1**, 16063 (2016).
8. Jun, J. J. et al. Fully integrated silicon probes for high-density recording of neural activity. *Nature* **551**, 232–236 (2017).
9. Tooker, A. et al. Optimization of multi-layer metal neural probe design. *Conf. Proc. IEEE Eng. Med. Biol. Soc.* **2012**, 5995–5998 (2012).
10. Salatino, J. W., Ludwig, K. A., Kozai, T. D. Y. & Purcell, E. K. Glial responses to implanted electrodes in the brain. *Nat. Biomed. Eng.* **1**, 862–877 (2017).
11. Liu, J. et al. Syringe-injectable electronics. *Nat. Nanotechnol.* **10**, 629–636 (2015).
12. Yang, X. et al. Bioinspired neuron-like electronics. *Nat. Mater.* **18**, 510–517 (2019).
13. Chung, J. E. et al. High-density, long-lasting, and multi-region electrophysiological recordings using polymer electrode arrays. *Neuron* **101**, 21–31 (2019).
14. Someya, T., Bao, Z. & Malliaras, G. G. The rise of plastic bioelectronics. *Nature* **540**, 379–385 (2016).
15. Khodagholy, D. et al. NeuroGrid: recording action potentials from the surface of the brain. *Nat. Neurosci.* **18**, 310–315 (2015).
16. Xie, C. et al. Three-dimensional macroporous nanoelectronic networks as minimally invasive brain probes. *Nat. Mater.* **14**, 1286–1292 (2015).
17. Luan, L. et al. Ultraflexible nanoelectronic probes form reliable, glial scar-free neural integration. *Sci. Adv.* **3**, e1601966 (2017).
18. Fu, T. M. et al. Stable long-term chronic brain mapping at the single-neuron level. *Nat. Methods* **13**, 875–882 (2016).
19. Dalvi, V. H. & Rossky, P. J. Molecular origins of fluorocarbon hydrophobicity. *Proc. Natl Acad. Sci. USA* **107**, 13603–13607 (2010).
20. Rolland, J. P., Van Dam, R. M., Schorzman, D. A., Quake, S. R. & DeSimone, J. M. Solvent-resistant photocurable 'liquid Teflon' for microfluidic device fabrication. *J. Am. Chem. Soc.* **126**, 2322–2323 (2004).
21. Liao, S., He, Y., Chu, Y., Liao, H. & Wang, Y. Solvent-resistant and fully recyclable perfluoropolyether-based elastomer for microfluidic chip fabrication. *J. Mater. Chem. A* **7**, 16249–16256 (2019).
22. Liu, J. et al. Fully stretchable active-matrix organic light-emitting electrochemical cell array. *Nat. Commun.* **11**, 3362 (2020).
23. Liu, Y. et al. Soft and elastic hydrogel-based microelectronics for localized low-voltage neuromodulation. *Nat. Biomed. Eng.* **3**, 58–68 (2019).
24. Qiang, Y. et al. Crosstalk in polymer microelectrode arrays. *Nano Res.* **14**, 3240–3247 (2021).
25. Fang, H. et al. Ultrathin, transferred layers of thermally grown silicon dioxide as biofluid barriers for biointegrated flexible electronic systems. *Proc. Natl Acad. Sci. USA* **113**, 11682–11687 (2016).
26. Grancarić, A. M. et al. Conductive polymers for smart textile applications. *J. Ind. Text.* **48**, 612–642 (2018).
27. Shoa, T., Mirfakhrai, T. & Madden, J. D. Electro-stiffening in polypyrrole films: dependence of Young's modulus on oxidation state, load and frequency. *Synth. Met.* **160**, 1280–1286 (2010).

28. Kim, Y. H. et al. Highly conductive PEDOT:PSS electrode with optimized solvent and thermal post-treatment for ITO-free organic solar cells. *Adv. Funct. Mater.* **21**, 1076–1081 (2011).

29. Yang, C. & Suo, Z. Hydrogel ionotronics. *Nat. Rev. Mater.* **3**, 125–142 (2018).

30. Minisy, I. M., Bober, P., Šeděnková, I. & Stejskal, J. Methyl red dye in the tuning of polypyrrole conductivity. *Polymer* **207**, 122854 (2020).

31. Matsuhisa, N. et al. Printable elastic conductors by in situ formation of silver nanoparticles from silver flakes. *Nat. Mater.* **16**, 834–840 (2017).

32. Sekitani, T. et al. A rubberlike stretchable active matrix using elastic conductors. *Science* **321**, 1468–1472 (2008).

33. Qu, J., Ouyang, L., Kuo, C.-C. & Martin, D. C. Stiffness, strength and adhesion characterization of electrochemically deposited conjugated polymer films. *Acta Biomater.* **31**, 114–121 (2016).

34. Matsuhisa, N., Chen, X., Bao, Z. & Someya, T. Materials and structural designs of stretchable conductors. *Chem. Soc. Rev.* **48**, 2946–2966 (2019).

35. Tringides, C. M. et al. Viscoelastic surface electrode arrays to interface with viscoelastic tissues. *Nat. Nanotechnol.* **16**, 1019–1029 (2021).

36. Yuk, H., Lu, B. & Zhao, X. Hydrogel bioelectronics. *Chem. Soc. Rev.* **48**, 1642–1667 (2019).

37. Le Floch, P. et al. Fundamental limits to the electrochemical impedance stability of dielectric elastomers in bioelectronics. *Nano Lett.* **20**, 224–233 (2020).

38. Song, E., Li, J., Won, S. M., Bai, W. & Rogers, J. A. Materials for flexible bioelectronic systems as chronic neural interfaces. *Nat. Mater.* **19**, 590–603 (2020).

39. Le Floch, P., Meixuanzi, S., Tang, J., Liu, J. & Suo, Z. Stretchable seal. *ACS Appl. Mater. Interfaces* **10**, 27333–27343 (2018).

40. Le Floch, P. et al. Wearable and washable conductors for active textiles. *ACS Appl. Mater. Interfaces* **9**, 25542–25552 (2017).

41. Bard, A. J. & Faulkner, L. R. *Electrochemical Methods: Fundamentals and Applications* (Wiley, 2000).

42. Olson, K. R. et al. Liquid perfluoropolyether electrolytes with enhanced ionic conductivity for lithium battery applications. *Polymer* **100**, 126–133 (2016).

43. Timachova, K. et al. Mechanism of ion transport in perfluoropolyether electrolytes with a lithium salt. *Soft Matter* **13**, 5389–5396 (2017).

44. Barrer, R. Permeability of organic polymers. *J. Chem. Soc. Faraday Trans.* **35**, 644–648 (1940).

45. Van Amerongen, G. Influence of structure of elastomers on their permeability to gases. *J. Polym. Sci.* **5**, 307–332 (1950).

46. Geise, G. M., Paul, D. R. & Freeman, B. D. Fundamental water and salt transport properties of polymeric materials. *Prog. Polym. Sci.* **39**, 1–42 (2014).

47. George, S. C., knörgen, M. & Thomas, S. Effect of nature and extent of crosslinking on swelling and mechanical behavior of styrene–butadiene rubber membranes. *J. Membr. Sci.* **163**, 1–17 (1999).

48. Vitale, A. et al. Direct photolithography of perfluoropolyethers for solvent-resistant microfluidics. *Langmuir* **29**, 15711–15718 (2013).

49. Gent, A. N. Fracture mechanics of adhesive bonds. *Rubber Chem. Technol.* **47**, 202–212 (1974).

50. Wang, Y., Yin, T. & Suo, Z. Polyacrylamide hydrogels. III. Lap shear and peel. *J. Mech. Phys. Solids* **150**, 104348 (2021).

51. Lacour, S. P., Jones, J., Wagner, S., Teng, L. & Zhigang, S. Stretchable interconnects for elastic electronic surfaces. *Proc. IEEE* **93**, 1459–1467 (2005).

52. Li, T., Huang, Z., Suo, Z., Lacour, S. P. & Wagner, S. Stretchability of thin metal films on elastomer substrates. *Appl. Phys. Lett.* **85**, 3435–3437 (2004).

53. Li, T., Suo, Z., Lacour, S. P. & Wagner, S. Compliant thin film patterns of stiff materials as platforms for stretchable electronics. *J. Mater. Res.* **20**, 3274–3277 (2005).

54. Yuk, H. et al. 3D printing of conducting polymers. *Nat. Commun.* **11**, 1604 (2020).

55. Minev, I. R. et al. Electronic dura mater for long-term multimodal neural interfaces. *Science* **347**, 159–163 (2015).

56. Vachicouras, N. et al. Microstructured thin-film electrode technology enables proof of concept of scalable, soft auditory brainstem implants. *Sci. Transl. Med.* **11**, eaax9487 (2019).

57. Steinmetz, N. A. et al. Neuropixels 2.0: a miniaturized high-density probe for stable, long-term brain recordings. *Science* **372**, eabf4588 (2021).

58. Guan, S. et al. Elastocapillary self-assembled neurotassels for stable neural activity recordings. *Sci. Adv.* **5**, eaav2842 (2019).

59. Cea, C. et al. Enhancement-mode ion-based transistor as a comprehensive interface and real-time processing unit for in vivo electrophysiology. *Nat. Mater.* **19**, 679–686 (2020).

60. Lu, Chi et al. Flexible and stretchable nanowire-coated fibers for optoelectronic probing of spinal cord circuits. *Sci. Adv.* **3**, e1600955 (2017).

61. Li, L. et al. Integrated flexible chalcogenide glass photonic devices. *Nat. Photonics* **8**, 643–649 (2014).

62. Li, S., Su, Y. & Li, R. Splitting of the neutral mechanical plane depends on the length of the multi-layer structure of flexible electronics. *Proc. R. Soc. A* **472**, 20160087 (2016).

63. Kim, M.-G., Brown, D. K. & Brand, O. Nanofabrication for all-soft and high-density electronic devices based on liquid metal. *Nat. Commun.* **11**, 1002 (2020).

64. Morin, F., Chabanas, M., Courtecuisse, H. & Payan, Y. in *Biomechanics of Living Organs: Hyperelastic Constitutive Laws for Finite Element Modeling* (eds Payan, Y. & Ohayon, J.) 127–146 (Elsevier, 2017).

Q60

Methods

Materials and devices

Materials. Dow Sylgard 184 silicone encapsulant was used to prepare the PDMS thin films and was obtained from Corning. PIB (Exxon Butyl 268S) was obtained from Vanderbilt Chemicals. H-SEBS (Tuftec H1062) was obtained from Asahi Kasei. PI (PI2545 HD) was obtained from MicroSystems. PHFIPA and PPFHEA were prepared from hexafluoroisopropyl acrylate and 2-(perfluorohexyl)ethyl acrylate, respectively, which were obtained from Fluoryx Labs. PFPE-DMA with a molecular weight in the range 8,000–10,000 kg mol^{-1} was synthesized by Axoft, Inc. as reported previously[22,23]. Fluorolink MD700 was obtained from Solvay and was used as a crosslinker for PHFIPA and PPFHEA. 2-Hydroxy-2-methylpropiophenone was used as a photoinitiator.

Preparation of dielectric polymer thin films for characterization. PFPE-DMA films. (1) Bis(2,4,6-trimethylbenzoyl)phenylphosphine oxide was used as photoinitiator, dissolved in bis(trifluoromethyl) benzene and mixed with PFPE-DMA, to prepare the photo-patternable precursor. (2) PFPE-DMA precursor was spin coated at 3,000 revolutions per min (r.p.m.). (3) The film was thermally dried for 2 min. (4) The film was exposed to UV light for a total dose above 150 mJ cm^{-2} under a nitrogen atmosphere.

SU-8 2002 bilayer films. (1) SU-8 2000.5 was spin coated at 3,000 r.p.m. (2) The film was baked at 65 °C for 2 min and at 95 °C for 2 min. (3) The film was exposed to UV light for a total dose above 150 mJ m^{-2} to completely cure the film and avoid pinholes. (4) The UV-cured film was post-baked at 65 °C for 2 min and at 95 °C for 2 min. (5) Defined patterns were developed using the SU-8 developer for 90 s, and then rinsed with isopropyl alcohol and blow-dried. (6) The developed patterns were hard-baked at 200 °C for 20 min. (7) Procedures (1)–(6) were repeated to define the second SU-8 layer to avoid pinholes.

PDMS (10:1) films. (1) PDMS base and curing agents (10:1 ratio) were mixed for 2 min and degassed for 2 min using a non-vacuum-type mixer (Thinky). (2) PDMS was spin coated at 5,000–8,000 r.p.m. (3) The PDMS films were baked at 65 °C overnight.

H-SEBS films. (1) H-SEBS was dissolved in toluene at 70–100 mg ml^{-1} and stirred for 48 h at 40 °C in a closed container. (2) The precursor solution was spin coated immediately at 1,000–2,000 r.p.m. after pouring it onto the substrate. (3) H-SEBS films were dried at 80 °C overnight.

PIB films. (1) Butyl 268S was dissolved in toluene at 10% of the solvent weight. (2) The precursor solution was spin coated immediately at 1,000–2,000 r.p.m. after pouring it onto the substrate. (3) PIB films were dried at 80 °C overnight.

PI films. (1) The precursor was spin coated at 3,000–4,000 r.p.m. immediately after pouring it onto the substrate. (2) Films were hard-baked using an atmosphere-controlled oven (vacuum purging, then under a continuous nitrogen flow) first at 200 °C for 30 min and then at 350 °C for 60 min.

PHFIPA and PPFHEA films. (1) The precursor was spin coated at 1,500 r.p.m. for 40 s. (2) Films were post-baked at 95 °C for 2 min. (3) Films were exposed to UV light for a total dose above 150 mJ m^{-2} to completely cure the film avoiding pinholes, under a nitrogen atmosphere. (4) Films were hard-baked at 110 °C for 1 h.

Fabrication of PFPE-DMA encapsulated neural probes. All photoresists and developers were obtained from Kayaku Advanced Materials unless otherwise mentioned. (1) A 100-nm-thick Ni sacrificial layer was patterned on the thermal oxide silicon wafer (University Wafer). (2) SU-8 2010 was patterned as spacers. (3) Cr/Au (15/100 nm) I/O pads were deposited via electron-beam evaporation. (4) For the bottom PFPE-DMA layer, the PFPE-DMA precursor was spin coated on the wafer at 2,000–6,000 r.p.m. to obtain a thickness ranging from 500 nm to 3 μm depending on the rotation speed and precursor concentration. The spin-coated PFPE-DMA film was aligned in a photomask aligner and patterned with UV light (10–30 mJ cm^{-2}) using a laboratory-made nitrogen diffuser (Extended Data Fig. 7b,c). Then the PFPE-DMA was post-baked at 115 °C, developed in bis(trifluoromethyl)benzene and blown dry. (5) For surface treatment, the PFPE-DMA surface was activated with inert gas plasma for 2–6 min. (6) For the metal interconnects, LOR3A and S1805 or S1813 photoresists were patterned on the wafer as described above. Different combinations of metal films, such as Al/Au, Al/Au/Al, Al/Au/Pt, Ti/Au, Ti/Au/Ti, Cr/Au and Cr/Au/Cr, were deposited by sputtering at Ar with a low oxygen atmosphere[65], with thicknesses in the range of 20–100 nm for each layer. Finally, the metal layers were lifted off using Remover PG solvent stripper overnight. (7) For multiple PFPE-DMA/metal layers, PFPE-DMA was spin coated and UV-cured, followed by plasma surface treatment, lift-off resist patterning and metal sputtering to create an additional layer of interconnects, similar to steps (4)–(6). Repeating this process multiple times will enable multilayer structures. (8) For the top PFPE-DMA layer, using the same recipe described in step (4), the top PFPE-DMA layer will be patterned. (9) For the SU-8 framework for transfer, SU-8 2010 was used to define a framework holding the soft brain probe during release. (10) The multilayer soft probes were released in nickel etchant (Transene), which is compatible with Al- and Ti-based adhesion layers.

Electroplating of electrodes. We used an SP-150e potentiostat (BioLogic) along with its commercial software EC-lab V11.36 for electrodeposition. Electrodes from neural probes were connected to the working electrode. A platinum wire immersed in the precursor solution was used as the counter electrode, which also serves as the voltage reference. For the deposition of Pt black, the precursor solution consisted of 1 mM chloroplatinic acid solution and 25 mM sodium nitrate. Cyclic voltammetry with a potential varying from −1.0 V to 0.2 V at 0.05 V s^{-1} for 10–15 cycles was used. For PEDOT-PSS deposition, an electrolyte consisting of 0.01 M 3,4-ethylenedioxythiophene (Sigma-Aldrich) and 0.1 M poly(4-styrenesulfonic acid) sodium salt (Sigma-Aldrich) aqueous solution was used. The electrochemically polymerized reaction was performed under constant-voltage conditions. In the constant-voltage mode, the polymerization was carried out under a constant current of 1 V for 30 s.

Characterization

Thickness measurements. All thickness measurements were carried out using a DektakXT stylus profiler (Bruker). The force applied was set to 1 mg and the scan speed was 0.67 μm s^{-1}. Two-point surface levelling was applied using the commercial software of the tool.

Characterization of mechanical properties. Stress–strain curves and fracture toughness measurements were obtained using a testing machine (Instron) in uniaxial tension for specimens in the pure shear test geometry. A 90° peeling test was used to determine the adhesion energies.

Characterization of electrical properties. Current–voltage (I–V) curves for the metal interconnects on the PFPE-DMA substrates were measured using a probe station connected to an Axon Digidata 1550B plus HumSilencer to output controlled voltages. Input currents were amplified using a current pre-amplifier before measurement by the data acquisition card.

Characterization of surface properties. The contact angles of LOR3A and DI water on PFPE-DMA were determined using the free DropSnake plugin on ImageJ[65,66].

EIS measurements. The three-electrode setup used was the same as reported in our previous work[37]. For each measurement, three sweeps in frequency were measured, from 1 MHz down to 0.1 Hz. A sinusoidal voltage of 100 mV peak-to-peak was applied. Five points per frequency decade, logarithmically spaced, were measured. For each data point, the response to ten consecutive sinusoids (but spaced out by 10% of the period duration) was accumulated and averaged.

EEC measurements. A Traceable Conductivity Pocket Tester with Calibration was used to measure the conductance of the solutions. The two electrodes have an area of 1 cm² and are separated by 1 cm. The resolution of the sensor was 1 μS, and the temperature dependence of the conductance in the range of −5 to 50 °C was automatically compensated to give the value at 25 °C.

SEM and FIB imaging. A metal sputter coater was used to deposit a 20-nm-thick Pt/Pd layer and reduce the charging under the electron beam during the SEM imaging process. SEM images were taken under 5 kV voltage using a JEOL 7900F SEM instrument. Before FIB milling, another 100-nm-thick layer or Pt was deposited using the metal sputter coater atop the sample to prevent damage of the area of interest under ion beams. The FIB process followed conventional procedures using an FEI Helios 660 instrument in which a 30 kV Ga beam was used for rough milling and a reduced 10 kV voltage was used for fine milling. To inspect the sample surface of the FIB-milled cross-section, a secondary electron detector under 3 kV voltage was used to take the SEM images, which showed clear contrast and distinct layering out of the samples.

Animal experiments

Brain and spinal cord implantation. All animal experiments in this study were approved by the Institutional Animal Care and Use Committee of Harvard University under protocols 19-03-348 and 20-05-368. The implantations were carried out on male C57BJ/6 mice (25–35 g; 6–8 weeks of age), which were housed in a regular 12 h/12 h light/dark cycle. The animals were anaesthetized with 2–3% isoflurane and maintained under anaesthesia with 0.75–1% isoflurane during the implantation surgery. Two stainless-steel screws were implanted in the cerebellum and used as ground electrodes. A craniotomy was performed on the brain, and the cortical surface was exposed upon removal of the dura mater. The PFPE-DMA brain probe was placed on the surface of the cortex and inserted using a 75 μm tungsten wire anchored to the neural probe through a fabricated hole at the front end of the device. For histological studies, SU-8 devices of the same size were implanted contralaterally in mouse brains for comparison. For spinal cord implantation, PFPE-DMA and 25-μm-thick PI probes were implanted in the mice through the following steps. First, the mice were anaesthetized, placed on a heating pad and given a midline incision on their vertebrae to expose the spinal cord. Then, an approximately 1 × 1 mm window was drilled on the L2–L3 lumbar vertebrae and the dura mater was removed to expose the tissue. Next, PFPE-DMA and PI probes were inserted into the subdural space of the L2–L3 segments in mice. Finally, a group of mice that received spinal cord surgery without probe implantation was used as sham controls.

Q49 **Electrophysiological recordings.** For data acquisition, a Blackrock Microsystems CerePlex μ headstage was connected to the flat flexible cable on the head of the mice through a laboratory-made printed circuit board. We used a CerePlex Direct data acquisition card and the CerePlex software to record and filter the electrophysiological recordings. The electrophysiological recording data were analysed offline. In brief, raw recording data were filtered using a bandpass filter in the 300–3,000 Hz frequency range. Spike sorting was performed using Mountainsort 4 software (https://github.com/flatironinstitute/mountainsort). The amplitude for each recording channel was calculated by the peak-to-peak amplitude of all sorted spikes. The spiking times of each cluster (that is, each single unit) were used to compute the ISI histogram. Recordings of electrical activity from the spinal cord using chronically implanted PFPE-DMA neural probes were performed after between six and eight weeks of implantation. For the spike-like electrical activity, a 250–3,000 Hz frequency range filter was applied to the voltage signals in the CerePlex software, and a threshold detection at −5 s.d. PCA was used for dimension reduction and MATLAB's 'kmeans' function was used to cluster the extruded waveforms. Q50

Immunostaining. Brain tissue. Immunohistochemistry and confocal fluorescence imaging were performed according to our previous reports[11,67]. (1) Mice were anaesthetized with 40–50 mg per kg (body weight) sodium pentobarbital and then transcardially perfused with 1x PBS (40 ml) and 4% paraformaldehyde (40 ml) followed by decapitation. (2) The brains implanted with SU-8/PFPE-DMA probes were removed from the cranium and post-fixed in paraformaldehyde for 24 h at 4 °C. (3) The samples were transferred to sucrose solutions with a stepwise increase in concentration from 10% to 30% (w/v) until they sunk to the bottom. (4) The samples were embedded in optimal cutting temperature compound and cut into 30-μm-thick slices using a cryostat. Brains implanted with SU-8 brain probes with the same thickness were used as controls. (5) The brain slices were first incubated with primary antibodies (NeuN: 1:200 (ab177487, Abcam); GFAP: 1:200 (ab4674, Abcam or 3670, Cell Signaling Technology); IBA1: 1:100, (ab5076, Abcam or 17198, Cell Signaling Technology)) at 4 °C overnight. After washing with 1x PBS three times, the brain slices were incubated with secondary antibodies at room temperature for 3–4 h. (6) The brain slices were stained with 4′,6-diamidino-2-phenylindole (DAPI) for 10 min. (7) After washing with 1x PBS, all samples were imaged with a Leica TCS SP8 confocal microscope using the Leica Application Suite X software platform 3.5.5. Q51

Spinal cord tissue. (1) At six weeks post-implantation, mice were anaesthetized with 40–50 mg per kg (body weight) sodium pentobarbital and then transcardially perfused with 1x PBS (40 ml) and 4% paraformaldehyde (40 ml) followed by decapitation. (2) The spinal cord tissues were removed and post-fixed in paraformaldehyde for 24 h at 4 °C. (3) The fixed tissue samples were transferred to sucrose solutions with a stepwise increase in concentration from 10% to 30% (w/v) until they sunk to the bottom. (4) The samples were embedded in optimal cutting temperature compound and cut into 30-μm-thick slices using a cryostat. Spinal cords implanted with 25-μm-thick PI probes were used as controls, and a group of mice that received spinal cord surgery without implants was used as sham controls. (5) The spinal cord slices were incubated with primary antibodies (GFAP: 1:200 (ab4674, Abcam) and IBA1: 1:100 (ab5076, Abcam)) at 4 °C overnight. After washing with 1x PBS three times, the slices were incubated with secondary antibodies at room temperature for 3–4 h. (6) The spinal cord slices were stained with DAPI for 10 min. (7) After washing with 1x PBS, all samples were imaged with a Leica TCS SP8 confocal microscope using the Leica Application Suite X software platform 3.5.5.

Open-field testing. To perform the open-field analysis, we used a 40 × 40 × 40 cm (length × width × height) open arena. All animals were tested during their more active dark cycle in a sound-attenuated laboratory maintained at 23 °C. The animals were placed in the centre of the arena and allowed to freely explore the open-field enclosure for 10 min while being recorded with an overhead camera. Digital recordings were collected, and the central positions of the animals were labelled using the DeepLabCut (DLC) toolbox (https://github.com/DeepLabCut/DeepLabCut) for the motion analysis. The animals' movements were defined as periods when the velocity of the animals'

centre point averaged more than 2 cm s⁻¹. The distance travelled, average speed and percentage of mobility time were calculated from the 10 min recording.

Gait analysis. The behaviour setup for the ladder-rung test involved using a GoPro 11 camera at 240 frames per second to record the mice consecutively running on a custom-made ladder. In this test, the animals crossed horizontal ladders while their footfalls were being recorded. Animals were habituated to a ladder with regularly spaced rungs before any experiments were performed. We used DLC to label the hind paws and detect the footfall using a peak detection algorithm, with video verification by the researchers. We also used DLC to perform limb tracking of six hindlimb joints (toe, metatarsophalangeal joint, ankle, knee, hip and iliac crest) for kinematic analysis of the hindlimb trajectories.

Simulations

Molecular dynamics simulations. (1) Low-density polymer matrices (~60–70% of the equilibrium density of each polymer at 300 K) were generated with five water molecules or five NaCl molecules added as solutes. Each simulated polymer was simulated by 100 monomers per chain and 15 chains per simulation box. The full breakdown of the number of atoms per polymer architecture is summarized in Supplementary Table 2. (2) The Maestro Suite of Schrödinger LLC[68] was used to pack the polymer chains and water/NaCl molecules into a simulation box. The force field used to describe the potential energy of the systems is OPLS[69], as developed and optimized by Schrödinger. For every polymer–solute combination, five independently generated structures were created with the goal to better sample the phase space of the polymer and to obtain ensemble averages and uncertainties. (3) The MD simulations were run using the Desmond MD code[70]. A time step of 1 fs was used to evolve the equations of motion. Once generated, the structures were brought close to equilibrium at 300 K through a set of MD stages described in Supplementary Table 2. (4) At the end of the equilibration, a canonical simulation of 2 ns was run to determine the density of the polymer at 300 K. (5) To determine the diffusion, a simulation of 250 ns was run in the canonical ensemble. The positions of all atoms/molecules of interest were tracked and the mean squared displacement (MSD) was computed. The MSD versus time curve was then post-processed to detect linear regions with a slope (in the log–log plot) equal to unity (that is, corresponding to the diffusive regime). This protocol was repeated for all polymer structures at a different temperature to construct the Arrhenius plot for all polymers investigated.

Finite element analysis. Abaqus 6.12 was used to analyse the mechanical properties of different polymer probes. The goal of the simulations is to evaluate the strain and stress concentration of composite beams bending around a capillary of circular cross-sections under gravity. The probes are made of three layers: a 140-nm-thick central metal layer between two 4.5-μm-thick dielectric layers with the elastic modulus of PFPE-DMA or SU-8. The elements used are S4R5 or S4R, with a mesh size of 50 μm, and a contact between the probes and the capillary modelled by surface-to-surface normal forces only (shear-free contact).

Statistics and reproducibility

The results of the micrographs in Fig. 3c–e have been repeated independently for more than three wafers. The devices shown in Extended Data Fig. 6n–t were reproduced more than six times. The micrographic areas shown in Extended Data Fig. 7j,k have been captured for >32 interconnects. The results shown in Extended Data Fig. 8h–k,m–o have been repeated more than three times for each of the panels.

Reporting summary

Further information on research design is available in the Nature Portfolio Reporting Summary linked to this article.

Data availability

All data and materials that supporting the findings of this study are available within the paper and its Supplementary Information. Source data are provided with this paper.

Code availability

The authors declare that all the code supporting the findings of this study are available within the paper and its Supplementary Materials. DeepLabCut is available at https://github.com/DeepLabCut/DeepLabCut. Mountainsort 4 is available at https://github.com/flatironinstitute/mountainsort. DropSnake is available at https://bigwww.epfl.ch/demo/dropanalysis/.

References

65. Stalder, A. F., Kulik, G., Sage, D., Barbieri, L. & Hoffmann, P. A snake-based approach to accurate determination of both contact points and contact angles. *Colloids Surf. A Physicochem. Eng. Asp.* **286**, 92–103 (2006).
66. Chaure, F. J., Rey, H. G. & Quiroga, R. Q. A novel and fully automatic spike-sorting implementation with variable number of features. *J. Neurophysiol.* **120**, 1859–1871 (2018).
67. Zhao, S. et al. Graphene encapsulated copper microwires as highly MRI compatible neural electrodes. *Nano Lett.* **16**, 7731–7738 (2016).
68. Schrödinger Release 2021-2: Maestro (Schrödinger Inc., 2021).
69. Harder, E. et al. OPLS3: a force field providing broad coverage of drug-like small molecules and proteins. *J. Chem. Theory Comput.* **12**, 281–296 (2016).
70. Bowers, K. J. et al. Scalable algorithms for molecular dynamics simulations on commodity clusters. In *SC '06: Proc. 2006 ACM/IEEE Conference on Supercomputing* 43 (IEEE, 2006).

Author contributions

P.L.F., S.Z., R.L. and J.L. designed the experiments. P.L.F., H. Sheng, G.Z., C.S., W.W., X.W. and A.S. synthesized the fluorinated polymers. P.L.F. characterized the dielectric stability of polymer thin films. N.M. and B.K. conducted the MD simulations. P.L.F., R.L., H. Sheng, H.P. and X.G. developed the nanofabrication process for the neural probes. P.L.F., T.Y., J.L., X.G. and R.L. characterized the electrical properties of the neural probes. R.L. performed the SEM and FIB characterization. P.L.F. and S.Z. performed the animal experiments. P.L.F., S.P., H. Shen and X.T. analysed the electrophysiological recordings from behaving animals. J.K., Z.W., N.L. and Z.S. simulated and characterized the mechanical properties of the materials and devices. E.M. and K.B. conducted the finite element analysis. P.L.F. and J.L. wrote the manuscript. All authors discussed and commented on the manuscript. J.L. supervised the project.

Competing interests

P.L.F., H. Sheng and J.L. are on a patent application filed by Harvard University related to this work. P.L.F., H.P., X.G., A.S., J.L., T.Y. and J.L. declare financial interests in Axoft, Inc. All other authors have no competing interests.

Additional information

Extended data is available for this paper at https://doi.org/10.1038/s41565-023-01545-6.

Correspondence and requests for materials should be addressed to Jia Liu.

Check for updates

Full activation pattern mapping by simultaneous deep brain stimulation and fMRI with graphene fiber electrodes

Siyuan Zhao[1,2,5], Gen Li[1,5], Chuanjun Tong[3,4], Wenjing Chen[3], Puxin Wang[1,2], Jiankun Dai[3], Xuefeng Fu[1], Zheng Xu [1], Xiaojun Liu[1], Linlin Lu[1], Zhifeng Liang [3✉] & Xiaojie Duan [1,2✉]

Simultaneous deep brain stimulation (DBS) and functional magnetic resonance imaging (fMRI) constitutes a powerful tool for elucidating brain functional connectivity, and exploring neuromodulatory mechanisms of DBS therapies. Previous DBS-fMRI studies could not provide full activation pattern maps due to poor MRI compatibility of the DBS electrodes, which caused obstruction of large brain areas on MRI scans. Here, we fabricate graphene fiber (GF) electrodes with high charge-injection-capacity and little-to-no MRI artifact at 9.4T. DBS-fMRI with GF electrodes at the subthalamic nucleus (STN) in Parkinsonian rats reveal robust blood-oxygenation-level-dependent responses along the basal ganglia-thalamocortical network in a frequency-dependent manner, with responses from some regions not previously detectable. This full map indicates that STN-DBS modulates both motor and non-motor pathways, possibly through orthodromic and antidromic signal propagation. With the capability for full, unbiased activation pattern mapping, DBS-fMRI using GF electrodes can provide important insights into DBS therapeutic mechanisms in various neurological disorders.

[1] Department of Biomedical Engineering, College of Engineering, Peking University, Beijing 100871, China. [2] Academy for Advanced Interdisciplinary Studies, Peking University, Beijing 100871, China. [3] Institute of Neuroscience, Chinese Academy of Sciences, CAS Center for Excellence in Brain Sciences and Intelligence Technology, Key Laboratory of Primate Neurobiology, Chinese Academy of Sciences, Shanghai 200031, China. [4] School of Biomedical Engineering, Guangdong Provincial Key Laboratory of Medical Image Processing, Key Laboratory of Mental Health of the Ministry of Education, Southern Medical University, Guangzhou 510515, China. [5] These authors contributed equally: Siyuan Zhao, Gen Li. ✉email: zliang@ion.ac.cn; xjduan@pku.edu.cn

The electrical stimulation of neural tissues forms the basis of current and emerging neural prostheses and therapies, including deep brain stimulation (DBS) for movement disorders, cochlear implants for deafness, retinal and cortical implants for blindness, spinal cord stimulation for chronic pain, limb stimulation for stroke and spinal cord injury, and vagus nerve stimulation for epilepsy and depression[1–5]. The therapeutic mechanisms and neuromodulatory effects of electrical stimulation, such as DBS, remain poorly understood, despite its widespread utilization[6,7]. Electrical stimulation of brain tissue may evoke various responses at both the local and global levels, but a comprehensive study of these effects is challenging to undertake using the electrophysiology techniques due to limited data sampling from predefined anatomical brain regions. Functional magnetic resonance imaging (fMRI) represents a powerful tool for mapping brain activity on a whole-brain scale. Simultaneous DBS and fMRI (DBS–fMRI) thus could provide us with valuable insights into brain function and connectivity patterns, as well as modulatory effects and therapeutic mechanisms of functional electrical stimulation in various neurological disorders[8–10].

A major obstacle to combine electrical brain stimulation and fMRI is that many metal electrodes elicit strong magnetic field interference and produce significant artifacts, which obstructs functional and structural mapping of a large volume of brain tissues surrounding the electrodes[11–13]. The main cause for this magnetic field distortion is the mismatch of magnetic susceptibility between the electrodes and water/tissues. The image artifacts or blind spots around the electrodes are particularly severe in fMRI, as it is more susceptible to such effect[14]. This artifact may not affect the identification of long-range responses in brain areas far from the implanted electrode, but local responses at the stimulation site, as well as activation of brain nuclei close to the implanted electrode tracks, will be obstructed, giving rise to incomplete and biased activation pattern mapping[11]. In addition to materials, the electrode size is another important factor to determine MRI artifact size and comprehensiveness of activation pattern mapping. Electrode materials with high charge-injection-capacity and stability are highly desirable to decrease MRI artifact size, as well as to improve stimulation resolution, and to elicit effective and chronically stable brain responses with minimal tissue damage.

In this work, we report on a full and unbiased activation pattern mapping by DBS–fMRI with graphene fiber (GF) microelectrodes in a Parkinson's disease (PD) rat model. Graphene films have been utilized in various kinds of neural electrodes[15–17], due to the unique electrical and optical properties. Here, we show that microelectrodes made from GFs exhibit the combined advantages of high charge-injection-capacity, stimulation stability, and MRI compatibility, which were not achievable by other electrodes. High-frequency DBS targeted at the subthalamic nucleus (STN) with GF electrodes effectively alleviates motor deficits in rats with PD. Moreover, the little-to-no artifact of the GF electrodes in various anatomical and functional MRI images makes all brain regions accessible by fMRI mapping under simultaneous DBS. STN–DBS in PD rats with GF microelectrodes evokes robust blood-oxygenation-level-dependent (BOLD) responses in multiple cortical and subcortical regions along the basal ganglia–thalamocortical network in a frequency-dependent manner. The BOLD responses of some of these regions were not previously detectable with traditional metal electrodes due to their large artifact[11]. The activation pattern indicates that STN–DBS modulates both motor and non-motor pathways, possibly through orthodromic and antidromic signal propagation. We believe that the DBS–fMRI studies with GF electrodes can serve as a powerful platform for translational research investigating the therapeutic mechanisms and modulatory effects of DBS.

Results

GF microelectrode technology. GFs were prepared through a dimension-confined hydrothermal process from aqueous graphite oxide (GO) suspensions[18]. Briefly, a glass pipeline was filled with an aqueous GO suspension. After being baked at 230 °C for 2 h with the pipeline sealed, a GF matching the pipe geometry was produced. The as-prepared GFs had a loose structure, with the graphene sheets randomly oriented. After being air-dried, the GO sheets became densely stacked and aligned parallel to the fiber's main axis, which causes a shrinkage of the fiber diameter and provides GFs with high electrical conductivity, as well as excellent mechanical strength and robustness, which is superior to carbon fibers (CFs), known to have poor fracture resistance and is inconvenient to use[18–20]. The fiber diameter was determined by the pipeline dimension and the GO concentration[18]. A diameter of ~75 μm was used throughout this work. The electrodes made from GFs of this diameter are mechanically strong enough for self-supported implantation into the brain. A typical scanning electron microscopy (SEM) image of a GF shows a porous structure with easily defined individual graphene sheets aligned along the axis (Fig. 1b). The Raman spectrum of the fibers revealed characteristic G and D peaks of the GO (Supplementary Fig. 1)[21]. Electrode fabrication started with insulating individual GFs with Parylene-C film of ~5 μm thickness. A pair of insulated GFs were aligned in parallel and pasted together with glue. After soldering one end of the two GFs onto a custom-made MRI-compatible connector made of high-purity copper used to interface with the stimulation pulse generator, the GFs were mechanically cut to expose the cross sections as electrically active sites, completing the fabrication of a bipolar GF-stimulating microelectrode. The high porosity and roughness of the exposed cross sections of the GF microelectrodes (Fig. 1c) resulted in a large surface area, which is advantageous for achieving high charge-injection-capacity and low impedance[22]. In addition, due to their high mechanical robustness, the GFs can be bent 90° to accommodate the MRI surface coil receiver during MRI scans.

The picture of a typical GF bipolar microelectrode is shown in Fig. 1d. Electrochemical impedance spectroscopy (EIS) measurements resulted in impedance values of 15.1 ± 3.67 kΩ at 1 kHz (mean ± SD, $n = 5$) for GF microelectrodes, which is approximately eight times lower than that of PtIr electrodes of the same diameter (126 ± 53.8 kΩ at 1 kHz, mean ± SD, $n = 5$) (Fig. 1e). The cyclic voltammogram (CV) of GF electrodes exhibited a nearly rectangular shape with no redox peaks observed (Fig. 1g). This suggested that the electrochemical interaction at the GF electrode–electrolyte interface is controlled by capacitive rather than Faradic process. The more resistive phase angle of the GF electrodes compared with PtIr electrodes (Fig. 1f) indicates the reduced imaginary component of impedance as a result of the large electrode surface area and double-layer capacitance[22].

The cathodal charge-storage-capacity (CSC$_c$) was calculated over a potential range of −0.6 to 0.8 V (shaded region in Fig. 1g). The GF microelectrodes showed a CSC$_c$ ~2–3 orders of magnitude higher than that of the PtIr electrodes with the same diameter (889.8 ± 158.0 mC cm^{-2} vs. 2.1 ± 0.7 mC cm^{-2}, mean ± SD, $n = 5$). Voltage transient measurements were carried out to estimate the charge-injection-limit (CIL), which is defined as the maximum charge that can be injected in a current-controlled stimulation pulse without polarizing an electrode beyond the potentials for water reduction or oxidation[22]. The GF microelectrodes have a wide water window of −1.5 to 1.3 V vs. Ag/AgCl (Supplementary Fig. 2). We estimated the CIL of the GF electrodes using −1.5 V as the threshold (see "Methods" section and Supplementary Fig. 3 for details). The GF microelectrodes exhibited a CIL of 10.1 ± 2.25 mC cm^{-2} (mean ± SD, $n = 5$), which is higher than most commonly used electrode materials for
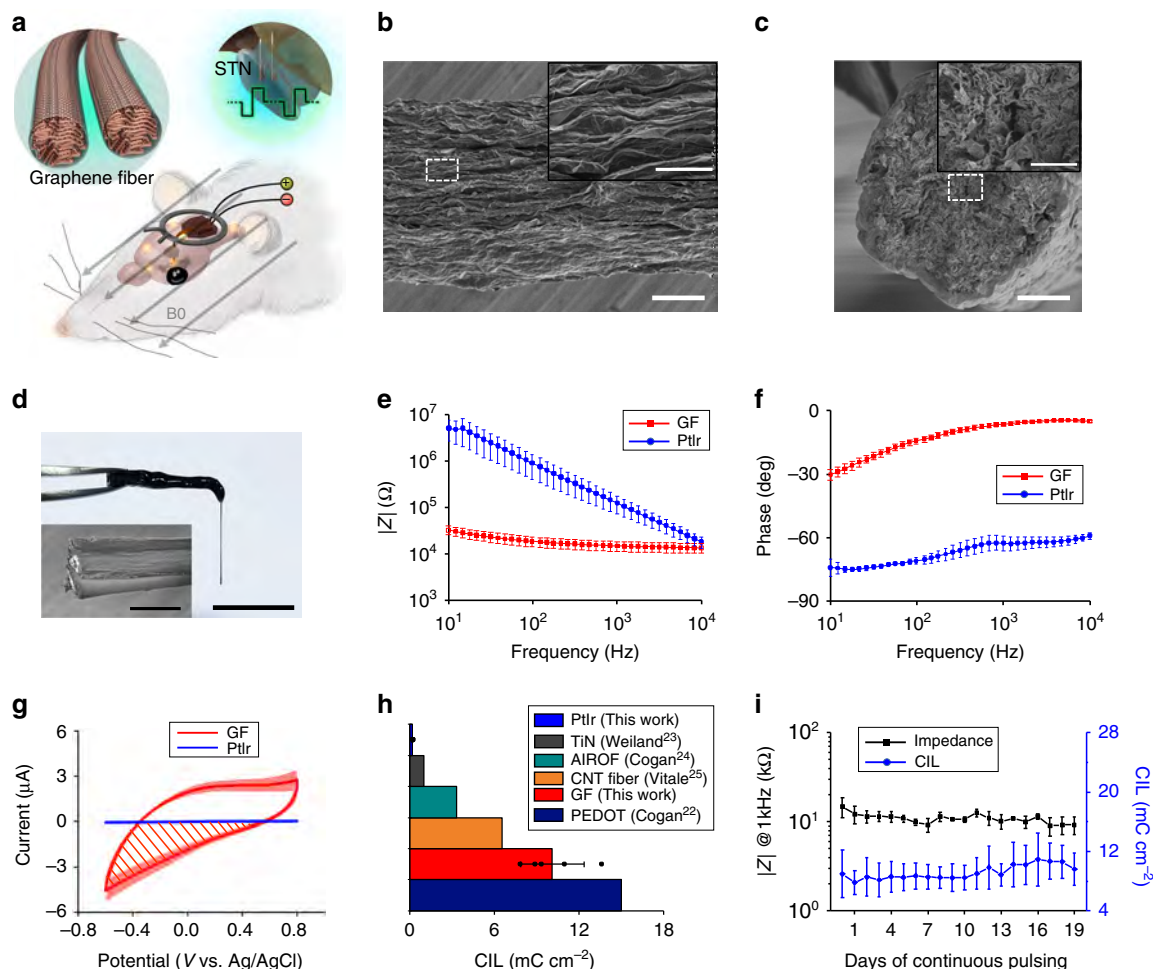
Fig. 1 GF electrodes characterization. a A schematic drawing of the DBS–fMRI study using GF bipolar microelectrodes. **b** A representative SEM image of the axial external surface of a GF fiber. Inset, magnified image of the region in the dashed box. Scale bar, 20 μm; inset, 5 μm. **c** A typical SEM image of the exposed cross section acting as the active stimulating site of a GF electrode. Inset, magnified image of the region in the dashed box. Scale bar, 20 μm; inset, 5 μm. Experiments were repeated five times (for **b**) and three times (for **c**) with similar results. **d** The picture of a GF bipolar microelectrode assembly. Inset, SEM image of the GF bipolar microelectrode tip, showing two GFs (bright core) with each one insulated with Parylene-C film (dark shell). Scale bar, 1 cm; inset, 100 μm. **e**, **f** Impedance modulus and phase of GF and PtIr microelectrodes. **g** Cyclic voltammetry of GF and PtIr electrodes. The time integral of the negative current shown by the shadow region represents the CSC_c. **h** CIL of different electrode materials. "AIROF" means activated iridium oxide film. **i** Stability of GF microelectrodes under continuous overcurrent pulsing at 1 mA current amplitude and 130 Hz frequency (see "Methods" for detailed pulsing parameters). Data represented as mean ± SD in **e**–**i** ($n = 5$ electrodes). Source data are provided as a Source Data file.

neural stimulation, including PtIr, titanium nitride, iridium oxide, and carbon nanotube (CNT) fiber (Fig. 1h)[22–26]. The conducting polymer poly(3,4-ethylenedioxythiophene) PEDOT is reported to possess the highest charge-injection-capacity due to both Faradaic and non-Faradaic mechanisms at the PEDOT–electrolyte interface, and is extensively utilized to coat electrodes to improve their electrochemical performance. The CIL of the GF microelectrodes is slightly lower than that of PEDOT. However, the PEDOT coating on electrodes is reported to suffer from chemical degradation, delamination, and cracks, which makes it incapable of stable chronic stimulation[27,28]. In our test, we also observed a dramatic impedance increase of the PEDOT-coated PtIr electrodes after 16 days of continuous pulsing at an overcurrent condition (a total of 172.8 M current-controlled pulses at 1 mA), indicating degradation of the PEDOT coating (Supplementary Fig. 4). Conversely, the GF electrodes displayed stable impedance and CIL values, even when subjected to more cycles of overcurrent pulsing (a total of 205.2 M pulses, 19 days) (Fig. 1i). Moreover, continuous monitoring of impedance of the GF

electrodes in vivo revealed nearly constant values over time for up to 24 days (Supplementary Fig. 5). These results indicate the high stability of the GF electrodes.

In clinical settings, DBS targeting the selected brain region is now extensively employed for the treatment of various intractable neurological and neuropsychiatric disorders[5]. Efficacious and safe electrical stimulation not only requires high charge-injection-capability but also stability from electrode materials. The GF electrodes show a higher CIL than most available electrode materials, and higher stability than PEDOT-modified metal electrodes. We attribute the high charge-injection-capacity of the GF electrodes to the porous structure and large surface area of their active stimulation sites that are accessible to ions. The high charge-injection-capacity of the GF electrodes allows for the use of small electrodes without the loss of stimulation efficacy, which is not only important to maintain a small MRI artifact size but could also activate a comparatively smaller population of neurons, thus improving the spatial resolution and selectivity of the neural stimulation[20].
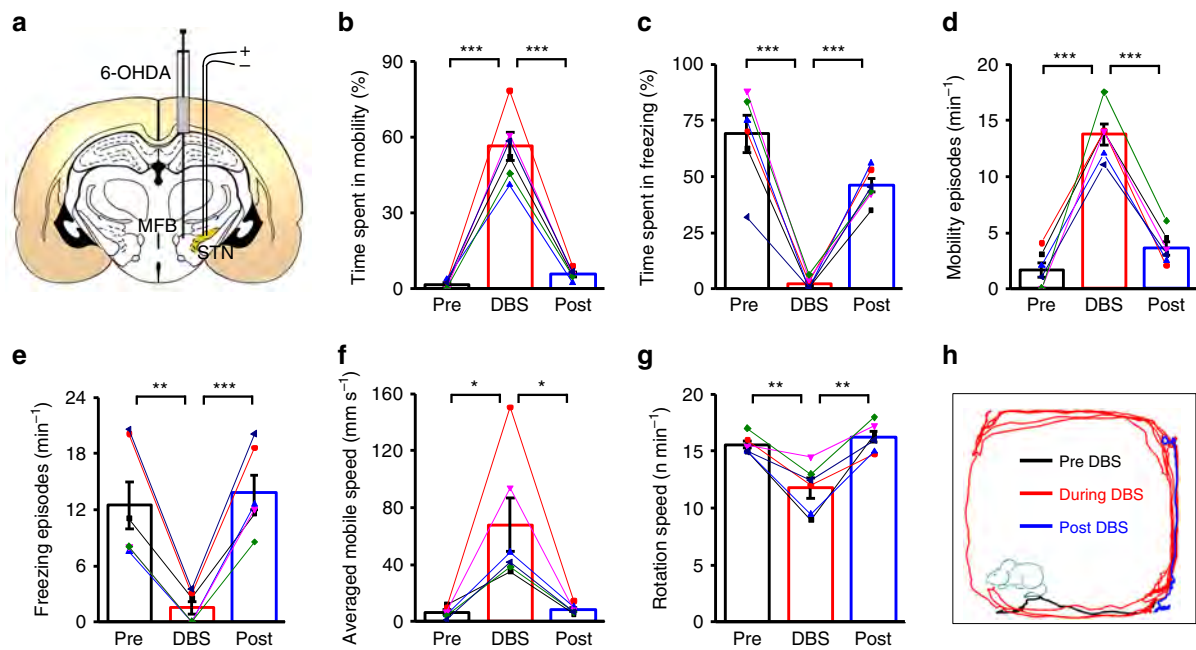
Fig. 2 STN–DBS with GF bipolar electrodes alleviates Parkinsonian motor deficits in 6-OHDA-lesioned rats. a A schematic section showing the placement of the GF bipolar stimulating electrodes at the STN ipsilateral to the 6-OHDA lesion. **b**–**e** Quantification of the locomotor activities of the hemi-Parkinsonian rats, including the time spent in mobility (**b**), time spent in freezing (**c**), mobile episodes per minute (**d**), and freezing episodes per minute (**e**) before (Pre), during (DBS), and after (Post) STN–DBS with GF bipolar electrodes. **f** Analysis of the average mobile speed of the hemi-Parkinsonian rats before (Pre), during (DBS), and after (Post) STN–DBS with GF bipolar electrodes. **g** Analysis of the apomorphine-induced contralateral rotation speed (in number of turns per min) before (Pre), during (DBS), and after (Post) STN–DBS with GF bipolar electrodes. **h** An example of the locomotor activity of a hemi-Parkinsonian rat before (black line, 2 min), during (red line, 2 min), and after (blue line, 2 min) STN–DBS with a GF bipolar electrode. Data from the same animals are connected with lines and distinguished by color in **b**-**g**. Data represented as mean ± SEM ($n = 6$ animals, $*p < 0.05$; $**p < 0.01$, $***p < 0.001$, two-tailed paired t test). Source data are provided as a Source Data file.

STN–DBS in hemi-Parkinsonian rats using GF microelectrodes. We demonstrated the capability of the GF microelectrodes for efficacious DBS in a hemi-Parkinsonian rat model. The hemi-Parkinsonian model was generated by unilateral injection of the neurotoxin 6-hydroxydopamine (6-OHDA) into the medial forebrain bundle (MFB) of the adult rat brains, resulting in a loss of dopamine neurons, which models Parkinson's disease on the contralateral side of the body[29]. Successful generation of the hemi-Parkinsonian rat model was confirmed by the apomorphine-induced contralateral rotation test[30]. Bipolar GF microelectrodes were implanted in the ipsilateral STN, a common DBS target for the treatment of Parkinson's disease[5,29] (Fig. 2a). For each subject, electrode tip placements within the STN were verified by T_2-weighted rapid acquisition with relaxation enhancement (RARE) anatomical MRI images acquired immediately after the implantation, and haematoxylin eosin (H&E) staining of the coronal brain sections at the end of the study (Supplementary Fig. 6). Those with electrode tips outside of STN were discarded from the study. The artifact-free property of the GF electrodes, as is described in the following section, could enable more precise in vivo localization and placement verification of the implanted electrodes.

High-frequency stimulation consisting of 130 Hz square constant current pulses (biphasic, symmetric, charge-balanced pulses at 50–200 μA and 60 μs width per phase) was applied to the GF bipolar microelectrodes implanted in rats with PD. Open-field tests showed that these rats ($n = 6$) spent 1.8 ± 0.6% of their time mobile, and 69.0 ± 8.3% of their time freezing. When STN–DBS was turned on, these rats spent more time mobile as 56.4 ± 5.4% and less time freezing as 2.3 ± 1.0% (both $p < 0.001$ compared with DBS off) (Fig. 2b, c). The improved mobility proved the therapeutic efficacy of STN–DBS with GF electrodes.

When STN–DBS was turned off, the time spent mobile and freezing immediately changed back to 5.6 ± 0.9% ($p < 0.001$ compared with DBS on) and 46.2 ± 3.2% ($p < 0.001$ compared with DBS on), respectively, indicating the disappearance of the above beneficial effects. The improved mobility of these rats in the open arena by STN–DBS with GF electrodes was also confirmed by the change in the episode number spent in mobility and freezing (Fig. 2d, e). Bradykinesia symptoms were also alleviated by STN–DBS with GF electrodes, as indicated by the increase of mobile speed from 6.3 ± 1.6 mm s^{-1} to 67.9 ± 18.7 mm s^{-1} ($p < 0.05$ compared with DBS off). Mobile speed changed back to 8.5 ± 1.3 mm s^{-1} ($p < 0.05$ compared with DBS on) when STN–DBS was turned off (Fig. 2f). Furthermore, in the apomorphine-induced contralateral rotation test, a statistically significant reduction of rotation speed was observed during STN–DBS with the GF electrodes (Fig. 2g). An example of the locomotor activity of a hemi-Parkinsonian rat before, during, and after STN–DBS with GF electrodes is shown in Fig. 2h. These results confirmed the therapeutic efficacy of the DBS with GF microelectrodes in activating the STN pathway and alleviating motor deficits of the hemi-Parkinsonian animals.

In vivo assessment of MRI compatibility. We evaluated the MRI artifacts of the GF microelectrodes in a high-field 9.4 T MRI scanner and compared them to those made of PtIr, which is the material most commonly used in clinical neural stimulation devices[31,32]. The same GF and PtIr microwire diameter (75 μm) was used. The electrodes were implanted in the STN of the rat brains (Fig. 3a). A canny edge detector was used to detect the artifact edge, from which the artifact size was measured (Supplementary Fig. 7). The GF bipolar electrodes showed an artifact
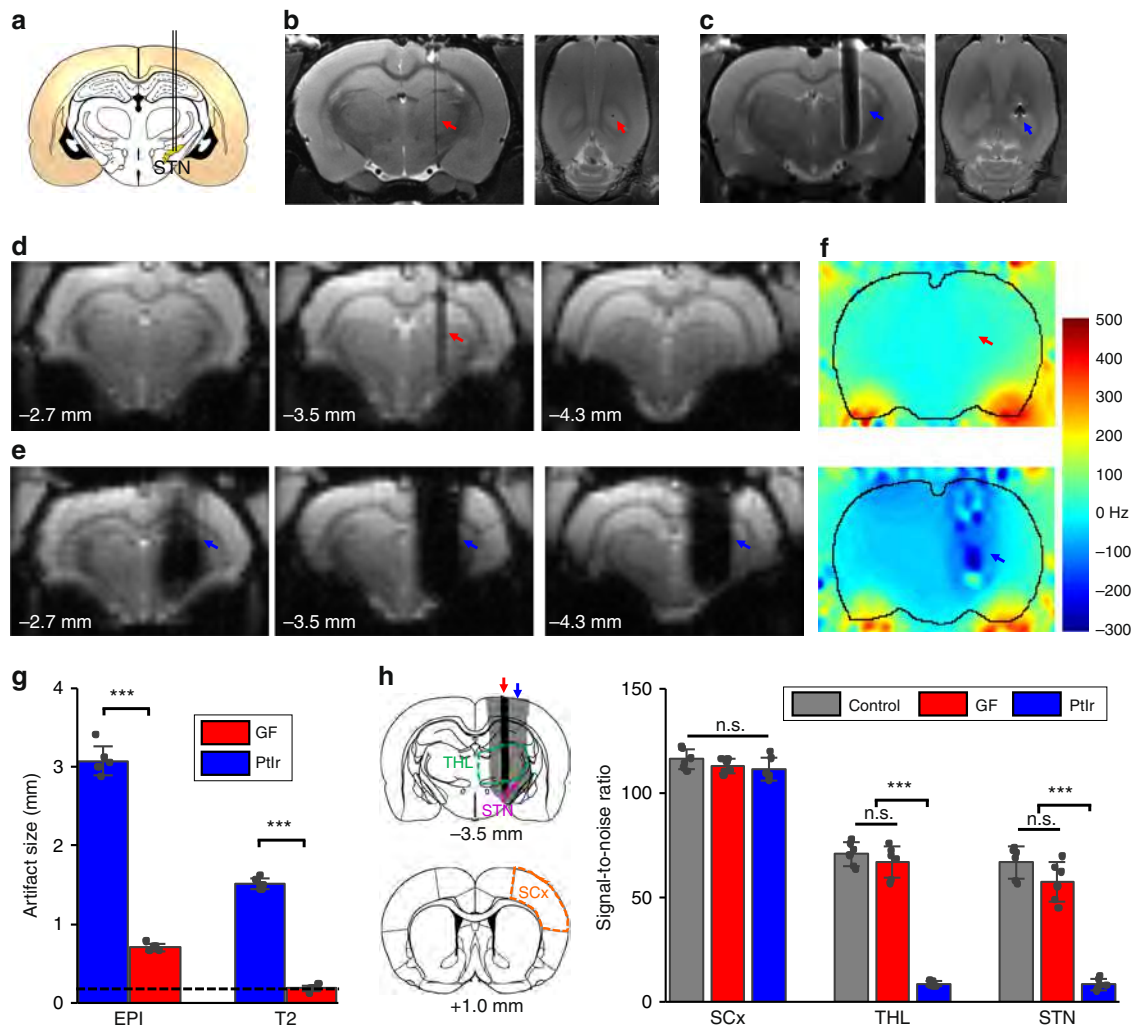
Fig. 3 In vivo assessment of MRI artifact. a A schematic section showing the placement of the electrodes at the STN of rat brains in MRI artifact studies. Each bipolar electrode was composed of a pair of GFs or PtIr wires (75 μm diameter) insulated with ~5-μm-thick Parylene. Thus, the actual size in the medial–lateral direction was ~170 μm. **b**, **c** Representative coronal (left) and horizontal (right) sections of the T$_2$ MRI images of rat brains implanted with a GF (**b**) and PtIr (**c**) bipolar microelectrode, through the position of the implants. **d**, **e** Representative three serial coronal scans from rostral (left) to caudal (right) of EPI images from rat brains implanted with a GF (**d**) and PtIr (**e**) bipolar microelectrode, with the middle images depicting the electrode implant sites. The numbers in each image denote the relative distance from bregma. **f** B0 distortion maps observed in rats implanted with a GF (upper) and PtIr (lower) bipolar electrode. Red and blue arrows in **b**–**f** point to the GF and PtIr implants, respectively. **g** MRI artifact size of the GF and PtIr bipolar electrodes. The black dashed line denotes the actual size of the bipolar electrodes. Data represented as mean ± SD ($n = 6$ electrodes, ***$p < 0.001$, two-tailed unpaired t test). **h** SNR of the EPI signal in several brain areas in control rats without any implant, and rats implanted with GF and PtIr bipolar electrodes at the STN. The ROIs of the three tested brain nuclei were defined from single slices, as indicated in the left reference diagrams. The top diagram represents the implantation plane, and the red and blue arrows point to the EPI artifact outline of the GF and PtIr bipolar electrodes, respectively. The numbers below the diagrams denote their relative distance from bregma. Somatosensory cortex (SCx) = orange; thalamus (THL) = green; STN = purple. Data represented as mean ± SD ($n = 6$ samples, n.s.: not significant; ***$p < 0.001$, one-way ANOVA tests with Tukey post hoc analysis). Source data are provided as a Source Data file.

with a size of 0.18 ± 0.04 mm ($n = 6$), comparable with their actual size of ~0.17 mm and much smaller than that from the PtIr bipolar electrodes (1.51 ± 0.07 mm, $n = 6$) in the T$_2$ anatomical images (Fig. 3b, c, g). Because the echo-planar imaging (EPI) sequence, commonly used in fMRI, is more sensitive to the susceptibility mismatch, both electrodes exhibited larger artifacts in the EPI images (Fig. 3d, e) than the anatomical T$_2$ images, which makes the fMRI particularly vulnerable to influences from field distortion caused by the implants. The GF bipolar electrodes displayed an artifact of 0.70 ± 0.05 mm ($n = 6$) in the EPI images, while the PtIr bipolar electrodes showed a much more pronounced artifact with sizes of 3.08 ± 0.18 mm ($n = 6$). Such a large volume of signal dropout clearly obstructed a significant

portion of the total rat brain area, resulting in a loss of functional response visualization during MRI scans (Fig. 3e). The large artifact of the PtIr electrodes was also manifested in serial slices from rostral (left) to caudal (right) of the EPI images, in which a total of six slices showed the artifact; whereas, for the GF electrodes, their artifact was visible in one slice and was slightly shown in one adjacent slice (Fig. 3d, e; Supplementary Fig. 8). In addition, we performed MRI scans on rat brains implanted with the GF bipolar electrodes under the application of electrical stimulation pulses, and no difference was observed in electrode artifact size for either T$_2$-weighted or EPI images (Supplementary Fig. 9), indicating that the application of the electrical pulses will not induce additional artifacts.

We outlined and overlaid the EPI artifacts of both electrodes on reference diagrams showing the coronal section of the rat atlas (Supplementary Fig. 8). It can be seen that a significant number of brain nuclei were overlapped with the blind regions surrounding the PtIr bipolar electrodes (a full list of these nuclei can be found in Supplementary Table 1), with some of them almost entirely blocked by the artifact. These affected brain regions will either be inaccessible or give a low response amplitude in fMRI mapping, leading to an incomplete and biased activation pattern map. Distinctly, for GF bipolar electrodes, no additional brain nuclei—except for those overlapped with the actual electrode tracks—were affected. All of the regions affected by the GF bipolar electrode artifact still had significant portions outside of the artifact, which made them all accessible to fMRI. EPI signal-to-noise ratios (SNRs) of some examined basal ganglia–thalamocortical regions, including the somatosensory cortex, thalamus, and even the target STN in brains implanted with GF bipolar electrodes, showed no significant difference compared with those in control animals with no implants. In contrast, EPI SNRs from brains implanted with PtIr bipolar electrodes were significantly attenuated for the thalamus and STN (Fig. 3h). No significant influence was found in the somatosensory cortex due to its large distance from the implants. Furthermore, B0 maps of rat brains implanted with the GF bipolar electrodes did not reveal any detectable field distortions around the implant, differing from the PtIr electrode implants which caused obvious and extensive B0 field variation around the implants (Fig. 3f). These quantitative results demonstrated that the GF electrodes caused minimal interference to the magnetic field, and their presence would not cause significant attenuation in fMRI signals, thus enabling a full and unbiased mapping of the activation pattern under DBS–fMRI studies. Such advantage is critical for exploring the neuromodulatory effects and mechanisms of DBS therapies. It was noted that the GF electrodes on one-segment EPI images showed comparable artifact size as that on four-segment EPI images (Supplementary Fig. 10), therefore ensuring high MRI compatibility and full activation pattern mapping capability for most fMRI studies.

Tungsten wire and carbon fiber (CF) electrodes were also used previously in simultaneous DBS–fMRI studies[9,13]. Bipolar electrodes made from 75-µm diameter tungsten wires showed EPI artifact of 2.14 ± 0.24 mm under 9.4T MRI (Supplementary Fig. 11), which is slightly smaller than that from PtIr electrodes of the same size (3.08 ± 0.18 mm), and still significantly larger than that from GF electrodes of the same size (0.70 ± 0.05 mm). CF electrodes of a similar size exhibited an EPI artifact size of 0.85 ± 0.14 mm, which was comparable with that from GF electrodes (Supplementary Fig. 11). However, we found that CF electrodes had a very low charge-injection-capacity (CIL of 0.05 mC cm^{-2} vs. 10.1 mC cm^{-2} for GF electrodes), which is consistent with previous reports[20]. Due to this very low charge-injection-capacity, a much larger electrode size is required to inject sufficient charge for DBS to elicit the desired physiological response without damages to tissues or electrodes (Supplementary Fig. 12), which would in turn increase artifact sizes for DBS–fMRI. Supplementary Table 2 lists the measured CIL, and calculated minimum wire diameters d_{min} for electrodes required to inject 200-µA current pulses without polarizing electrode potential beyond the water window, for various materials, including GF, CF, PtIr, tungsten, and graphene-encapsulated copper (G–Cu)[33]. EPI images from rat brains implanted with various bipolar electrodes made of wires with this minimum wire diameter d_{min} are shown in Supplementary Fig. 13. Under the prerequisite of safe charge injection without electrode potential excursion beyond the water window, the CF electrodes led to a ~2× EPI artifact size compared with the GF electrodes used in our study (with diameter of 75 µm,

Supplementary Fig. 14), which caused significantly reduced SNR for some nuclei close to the electrodes, including thalamus and STN (Supplementary Fig. 14). Among all tested materials, GF was the only one that did not cause signal loss for either thalamus or STN (Supplementary Fig. 14), thus possessing the capability for full activation pattern mapping. In addition, the large size of the CF bipolar electrodes (~586 µm, Supplementary Figs. 12, 13 and Supplementary Table 2) would also decrease stimulation selectivity, as well as lead to severe acute tissue damages and sustained chronic inflammatory responses[20,34], all of which are undesirable for neural electrical modulation.

DBS–fMRI studies. The STN–DBS using GF bipolar electrodes in hemi-Parkinsonian rats evoked significant and frequency-dependent positive BOLD responses in the ipsilateral basal ganglia–thalamocortical network, including multiple cortical and subcortical regions (Fig. 4). Individual BOLD activation maps from each rat are included in Supplementary Fig. 15. No significantly modulated voxels were observed in the contralateral hemisphere. DBS–fMRI measurements of the same rats immediately after sacrifice revealed no BOLD responses (Supplementary Fig. 16). This suggests that the BOLD responses that we observed here reflected brain activities, rather than artifact caused from the electrical stimulation. In addition, the time courses of several anatomical regions of interest (ROIs) were calculated for each stimulation frequency, which demonstrated clear BOLD signal changes that were time-locked to the stimulation pulse blocks (Fig. 5). The maximal amplitude of the BOLD signals was observed at 100 and 130 Hz, which are the therapeutic effective frequencies used in clinical settings. Of all of the regions examined, the DBS target STN showed the largest percentage of BOLD changes (~$5.81 \pm 0.36\%$ at 100 Hz, and $6.12 \pm 0.38\%$ at 130 Hz DBS, $n = 24$). Among the examined cortical regions, the motor cortex exhibited the largest BOLD signal changes ($3.86 \pm 0.36\%$ at 100 Hz, $3.50 \pm 0.21\%$ at 130 Hz DBS, $n = 24$), and the somatosensory cortex showed the lowest responses ($1.28 \pm 0.29\%$ at 100 Hz, $0.84 \pm 0.14\%$ at 130 Hz DBS, $n = 24$). A close examination of the signal time traces revealed a clear "double peak" feature of the BOLD signal in certain regions, including the motor cortex, somatosensory cortex, cingulate cortex, and STN (Fig. 5), possibly due to the involvement of two different circuitries or a delayed neurotransmission effect[10]. It is worth noting that, for 10 Hz STN–DBS, the three cortex and caudate putamen regions first produced a small negative BOLD signal followed by a positive BOLD response during the stimulation epoch, a feature that is distinct from other regions and other frequencies. This suggests the possibility of a biphasic neuronal response[35]. Importantly, the BOLD activation within STN, GPi, GPe, caudate putamen, and motor cortices exhibited significant correlations with the mobile speed increase of the hemi-Parkinsonian rats under 130 Hz DBS ($p < 0.05$, Fig. 6).

Discussion
Simultaneous DBS and fMRI serves as a powerful tool for examining the modulatory effects of electrical stimulation on brain network activity in vivo, which is important to understand the underlying therapeutic mechanism of DBS. The little-to-no artifact of the GF electrodes makes the fMRI mapping accessible to all brain regions, thus providing a way for full and unbiased activation pattern mapping under DBS, especially in small animal studies. Previous work on DBS–fMRI at the STN target in rats using conventional stimulating electrodes, such as PtIr, failed to demonstrate reliable BOLD responses within regions in the STN, internal and external globus pallidus (GPi and GPe), and thalamic nuclei, due to the electrode artifact[11]. Even for human DBS–fMRI
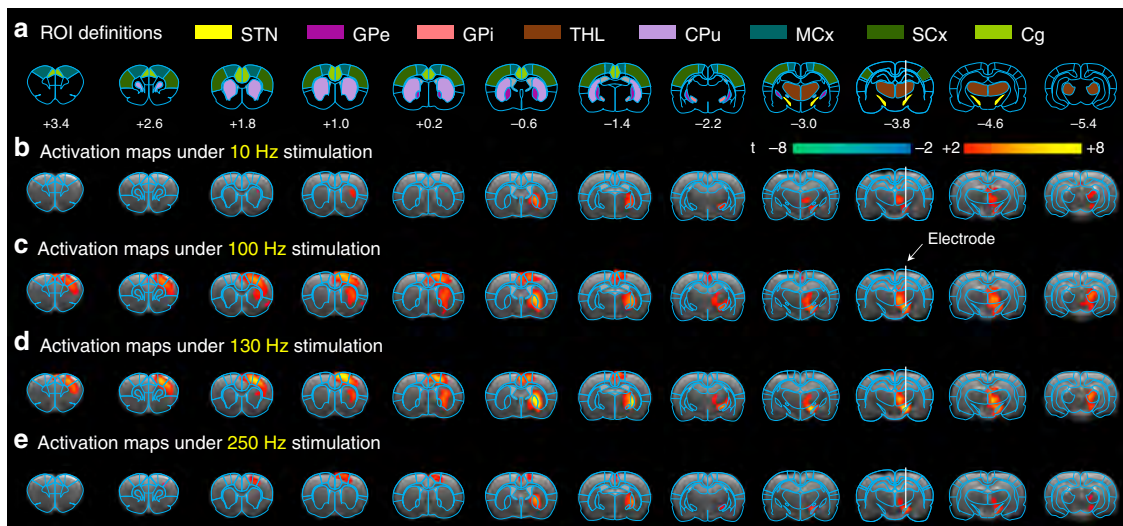
Fig. 4 BOLD activation maps evoked by STN–DBS with GF electrodes in PD rats. Four stimulation frequencies were tested as marked in each panel. The BOLD activation maps are overlaid onto averaged anatomical images. Numbers below slices denote relative distance from bregma (in mm). The same set of distance numbers applies to the slices in **b–e**. Color bar denotes t-score values obtained by GLM analyses, with a significance threshold of uncorrected $p < 0.001$. All data are group averaged, $n = 24$ scans from eight rats. STN subthalamic nucleus, GPe external globus pallidus, GPi internal globus pallidus, THL thalamus, CPu caudate putamen, MCx motor cortex, SCx somatosensory cortex, Cg cingulate cortex.

investigations, it was reported that the electrode artifact could lead to regional bias in activation pattern mapping[36,37].

With the utilization of GF electrodes, we observed that STN–DBS in hemi-Parkinsonian rats modulated the activity of the basal ganglia–thalamocortical network in a frequency-dependent manner. Robust positive BOLD responses to STN–DBS were observed in both distant and local areas, including the motor cortex, somatosensory cortex, cingulate cortex, GPi, GPe, caudate putamen, thalamus, and even the DBS target of STN. This activation pattern indicates the modulation of both motor and non-motor pathways by STN–DBS. The strong positive activation of the ipsilateral motor cortex was consistent with the therapeutic motor effects of DBS. Prior work demonstrated direct antidromic activation of primary motor cortex neurons during STN–DBS using electrophysiological studies[30]. Optogenetic research showed that the therapeutic motor effects were from antidromic stimulation of the afferent hyperdirect pathway from the cortex to STN, rather than from orthodromic projections to GPi[29]. The significant correlations of BOLD activation within STN, GPi, GPe, caudate putamen, and motor cortices with the mobile speed increase of the hemi-Parkinsonian rats observed here indicated that the alleviation of PD symptom under STN–DBS was related to the modulation of the basal ganglia. These results suggest that both orthodromic stimulation of the feed-forward thalamocortical circuit and antidromic activation of motor cortical afferents might underlie the therapeutic mechanism of STN–DBS.

The activation in the somatosensory and cingulate cortex indicate the involvement of non-motor circuits which may be related to the sensory and limbic effects observed clinically for STN–DBS, particularly the effects on pain and mood[38,39]. An early human DBS–fMRI case study reported that, in one patient, depressive dysphoria was induced by right-side DBS accompanied by positive BOLD activation in the superior prefrontal cortex, anterior cingulate, and anterior thalamus, with the implanted electrode marginally superior and lateral to the intended STN target[40]. Another investigation showed that stimulation applied at the anteromedial STN contact and the contact immediately dorsal to it consistently produced a hypomanic state, in addition to an alleviation of motor symptoms. Their

positron emission tomography (PET) study revealed the activation of limbic and association cortex, including areas of the anterior cingulate gyrus and ventral anterior nucleus of the thalamus[41]. These side effects are understandable because STN is known to be involved in multiple circuits connecting cortical regions to the basal ganglia that regulate motor, cognitive, and emotional behavior[42]. These studies also showed that the exact position of the stimulation sites within different STN sub-regions might affect both the motor and non-motor outcome of DBS. We believe that, for future human applications, the artifact-free property of the GF electrodes under anatomical MRI and their small size would enable more precise MR-guided electrode implantation to minimize location inaccuracies, thus assisting to obtain optimal clinical benefits and alleviate adverse side effects from DBS.

The activation of caudate putamen, thalamus, and globus pallidus were also observed in previous human and animal DBS–fMRI studies. Greater activation in caudate putamen was reported in normal anesthetized pigs when using STN as a DBS target than using a GPi target, which might help to understand the fact that more patients were able to reduce medication dosage using STN–DBS than using GPi-DBS[43]. In a human pilot study, it was reported that the stimulation was effective over a longer period of time for patients with BOLD signal activation observed in the globus pallidus than those exhibiting no activation in the pallidum[44]. While determination of how the activation of various brain areas correlates with the therapeutic effects of DBS warrants additional research, we believe that DBS–fMRI may act as an effective paradigm in rating the clinical effect of the procedure. One limitation of the present work is that the difference in states between behavioral testing (awake) and fMRI (anesthetized) might limit our ability to detect all potential neural correlates of the DBS therapeutic effect. For future studies, applications of awake rat fMRI[45] would be beneficial to provide more detailed clues of circuitry mechanisms of DBS therapies.

Our work demonstrates the advantage of GF electrodes in simultaneous DBS and fMRI studies. We believe that the little-to-no artifact of the GF electrodes is attributable to the close magnetic susceptibility between the GFs and water/tissues. It was observed that artifacts from all electrodes were much more
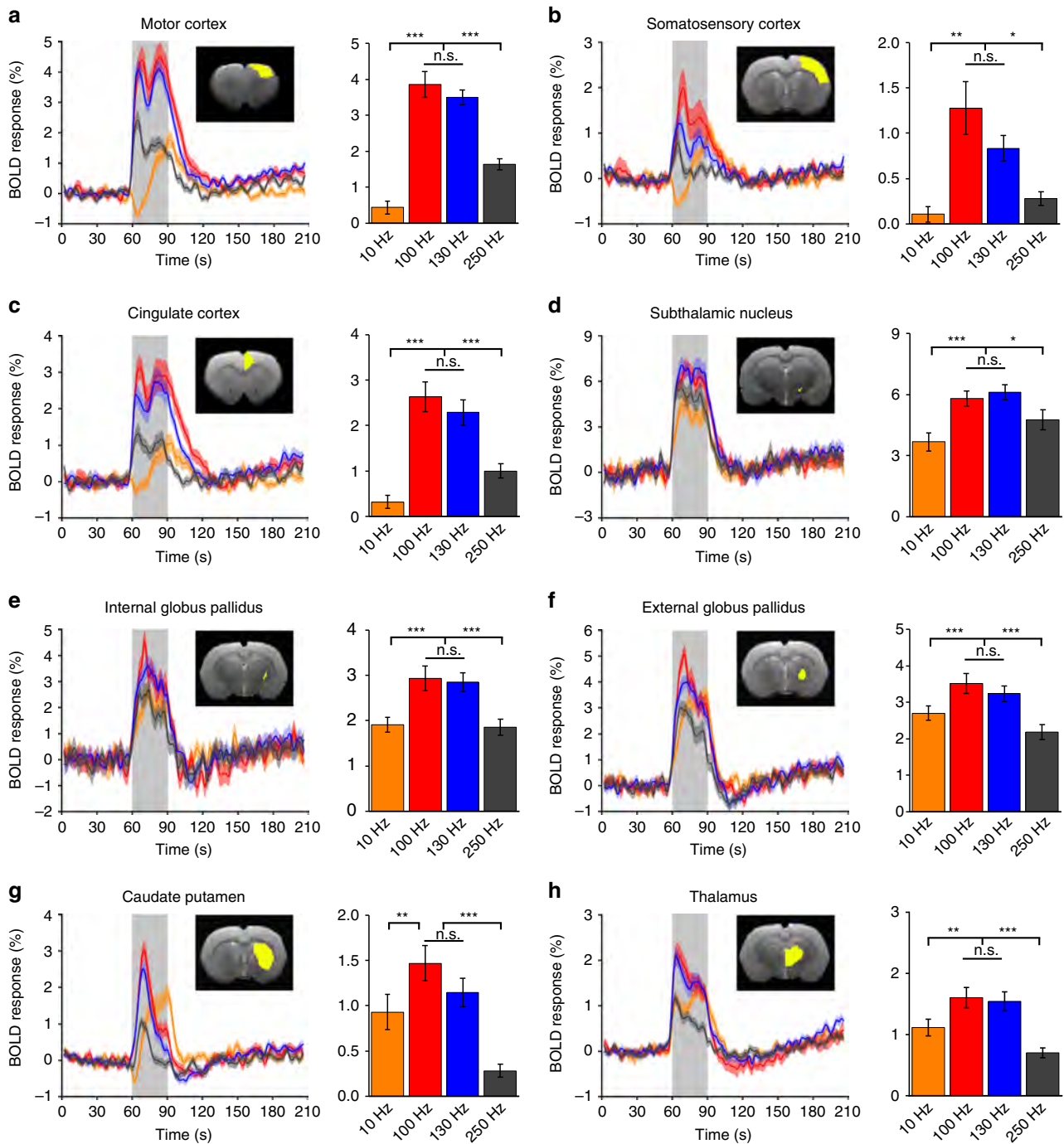
Fig. 5 BOLD signal time series at selected anatomically defined ROIs evoked by STN–DBS with GF electrodes in PD rats. Percent BOLD response over time at each ROI is shown for multiple stimulation frequencies (orange, 10 Hz; red, 100 Hz; blue, 130 Hz; gray, 250 Hz). The stimulation epoch is indicated by a gray-shaded band. The solid lines show the average signal, and the shaded regions represent the SEM, $n = 24$ from eight rats. The bar graphs display the average percent changes in BOLD amplitude during the stimulation period. Data represented as mean ± SEM ($n = 24$ scans from eight rats, n.s.: not significant; $*p < 0.05$; $**p < 0.01$; $***p < 0.001$, one-way repeated measures ANOVA tests with Tukey post hoc analysis). The inserts depict representative slice examples for each predefined ROI (note that most ROIs encompassed multiple slices). All ROIs are ipsilateral to the DBS hemisphere. Source data are provided as a Source Data file.

evident on the functional images (T_2^*-weighted gradient-echo EPI images) compared with the structural images (T_2-weighted RARE images) (Fig. 3b–e), which indicates that the artifacts are primarily resultant from magnetic field inhomogeneity as the gradient-echo EPI images are more sensitive to magnetic susceptibility inhomogeneity than the T_2-weighted RARE images[46]. The PtIr electrodes severely degraded MRI image quality with a

relatively large paramagnetic susceptibility of ~231 ppm, and $\Delta\chi \approx 240$ ppm with respect to that of water ($\chi = -9.05$ ppm)[47]. The tungsten electrodes of the same size showed less artifact than PtIr electrodes with magnetic susceptibility of ~77.2 ppm, and $\Delta\chi \approx 86$ ppm with respect to that of water[14]. Although the precise value of the overall magnetic susceptibility of the GFs is not yet available, their little-to-no artifact suggests a close value to that of
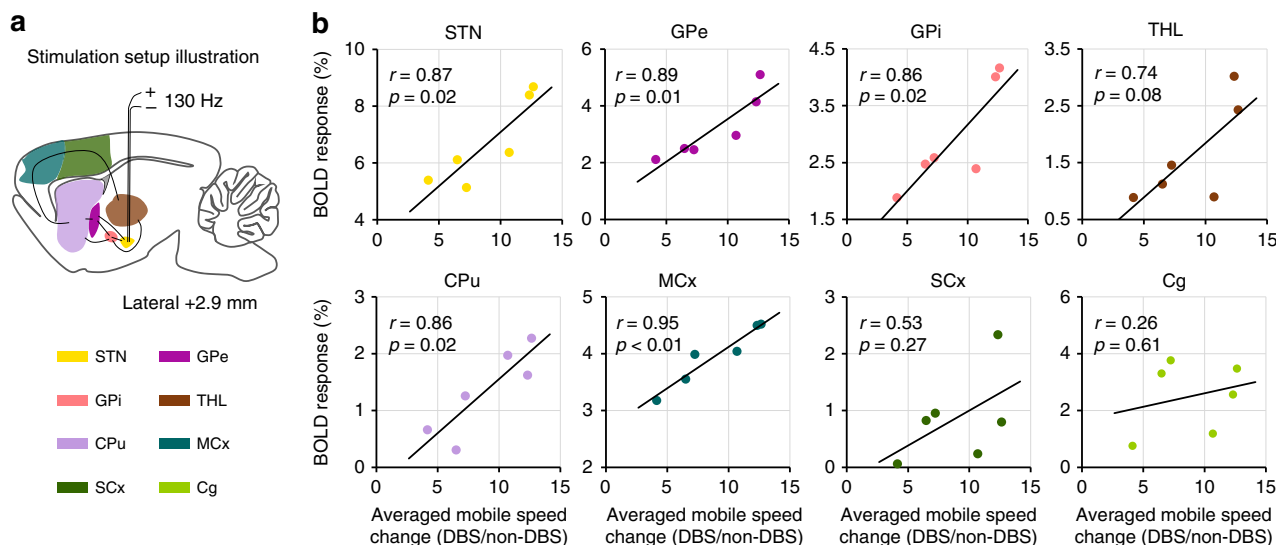
Fig. 6 Correlation between BOLD responses and mobile speed change. a A schematic section showing the placement of the stimulating electrode at STN. **b** Scatter plot between regional BOLD responses and averaged mobile speed change under 130 Hz STN–DBS. The averaged mobile speed change is defined as averaged mobile speed under DBS divided by that without DBS (non-DBS), which is the average of pre- and post-DBS values. The Pearson's correlation coefficient r between mobile speed increase and BOLD responses across rats was calculated for each ROI. Source data are provided as a Source Data file.

water. Eddy currents can be induced in implantable electrodes by gradient switching and RF field, which might contribute to the MRI artifact. However, because the area receiving the magnetic flux is small as a result of small electrode diameter, the induced eddy currents in GFs used here were small and decayed rapidly (see Supplementary Information for details), which makes the eddy current origin negligible for the MRI artifact[26]. Furthermore, the interactions between the MRI environment and conductive implants pose risks of electrode heating and tissue damage[48]. The H&E staining results showed no obvious tissue damage around the electrode tips after the DBS–fMRI studies under the conditions used here. This indicates that, under strict guidelines, the DBS–fMRI can be safe for future human applications.

In conclusion, our DBS–fMRI study using GF electrode technology revealed a full activation pattern under STN–DBS in Parkinsonian rats, which is not achievable by other metal or CF electrodes. The DBS–fMRI studies with the GF electrodes are widely applicable to other targets or neurological conditions. With the unique capability for full and unbiased mapping of the entire circuit and network connectivity without obstructing brain nuclei, future DBS–fMRI studies with the GF electrodes at different targets and with varied stimulation frequency and strength could provide important insights into brain circuitries and network connections, as well as the therapeutic mechanisms underlying various DBS therapies.

Methods

Microelectrode fabrication and characterization. Graphene fibers (GFs) were prepared through a one-step dimensionally confined hydrothermal process using suspensions of graphene oxide (GO) (monolayer, thickness: 0.8–1.2 nm; sheet diameter: 0.5–5 μm; #XF002-2, Nanjing/Jiangsu XFNANO Materials Technology, China). In a typical preparation, an 8 mg mL^{-1} aqueous GO suspension was injected into a glass pipeline with a 0.9 mm inner diameter using a syringe. After being baked at 230 °C for 2 h with the two ends of the pipeline sealed, a GF matching the pipe geometry was produced. This preformed GF was then released from the pipeline by flow of N_2 and dried in air. The dried GF had a reduction in diameter to ~75 μm due to water loss and drying-induced alignment of the GO sheets. Measurements of the Young's modulus of these GFs using a single-column testing instrument (Instron 5843, USA) gave an average Young's modulus of 2–3 GPa. The diameter of 75 μm was used in all studies in this work. The GF samples were characterized by scanning electron microscopy (Hitachi S-4800 operated at 1–2 kV acceleration voltage, Japan) and Raman spectroscopy

(Jobin-Yvon Horiba LabRAM HR-800, 514 nm, ×100 objective, France, LabSpec Version 5.36.11). Parylene-C film of 5 μm thickness was deposited onto the GFs in a homemade low-pressure coating system. To make a bipolar GF-stimulating electrode, a pair of GFs with Parylene-C insulation were aligned in parallel and mechanically pasted together with glue. One end of two GFs was soldered onto a custom-made MR compatible female header connector made of high-purity copper. A sharp blade was used to cut the GFs to the desired length and expose the cross sections of the pair of GFs as the active stimulating sites. The same method described above was used to fabricate other bipolar electrodes from PtIr microwires (#767600, A-M Systems, USA), tungsten microwires (#797550, A-M Systems, USA), CFs and G–Cu wires. In all, 1 K tow carbon fiber (#CF701, The Composites Store, USA) was split to produce bundles with desired diameters. G–Cu wires were made by chemical vapor deposition of graphene on copper wires[33].

All electrochemical measurements were performed in 1× phosphate buffered saline (PBS) with pH 7.4 at room temperature. Electrochemical impedance spectroscopy (EIS) and cyclic voltammetry (CV) were done using a CHI660e electrochemical workstation (version 15.08, CH Instruments, USA). A three-electrode configuration was used, with the tested sample as the working electrode, an Ag/AgCl electrode as the reference electrode, and a large surface area platinum as the counter electrode. CV tests were performed by sweeping the potential of the electrode at a scan rate of 50 mV s^{-1}. Each sample was swept for two cycles, and the cathodic charge-storage-capacity (CSCc) was calculated as the time integral of the cathodic current recorded over a potential range of −0.6 to 0.8 V in the second cycle. For water window testing, CV was performed between the voltage limits of −1.8 to 1.8 V at a scan rate of 1 mV s^{-1}. The water window of the GF electrodes was determined as the water oxidation and reduction potential obtained from CV measurements, where a steep increase in current was observed (Supplementary Fig. 2).

For voltage transient experiments, a three-electrode cell (the same as above) was used. Biphasic, symmetric, and charge-balanced current pulses of 60 μs duration (Supplementary Fig. 3) were delivered to the tested sample at a frequency of 130 Hz with a stimulator (Model 2100, A-M Systems, USA). Voltage transients under the current pulses were recorded with an oscilloscope, and the negative potential excursion (V_{exc}) was calculated by subtracting the initial access voltage (V_{acc}) due to solution resistance from the total voltage (V_{tot}, Supplementary Fig. 3). The charge-injection-limit was calculated by multiplying the current amplitude and pulse duration at which V_{exc} reaches the water reduction limit (−1.5 and −0.6 V for GF electrodes and PtIr electrodes, respectively), divided by the geometric surface area of the electrodes.

Stability testing under continuous overcurrent pulsing was performed by immersing the GF electrodes in a cell filled with 1× PBS, pH 7.4 at room temperature. A two-electrode configuration was used with the GF electrode as the working electrode, and a large surface area Pt foil electrode used as the return and reference electrode. The cell was sealed in order to avoid evaporation of the electrolyte, and thus keep the solution impedance constant. The electrodes were tested prior to the beginning of the stability experiments (day 0), and on each of the following days after ~23 h of continuous stimulation (10.8 M pulses day^{-1}, 130 Hz, biphasic, symmetric, and charge-balanced current pulses of 60 μs duration) at 1 mA amplitude. This pulse amplitude is larger than what is commonly used in DBS for

PD (50–300 μA). The experiment was concluded after 19 days of continuous stimulation.

The same protocol described above was used to test the stability of the PEDOT-poly (styrene sulfonate) (PSS) deposited on the electrically active sites of the PtIr microelectrodes. For PEDOT-PSS deposition, electrolyte consisting of 0.01 M 3,4-ethylenedioxylthiophene (EDOT) (Sigma-Aldrich, USA) and 0.1 M sodium PSS (Sigma-Aldrich, USA) aqueous solution was used. The electrochemically polymerized reaction was performed in a three-electrode cell under galvanostatic conditions. A platinum foil was used as the counter electrode, and an Ag/AgCl electrode was used as the reference electrode. In the galvanostatic mode, the polymerization was carried out under a constant current of 22 nA for 30 min. After PEDOT-PSS deposition, samples were kept immersed in deionized water for 2 h to remove impurities and excess EDOT. The electrodes were tested before the PEDOT-PSS deposition and on the same day of the PEDOT-PSS deposition (day 0).

Animal surgery. Adult male Sprague-Dawley rats weighing 250–280 g (Charles River Laboratories, China) were used throughout this study. Our procedures for handling the animals complied with the Beijing Administration Rules of Laboratory Animals and the National Standards of Laboratory Animal Requirements of Environment and Housing Facilities (GB 14925−2010), and were approved by the Institutional Animal Care and Use Committee of Peking University. For surgery, the rats were anesthetized using constant 2–2.5% isoflurane in medical-grade oxygen. Rats were secured in a stereotactic apparatus (Lab Standard Stereotaxic Instrument, Stoelting, USA) throughout the procedure. The hemi-Parkinsonian rats were generated by unilateral injection of 6-hydroxydopamine (6-OHDA, 1.6 μL, 5 mg mL^{-1} dissolved in 0.9% saline; Sigma-Aldrich, USA) into the medial forebrain bundle (MFB) (AP: −4.4 mm; ML: −1.1 mm; DV: 8.0 mm from dura). After a 2-w recovery period, apomorphine-induced contralateral rotation behavior was tested to confirm whether the hemi-Parkinsonian rat model was successfully induced. Each rat was injected with apomorphine (0.5 mg kg^{-1}, Sigma-Aldrich, USA) subcutaneously. After 15 min, the contralateral rotational number was counted for 5 min, and those exhibiting a contralateral rotation speed exceeding 15 turns min^{-1} were considered as successful based on previous similar studies and selected for electrode implantation.

In a typical implantation of the DBS electrodes, a bipolar GF microelectrode was implanted unilaterally into the STN (AP: −3.5 mm, ML: −2.5 mm, DV: 7.8 mm from dura) of a hemi-Parkinsonian rat. All GF microelectrodes used in this study were directly inserted into the rat brains. Craniotomies were sealed with a silicone elastomer (World Precision Instruments, USA). Ceramic bone anchor screws, together with dental methacrylate, were used to fix the connector and electrode set onto the rat skull. Electrode tip placements within the STN were verified for each subject by T$_2$-weighted RARE anatomical MRI images acquired immediately after implantation and H&E staining of the coronal brain sections at the end of the study. Animals with electrode placements outside of the target regions were discarded from the study and excluded from all further experimental analyses. They were also not included in the final subject numbers.

DBS and behavioral tests. The efficacy of the GF microelectrodes for DBS was assessed by open-field testing on hemi-Parkinsonian rats. In a typical test, a rat was placed in a box (75 × 75 cm in square and 40 cm high), and the position of the rat's body center was tracked using ANY-maze software (Stoelting, USA), with a digital video camera mounted directly above the arena. An electrical commutator and pulley system was used to allow the rat to move and turn freely within the box. A stimulator (Model 2100, A-M Systems, USA) was used to deliver continuous electrical pulses (biphasic, symmetric, and charge-balanced current pulses of 60 μs duration at 130 Hz). The optimal current intensity was determined by the maximum value that did not cause dyskinetic movement of the contralateral forelimb which gave a current range of 50–200 μA, although for most animals, 100 μA was used. This stimulation parameter setting was consistent with those used in clinical settings[49]. The motor performance of the hemi-Parkinsonian rats before (2 min), during (2 min), and after STN–DBS (2 min) was compared. Several motor behavioral indexes, including time spent in mobility, time spent in freezing, mobile episodes, freezing episodes, and average mobile speed, were recorded and analyzed with ANY-maze software (version 4.70)[30]. Rotation speed was counted and calculated manually. The time spent in mobility and freezing did not add up to 100%, because the rats spent the rest of the time in fine movements.

MRI acquisitions. All MRI experiments were performed in a Bruker 9.4T scanner with Bruker's 86 mm volume coil for transmission and a 2-cm diameter single-loop surface coil for receiving (ParaVision Version 6.0.1 for MRI acquisitions). The implanted electrodes were bent 90° and laid flat along the rats' skulls to allow the placement of the MRI surface receiver coil over the rat heads. Rats were anesthetized with 4% isoflurane, followed by a bolus injection of dexmedetomidine (0.022 mg kg^{-1}). During MRI scanning, isoflurane (0.5%) delivered via a nose cone combined with continuous infusion of dexmedetomidine (0.015 mg kg^{-1} h^{-1}) was used to maintain anesthesia[50]. Animal temperature, respiration, and blood oxygen saturation were all monitored and within normal ranges (Model 1025, SA

Instruments, USA). Body temperature was maintained at 37 ± 0.5 °C using a circulated hot water bed and a hot air blower.

T$_2$-weighted anatomical images were acquired using RARE sequence with the following parameters: TR/TE = 2500/33 ms, RARE factor = 8, FOV = 30 × 30 mm^2, matrix = 256 × 256, slice thickness = 0.8 mm, and contiguous 20 slices without gap in the axial direction. All fMRI data were acquired using a 4-shot gradient-echo EPI sequence with the following parameters: TR/TE = 500/13 ms, FOV = 30 × 30 mm^2, matrix = 80 × 80, flip angle = 55°, repetitions = 105, slice thickness = 0.8 mm, and contiguous 14 slices without gap in the axial direction. B0 distortions were assessed by a high-resolution field map acquired using a dual-echo 3D gradient-echo sequence with the following parameters: TR = 20 ms, TE1 = 1.6 ms, TE2 = 5.2 ms, FOV = 40 × 40 × 40 mm^3, and matrix = 64 × 64 × 64. To measure the electrode artifact size, raw MRI images with the largest electrode artifact were selected and upsampled from 0.12 × 0.12 × 0.8 mm^3 to 0.06 × 0.06 × 0.8 mm^3 voxel resolution. A canny edge detector in Matlab (R2018a, Mathworks, USA) was used to detect the artifact edge (Supplementary Fig. 7). The artifact size in the medial–lateral direction was then measured and averaged over different animal subjects.

The fMRI scans were acquired for 210 s (70 repetitions), during which stimulation was applied in a 60 s-OFF/30 s-ON/120 s-OFF cycle, with the following parameters: bipolar square-wave current with an amplitude of 300 μA, frequency of 10, 100, 130, and 250 Hz, and pulse width of 7.8/f ms, where f is frequency in Hz. Pulse width was varied in this way in order to make the total duration of current delivery over the stimulation period constant. Stimulation frequencies were varied in a pseudo-randomized order, and at each DBS frequency the EPI scan was repeated three times per rat for within subject/session averaging. The electrode location at STN was confirmed with H&E staining of the coronal brain sections at the end of the study. DBS–fMRI studies were carried out on eight rats. Two rats were unable to undergo behavioral tests because their connectors were accidentally damaged before the behavioral tests. All animal experiments were not blinded.

fMRI data analysis. Data analysis was performed using a custom-written program developed using Matlab (R2018a, MathWorks, USA) and SPM12 (http://www.fil.ion.ucl.ac.uk/). EPI images were first grouped by subject and DBS frequency, and realigned to the first volume of the first session, using a least squares approach and a six-parameter rigid body spatial transformation, and then co-registered to the subject's own T$_2$ anatomical images, which were normalized to a rat brain template. EPI images were spatially smoothed with a full-width half maximum (FWHM) of 0.8 × 0.8 mm. B0 field maps were also co-registered to an anatomical template using their reconstructed magnitude images. After preprocessing, statistical analysis was conducted across subjects using a general linear model with reference to the stimulation paradigm, and the default hemodynamic response function of SPM was used. For each scan, the time series was converted to relative BOLD response (ΔS(t)/S0), where ΔS(t) was generated by subtracting the mean of pre-stimulation period (S0) of that scan. For four different DBS frequency groups, the t-statistic maps of each subject were averaged, respectively, with a significance level set at $p < 0.001$.

For ROIs time course analysis, eight ROIs were anatomically defined and applied to co-registered data, including the cingulate cortex, motor cortex, somatosensory cortex, caudate putamen, internal globus pallidus, external globus pallidus, subthalamic nucleus, and thalamus. The BOLD signal time courses were calculated for each ROI. One-way repeated measures ANOVA tests with Tukey post hoc analysis were conducted to evaluate frequency-dependent responses[10]. Significance level was set at *$p < 0.05$; **$p < 0.01$; ***$p < 0.001$. Data plotting and analysis were performed using Origin 2020.

Data availability
The authors declare that the data supporting the findings of this study are available within the article and its Supplementary Information files or available from the corresponding authors upon reasonable request, including all raw MRI image files. The source data underlying Figs. 1e–i, 2b–g, 3g-h, 5a–h, and 6b, and Supplementary Figs. 1, 2, 3, 4, 5, 10c, 12, and 14 are provided as a Source Data file.

Code availability
Custom code used in this study has been deposited on GitHub.

References

1. Kemler, M. A. et al. Spinal cord stimulation in patients with chronic reflex sympathetic dystrophy. *N. Engl. J. Med.* **343**, 618–624 (2000).

2. Ryugo, D. K., Kretzmer, E. A. & Niparko, J. K. Restoration of auditory nerve synapses in cats by cochlear implants. *Science* **310**, 1490 (2005).

3. Jackson, A. & Zimmermann, J. B. Neural interfaces for the brain and spinal cord—restoring motor function. *Nat. Rev. Neurol.* **8**, 690 (2012).

4. Milby, A. H., Halpern, C. H. & Baltuch, G. H. Vagus nerve stimulation for epilepsy and depression. *Neurotherapeutics* **5**, 75–85 (2008).

5. Benabid, A. L., Chabardes, S., Mitrofanis, J. & Pollak, P. Deep brain stimulation of the subthalamic nucleus for the treatment of Parkinson's disease. *Lancet Neurol.* **8**, 67–81 (2009).

6. Ressler, K. J. & Mayberg, H. S. Targeting abnormal neural circuits in mood and anxiety disorders: from the laboratory to the clinic. *Nat. Neurosci.* **10**, 1116 (2007).

7. Pienaar, I. S. et al. Deep-brain stimulation associates with improved microvascular integrity in the subthalamic nucleus in Parkinson's disease. *Neurobiol. Dis.* **74**, 392–405 (2015).

8. Yang, P. F. et al. Comparison of fMRI BOLD response patterns by electrical stimulation of the ventroposterior complex and medial thalamus of the rat. *PLoS ONE* **8**, e66821 (2013).

9. Chao, T. H. H., Chen, J. H. & Yen, C. T. Repeated BOLD-fMRI imaging of deep brain stimulation responses in rats. *PLoS ONE* **9**, e97305 (2014).

10. Van Den Berge, N. et al. Functional circuit mapping of striatal output nuclei using simultaneous deep brain stimulation and fMRI. *Neuroimage* **146**, 1050–1061 (2017).

11. Lai, H. Y., Younce, J. R., Albaugh, D. L., Kao, Y. C. J. & Shih, Y. Y. I. Functional MRI reveals frequency-dependent responses during deep brain stimulation at the subthalamic nucleus or internal globus pallidus. *Neuroimage* **84**, 11–18 (2014).

12. Arantes, P. R. et al. Performing functional magnetic resonance imaging in patients with Parkinson's disease treated with deep brain stimulation. *Mov. Disord.* **21**, 1154–1162 (2006).

13. Shyu, B. C., Lin, C. Y., Sun, J. J., Chen, S. L. & Chang, C. BOLD response to direct thalamic stimulation reveals a functional connection between the medial thalamus and the anterior cingulate cortex in the rat. *Magn. Reson. Med.* **52**, 47–55 (2004).

14. Schenck, J. F. The role of magnetic susceptibility in magnetic resonance imaging: MRI magnetic compatibility of the first and second kinds. *Med. Phys.* **23**, 815–850 (1996).

15. Kuzum, D. et al. Transparent and flexible low noise graphene electrodes for simultaneous electrophysiology and neuroimaging. *Nat. Commun.* **5**, 5259 (2014).

16. Park, D. W. et al. Graphene-based carbon-layered electrode array technology for neural imaging and optogenetic applications. *Nat. Commnun.* **5**, 5258 (2014).

17. Yin, R. et al. Soft transparent graphene contact lens electrodes for conformal full-cornea recording of electroretinogram. *Nat. Commnun.* **9**, 2334 (2018).

18. Zelin, D. et al. Facile fabrication of light, flexible and multifunctional graphene fibers. *Adv. Mater.* **24**, 1856–1861 (2012).

19. Xin, G. et al. Highly thermally conductive and mechanically strong graphene fibers. *Science* **349**, 1083–1087 (2015).

20. Jancrazio, P. J. et al. Thinking small: progress on microscale neurostimulation. *Technol. Neuromodulation* **20**, 745–752 (2017).

21. Moon, I. K., Lee, J., Ruoff, R. S. & Lee, H. Reduced graphene oxide by chemical graphitization. *Nat. Commnun.* **1**, 73 (2010).

22. Cogan, S. F. Neural stimulation and recording electrodes. *Annu. Rev. Biomed. Eng.* **10**, 275–309 (2008).

23. Weiland, J. D., Anderson, D. J. & Humayun, M. S. In vitro electrical properties for iridium oxide versus titanium nitride stimulating electrodes. *IEEE Trans. Biomed. Eng.* **49**, 1574–1579 (2002).

24. Cogan, S. F., Troyk, P. R., Ehrlich, J., Plante, T. D. & Detlefsen, D. E. Potential-biased, asymmetric waveforms for charge-injection with activated iridium oxide (AIROF) neural stimulation electrodes. *IEEE Trans. Biomed. Eng.* **53**, 327–332 (2006).

25. Vitale, F., Summerson, S. R., Aazhang, B., Kemere, C. & Pasquali, M. Neural stimulation and recording with bidirectional, soft carbon nanotube fiber microelectrodes. *ACS Nano* **9**, 4465–4474 (2015).

26. Lu, L. et al. Soft and MRI compatible neural electrodes from carbon nanotube fibers. *Nano Lett.* **19**, 1577–1586 (2019).

27. Green, R. A., Lovell, N. H., Wallace, G. G. & Poole-Warren, L. A. Conducting polymers for neural interfaces: challenges in developing an effective long-term implant. *Biomaterials* **29**, 3393–3399 (2008).

28. Cui, X. T. & Zhou, D. D. Poly (3,4-ethylenedioxythiophene) for chronic neural stimulation. *IEEE Trans. Neural Syst. Rehabil. Eng.* **15**, 502–508 (2007).

29. Gradinaru, V., Mogri, M., Thompson, K. R., Henderson, J. M. & Deisseroth, K. Optical deconstruction of parkinsonian neural circuitry. *Science* **324**, 354–359 (2009).

30. Li, Q. et al. Therapeutic deep brain stimulation in parkinsonian rats directly influences motor cortex. *Neuron* **76**, 1030–1041 (2012).

31. Coffey, R. J. Deep brain stimulation devices: a brief technical history and review. *Artif. Organs* **33**, 208–220 (2009).

32. Tagliati, M. et al. Safety of MRI in patients with implanted deep brain stimulation devices. *Neuroimage* **47**, T53–T57 (2009).

33. Zhao, S. et al. Graphene encapsulated copper microwires as highly MRI compatible neural electrodes. *Nano Lett.* **16**, 7731–7738 (2016).

34. Stice, P., Gilletti, A., Panitch, A. & Muthuswamy, J. Thin microelectrodes reduce GFAP expression in the implant site in rodent somatosensory cortex. *J. Neural Eng.* **4**, 42–53 (2007).

35. Paek, S. B. et al. Frequency-dependent functional neuromodulatory effects on the motor network by ventral lateral thalamic deep brain stimulation in swine. *Neuroimage* **105**, 181–188 (2015).

36. Tarsy, D., Vitek, J. L., Starr, P. & Okun, M. *Deep Brain Stimulation in Neurological and Psychiatric Disorders* (Humana Press, Totowa, 2008).

37. Kahan, J. et al. Therapeutic subthalamic nucleus deep brain stimulation reverses cortico-thalamic coupling during voluntary movements in Parkinson's disease. *PL0S ONE* **7**, e50270 (2012).

38. Kim, H. J. et al. Chronic subthalamic deep brain stimulation improves pain in Parkinson disease. *J. Neurol.* **255**, 1889 (2009).

39. Okun, M. S. et al. Cognition and mood in Parkinson's disease in subthalamic nucleus versus globus pallidus interna deep brain stimulation: The COMPARE Trial. *Ann. Neurol.* **65**, 586–595 (2009).

40. Stefurak, T. et al. Deep brain stimulation for Parkinson's disease dissociates mood and motor circuits: a functional MRI case study. *Mov. Disord.* **18**, 1508–1516 (2003).

41. Mallet, L. et al. Stimulation of subterritories of the subthalamic nucleus reveals its role in the integration of the emotional and motor aspects of behavior. *Proc. Natl Acad. Sci. USA* **104**, 10661–10666 (2007).

42. Alexander, G. E., Delong, M. R. & Strick, P. L. Parallel organization of functionally segregated circuits linking basal ganglia and cortex. *Annu. Rev. Neurosci.* **9**, 357 (1986).

43. Min, H. K. et al. Deep brain stimulation induces BOLD activation in motor and non-motor networks: an fMRI comparison study of STN and EN/GPi DBS in large animals. *Neuroimage* **63**, 1408–1420 (2012).

44. Jech, R. et al. Functional magnetic resonance imaging during deep brain stimulation: a pilot study in four patients with Parkinson's disease. *Mov. Disord.* **16**, 1126–1132 (2001).

45. Han, Z. et al. Awake and behaving mouse fMRI during Go/No-Go task. *Neuroimage* **188**, 733–742 (2019).

46. Georgi, J. C., Stippich, C., Tronnier, V. M. & Heiland, S. Active deep brain stimulation during MRI: a feasibility study. *Magn. Reson. Med.* **51**, 380–388 (2004).

47. Jiang, C. Q., Hao, H. W. & Li, L. M. Artifact properties of carbon nanotube yarn electrode in magnetic resonance imaging. *J. Neural Eng.* **10**, 026013 (2013).

48. Johannes, B. E. et al. Should patients with brain implants undergo MRI? *J. Neural Eng.* **15**, 041002 (2018).

49. Nilsson, M. H., Jarnlo, G. B. & Rehncrona, S. Functional balance performance in patients with Parkinson's disease after long-term treatment with subthalamic nucleus high-frequency stimulation. *Parkinsonism Relat. Disord.* **14**, 291–297 (2008).

50. Brynildsen, J. K. et al. Physiological characterization of a robust survival rodent fMRI method. *Magn. Reson. Imaging* **35**, 54–60 (2017).

Author contributions

X.D. and S.Z. conceived and designed the experiments. S.Z., G.L., P.W., X.F., and L.L. fabricated and characterized the electrodes. S.Z., G.L., Z.X., and X.L. performed the open-field tests and analysis. S.Z., G.L., C.T., W.C., J.D., Z.X., and Z.L. conducted the MRI and DBS–fMRI studies and analysis. X.D. supervised the project. X.D., S.Z., G.L., C.T., W.C., and Z.L. wrote the paper. All of the authors discussed the results and commented on the paper.

Competing interests

The authors declare no competing interests.

Additional information

Supplementary information is available for this paper at https://doi.org/10.1038/s41467-020-15570-9.

Correspondence and requests for materials should be addressed to Z.L. or X.D.

Peer review information *Nature Communications* thanks Shella Keilholz, Yen-Yu Ian Shih and the other, anonymous, reviewer(s) for their contribution to the peer review of this work.

Reprints and permission information is available at http://www.nature.com/reprints

Publisher's note Springer Nature remains neutral with regard to jurisdictional claims in published maps and institutional affiliations.